A MULTIMODALITY CMOS CELLULAR INTERFACING ARRAY FOR HOLISTIC CELLULAR CHARACTERIZATION AND CELL-BASED DRUG SCREENING

A Dissertation
Presented to
The Academic Faculty

by

Jong seok Park

In Partial Fulfillment
of the Requirements for the Degree
Doctor of Philosophy in the
School of Electrical and Computer Engineering

Georgia Institute of Technology
December 2017

A MULTIMODALITY CMOS CELLULAR INTERFACING ARRAY FOR HOLISTIC CELLULAR CHARACTERIZATION AND CELL-BASED DRUG SCREENING

Approved by:

Dr. Hua Wang, Advisor
School of Electrical and Computer Engineering
Georgia Institute of Technology

Dr. Muhannad Bakir
School of Electrical and Computer Engineering
Georgia Institute of Technology

Dr. Wilbur A. Lam
Department of Biomedical Engineering
Georgia Institute of Technology

Dr. Oliver Brand
School of Electrical and Computer Engineering
Georgia Institute of Technology

Dr. Omer T. Inan
School of Electrical and Computer Engineering
Georgia Institute of Technology

Date Approved: Nov. 3, 2017

To my family

ACKNOWLEDGEMENTS

I would like to express my sincere gratitude to my advisor Dr. Hua Wang for his enthusiastic and effective guidance and unconditional support. I am very proud of being a member of Georgia tech Electronics and Micro-System (GEMS) lab, especially as one of starting members of GEMS lab with Dr. Hua Wang. I was very lucky that I can work very closely with Dr. Hua Wang and directly learn his hands-on techniques. During my Ph.D, I have learned a lot from Dr. Hua Wang about not only technical things but also patience, enthusiasm, devotion, dedication, and professionalism in his work. In addition, I feel very happy to see the achievement and growth of GEMS lab. Also, I would like to thank Dr. Todd McDevitt and Dr. Tracy Hookway of Gladstone/UCSF, Dr. Mark Styczynski of Georgia Tech, and Dr. Hee-cheol Cho of Emory University for technical discussions and collaborations.

I would like to especially thank Dr. Muhannad Bakir, Oliver Brand, Dr. Omer Inan, and Dr. Wilbur Lam for serving as my dissertation committees. Their valuable technical suggestions and feedback have been very helpful to further advance my research.

I extend my sincere gratitude to all members of Georgia tech Electronics and Micro-System (GEMS) lab, including Taiyun Chi, Song Hu, Tso-Wei Li, Sensen Li, Min-Yu Huang, Fei Wang, Doohwan Jung, Moez Aziz, Edgar Garay, Huy Thong Nguyen, Yeojoon Youn, Adam Wang, Sanghoon Lee, and Tzu-Yuan Huang. In addition, I would like to

especially thank Taiyun Chi and Song Hu, who are the other starting members of GEMS lab. I am very proud of working together with them and I have learned a lot from them.

I also would like to thank members of Wireless Communications Research (WCR) lab at Intel, Hillsboro, Oregon, including Dr. Christopher Hull, Dr. Stefano Pellerano, and Dr. Yanjie Wang for their technical suggestions and supporting my Ph.D and internship. It was my first industry experience and my great pleasure to work with them.

I would like to express my appreciation and respect to my father Yoongiu Park and my mother Soonam Lee for their endless love, support, and trust. Last, but the most important, I would like to thank Jesus Christ for all blessings and amazing grace.

TABLE OF CONTENTS

LIST OF TABLES

LIST OF FIGURES

SUMMARY

Cell are the basic structural, functional, and biological units of all known living organisms. Understanding the physiological behaviors of living cells and tissues is a prerequisite to further advance bioscience and biotechnologies, such as synthetic biology, stem cell manufacturing, and regenerative medicine. Moreover, both wide-type and genetically modified cells have been widely used as powerful sensing and diagnostic tools in cell-based assays; these assays are the key enablers in numerous high-impact applications, including characterizing the potency and toxicity of new drugs in pre-clinical pharmaceutical development, determining the patient-specific treatments in personalized medicine, fast pathogen screening for epidemic disease detections, and detecting biohazards and pollutants in environmental monitoring. However, cells are highly complex systems with numerous molecules operating in hundreds of pathways to maintain their proper functions, phenotypes, and physiological behaviors. With this daunting scale of complexity, cells often undergo concurrent multi-physics responses when subjected to external biochemical stimuli or physiological condition shifts. On the other hand, existing integrated electronic sensors are mostly of single-modality to capture one category of cellular physiological responses, e.g., neural recording and stimulation systems for measuring neuron activities, electrical impedance sensors for cell-growth assay and detecting myocardial ischemia, pH sensors for cellular metabolism assay, magnetic cell-based sensor for measuring cardiac beating rate, and optical sensors for DNA sequencing. Such single-modality sensors fundamentally cannot capture the complex multi-physics cellular responses and largely limit our understanding on the cellular behaviors and dynamics. This is particularly true for drug screening application. When cells are exposed to drug or biochemical stimulus, cells exhibit complex behaviors that demand multi-

physics and multi-parametric modeling. The key objective is to real-time capture multi-physical cellular physiological responses from the same cellular sample with a high spatiotemporal resolution. In addition, it is highly desired to support cellular stimulations or actuations, which enable various in-depth cellular studies. For example, electrical stimulation promotes the cardiac differentiation of human cardiac progenitor cells and the maturation of cardiomyocytes derived from human embryonic stem cells, and it also can be used to study cellular behaviors under various neurological and cardiovascular diseases.

To address these challenges, my Ph.D research focuses on investigating CMOS multimodality cellular sensing/actuation array platforms to achieve (1) simultaneous detections of multiple orthogonal cellular physiological responses in each array pixel, (2) arbitrarily reprogrammable and multi-site concurrent electrical cellular stimulations, (3) single-cell resolution array pixel, and (4) on-chip signal processing units for rapid and self-contained cellular diagnostics. In addition, since the platform is directly interfacing with living cells, I have investigated on (5) the biocompatibility of the CMOS sensor, including electro-less gold plating on microscale aluminum electrodes, protein coatings, and high solution resistance and reliable biocompatible packaging techniques, which is particularly important to successfully culture living cells on the sensor surface and to study long-term drug effects. Furthermore, I have investigated on (6) the culturing various living cells such as neurons, cardiomyocytes, fibroblast, and cancer cells on the fully packaged CMOS sensor array for *in vitro* cell-based experiments.

My proposed platforms will enable real-time holistic cellular characterization and impact many areas including drug screening, stem cell manufacturing, regenerative medicine, implantable bioelectronics, and neural/cognitive sciences. Moreover, my proposed platforms will open the door to future hybrid biotic/abiotic (cells/semiconductor) systems for analyte detections, chemical syntheses, and signal processing/computing.

CHAPTER 1

INTRODUCTION

1.1. Motivation

All living things are made up of cells and cells are the smallest and the most basic structural and functional building blocks for life [1]-[3]. The characterization of physiochemical behavior of cells and the understanding the cellular and molecular mechanisms are the first step for the scientific progress in biotechnologies and biosciences such as synthetic biology [4] stem cell manufacturing [5] and regenerative medicine [6]. Cell based assay has been widely used for cell characterization and drug screening due to its unique advantages (Fig. 1.1). Since it directly uses living cells, it provides physiologically relevant information and offers an accurate representation of a real-life model. It also achieves a high sensitivity and responses can be very fast. Recently, cell-based assay has gained tremendous interest for new emerging applications such as a drug discovery, epidemic disease detections, and an environmental monitoring for detecting bio-hazards and pollutants. In particular, cell-based assay has a great potential in a personalized medicine as the patient derived cells can be directly used to test a potency, efficacy, and toxicity of a newly developed patient-specific medicine.

However, cells are highly complex system with multi-physics and multi-parametric activities. For example, cells perform chemical activities such as anabolism (the synthesis of complex organic molecules from simple organic molecules with the storage of energy) and catabolism (the breakdown of complex organic molecules to simple organic molecules with the release of energy) and mechanical activities such as movement towards the external stimuli such as chemicals (chemotaxis), photons (phototaxis), and hormones.

Furthermore, cells can harvest and utilize energy. For example, most of cells perform cellular respiration and plant cells undergo photosynthesis.

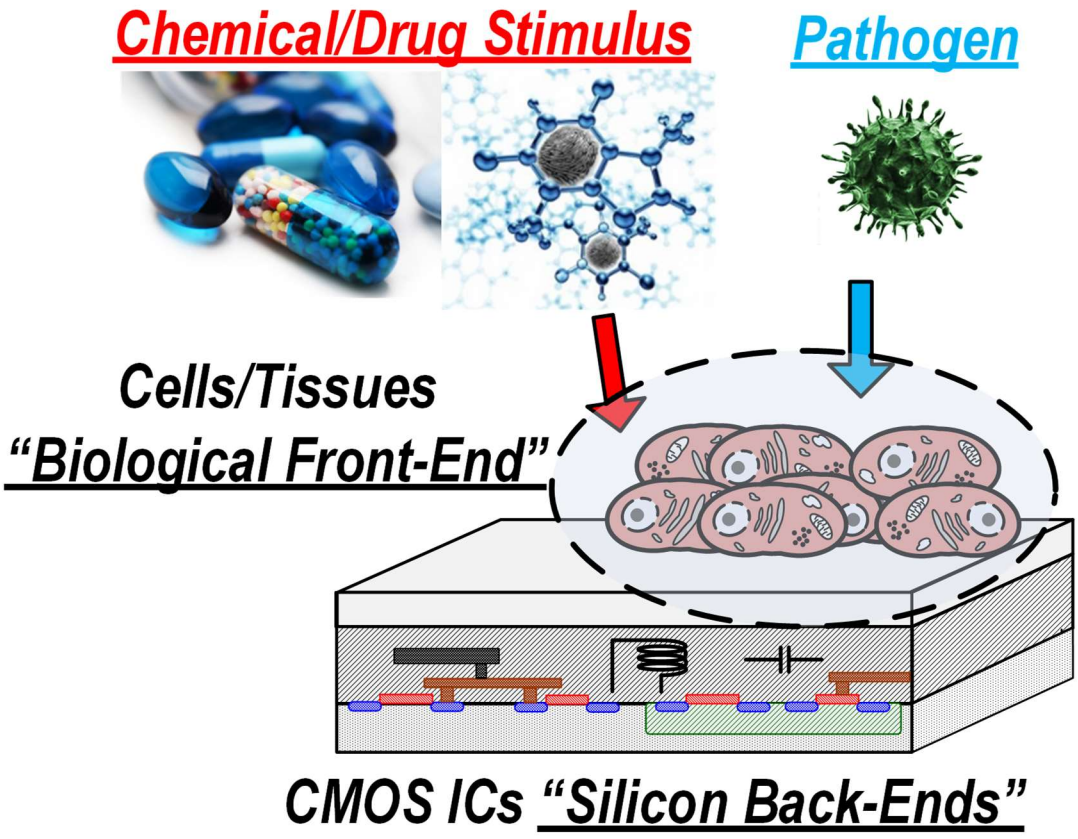

Fig. 1.1. Cell-based sensor and actuator.

A variety of single-modality cell-based sensors and actuators have been proposed and successfully demonstrated to capture one type of physiological changes. For a potential recording, patch pipettes which penetrates into the cell membrane and measure the intracellular potentials have been widely used. However, it requires bulky and dedicated mechanical setup and therefore, not suitable for the large-scale high-throughput applications. Moreover, since it is invasive type of contact, it cannot support long-term recording. To address these challenges, recently, an extracellular potential recording using microelectrode array has gained tremendous interest. In particular, microelectrode array

together with read-out circuits fully integrated in CMOS platform has been an active research area [7]-[9]. A CMOS low-noise bio-amplifier that employs PMOS pseudo resistors, operational amplifier, and capacitors achieves low cut-off frequency of 0.025Hz and low input-referred noise of 2.2μVrms integrated from 0.025Hz to 7.2kHz and cell-based measurement results demonstrate extracellular action potential recording of rat olfactory cortex in the paper [7]. A large-scale high-throughput extracellular potential recording of on-chip cultured snail neuron is also demonstrated with 128×128 microelectrode array with the electrode pitch size of 7.8μm [8]. Furthermore, in order to study plasticity and learning process, in-situ electrical stimulation is added in the microelectrode sensor array and a 1024-channel extracellular potential recordings after an electrical stimulation are demonstrated in the paper [9].

Electrical impedance sensing has been widely used to capture electrochemical activities of bio-samples [10]-[12]. A 10×10 sensor array integrated in a standard CMOS process [10] demonstrates the detection of a wide variety of DNAs and proteins in real time without a molecular label using an electrochemical impedance spectroscopy. In the paper [11], a 16×8 array integrated in CMOS demonstrates a successful detection of DNAs by an electrochemical redox cycling process. It is also recently reported in the paper [12] that two pair of microelectrodes are integrated in the hanging drop network to monitor the size of micro-tissue spheroids, e.g., the cancer cell growth assay, and to measure the beating rate of cardiac micro-tissues.

Optical measurements are one of the most accurate and fundamental measurement methods and therefore, have been widely used for bio-sample characterizations. However, optical measurements often require bulky and very expensive instruments such as a lens, laser source, and optical filter. In order to address these challenges, many efforts have been made to develop a cost-efficient and miniaturized optical sensor for point-of-care and point-of-use applications [13]-[15]. A CMOS fluorescent-based biosensor microarray is proposed in the paper [13] that CMOS sensor array chip, thin-film optical long-pass filter,

and fiber-optical faceplate are integrated and packaged together as a single chip module and successfully measures DNA hybridization kinetics. Note that the thin-film optical long-pass filter (20 layers with the total thickness of 2.1μm) is directly deposited on top of the CMOS sensor chip together with a fiber-optical faceplate (wave-guide) to achieve the excitation light rejection of 98dB. In order to further reject the excitation light or potentially obviate the use of an optical filter, the time-resolved or time-gated fluorescence detection method implemented in CMOS process is also reported in the paper [14]. On the other hand, a bioluminescent detection with a fiber-optic faceplate and immobilized luminescent reporters is reported in the paper [15]. A 8×16 array is implemented in CMOS and successfully demonstrates DNA sequencing by measuring emitted visible light intensity using a linked enzymatic reaction in the paper [15].

Sensing modality	Physiological measurements	Sensing circuits
Extracellular potential recording	Seizure detection, neuroprosthetics, cardiac arrhythmia, action potential propagation, etc.	Low-noise voltage amplifier (Sub-Hz to KHz)
Electrical stimulator	Neurological and cardiovascular diseases, sensory modality lost, cardiomyocytes maturation and differentiation	5 bit active charge balancing current sources
Complex impedance measurement	Detection of a wide variety of DNAs and proteins, cardiac beating rate, myocyte ischemia, cell growth	Voltage excitation and current sensing (KHz to MHz)
PH sensing	Cell metabolism assay,	ISFET
Magnetic sensing	Cell movement tracking, cardiac muscle contraction/ relaxation	Inductor
Fluorescent detection	DNA hybridization kinetics, fluorescent imaging, etc.	Photo-diode and thin film optical filter
Optical detection	Bioluminescent detection, DNA sequencing, cell growth, cell viability, cardiomyocyte contraction/relaxation	Photo-diode

Fig. 1.2. Summary of the cell-based sensors and actuators.

However, the existing single-modality sensors can only capture one-type of cellular physiological changes and require additional efforts to capture multi-physical cellular responses. For example, bio-samples can be sequentially transferred through multiple

single-modality sensors. However, it suffers from potential abrogation of cell functions and results in low throughput. Parallel monitoring of multiple cell samples each with different single-modality sensor can be another feasible method to capture multi physical cellular behaviors. However, significant sample-sample variations often exist and result in a compromised biological correlation amount the different modality measurements.

To address these unmet challenges, we propose a multimodality sensor array fully integrated in a standard CMOS process for holistic cell characterization and high throughput drug screening [16]-[20]. The proposed multimodality sensor array contains tri-modality pixels including an optical detection (photo diode), a complex impedance sensing (voltage excitation and current sensing), and an extracellular potential recording (low-noise bio-potential amplifier) and a temperature sensor. The extracellular potential recording modality can detect the action potential (300Hz to 20kHz) and/or the local filed potential (1Hz to 300Hz) of the electro-genic cells such as neurons and cardiomyocytes. Complex impedance sensing modality can measure cell-to-sensor surface attachment, cell growth, and the beating rate of cardiomyocytes. Optical detection can measure cell morphology, shape, and opacity changes as well as a cardiac muscle fiber contraction and relaxation. Also, it can be used for bioluminescent assay. To consider the effect of cellular physiological changes due to the ambient temperature variations, cellular environmental thermal monitoring is also required. In addition, it is highly desired to support cellular stimulations or actuations, which enable various in-depth cellular studies. For example, electrical stimulation promotes the cardiac differentiation of human cardiac progenitor cells [76] and the maturation of cardiomyocytes derived from human embryonic stem cells [77] and it also can be used to study cellular behaviors under various neurological and cardiovascular diseases [78]-[82].

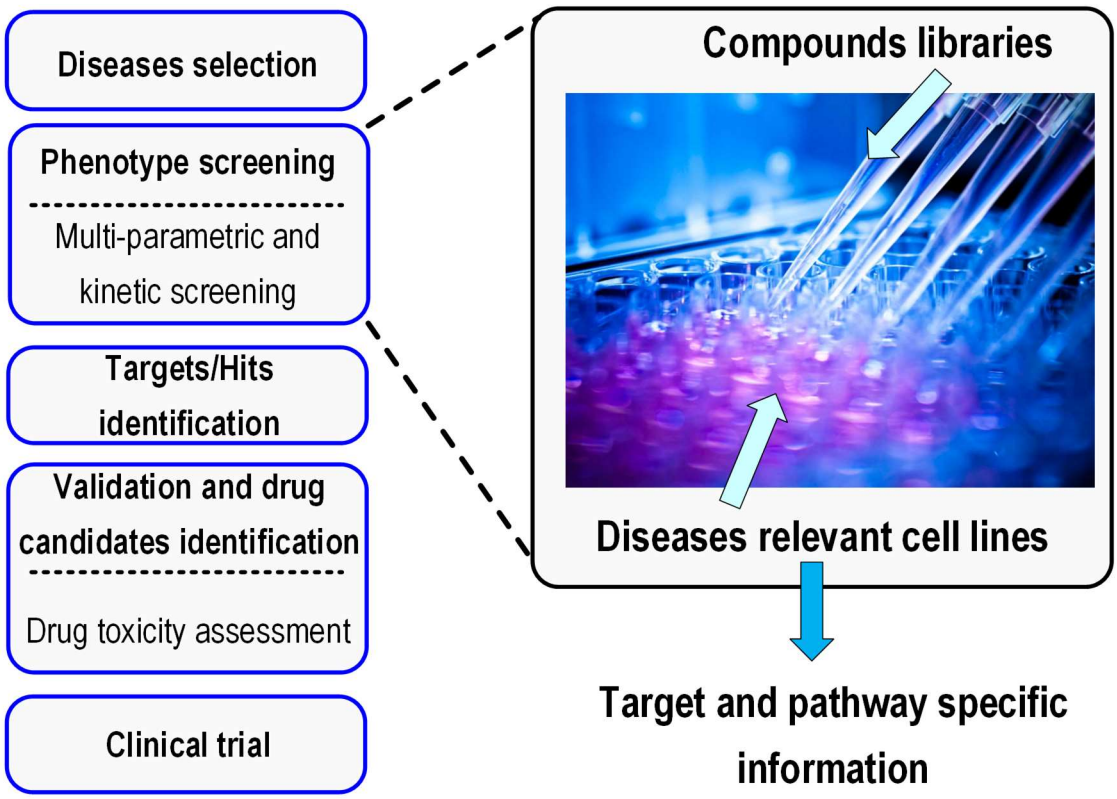

Fig. 1.3. Label-free drug discovery strategy.

The high throughput multimodality sensor and stimulator arrays are particularly useful for drug discovery and drug development. Figure 1.3 shows drug discovery strategy [31]. It consists of following steps; diseases selection, phenotype screening, targets/hits identification, validation, and clinical trial. The details of the drug discovery process are explained as follows. After target diseases are selected, many libraries of compounds are screened in large panels of disease relevant cell lines based on the phenotype screening. Next, targets for specific phenotypes are identified, and hits are selected and identified based on the specific phenotype response. Finally, drug candidates are generated after validation. For phenotype screening, many combinations of diseases relevant cell lines and chemical compounds are investigated and thus this step is very time consuming and labor intensive. Furthermore, for successfully drug screening, multi-parametric and real-time kinetic measurements are of paramount importance, since cell signals could be encoded by

spatiotemporal dynamics and come in multiple pathways. The diseases relevant cellular phenotypes for drug screening application include morphological, structural, electrophysiological abnormalities. For example, cell proliferation, cell death, cell migration, cell division, inflammation, cell-to-cell communication, and cell signaling. Therefore, our proposed CMOS multimodality joint sensor and stimulator array has a great potential in drug screening application, supporting high throughput multi-parametric and real-time kinetic phenotype screening.

1.2. Dissertation Outline

This dissertation is organized as follows. In the chapter 2, we will present a proof-of-concept design of a 144-pixel multimodality CMOS sensor array. Each multimodality pixel supports extracellular recording, optical sensing, and complex impedance measurement with the multimodality pixel size of 80μm×100μm. The human cardiomyocytes, mouse neurons, and human ovarian cancer cells are successfully cultured on the sensor array. The cell-based measurements results including extracellular recording, optical opacity imaging, bioluminescent assay, and complex impedance mapping are presented in chapter 2. Next, the biphasic current stimulator is added to the multimodality CMOS sensor array with improved pixel resolution and field of view. And a 1024-pixel CMOS multimodality joint sensor and stimulator array is presented in the chapter 3. Each multimodality pixel supports extracellular recording, optical sensing, biphasic current stimulation, and complex impedance measurement with the multimodality pixel size of 58μm×58μm. The extensive cell-based measurements based on the on-chip cultured rat cardiomyocytes demonstrate the utility and the benefit of a proposed multimodality joint sensor and stimulator array in the chapter 3. In addition, details of the biocompatible packaging techniques are also presented in the chapter 3. The multimodality pixel resolution is further reduced to a single-cell resolution with wide field of view and a CMOS

22k-Pixel Single-Cell Resolution Multi-Modality Real-Time Cellular Sensing Array is presented in chapter 4 with the multimodality pixel size of 17μm×17μm.

CHAPTER 2

A 144-PIXEL MULTIMODALITY CMOS SENSOR ARRAY FOR CELL-BASED ASSAY AND DRUG SCREENING

In this chapter, we present a fully integrated multi-modality CMOS cellular sensor array with four different sensing modalities to characterize different cell physiological responses, including extracellular voltage recording, cellular impedance mapping, optical detection with shadow imaging and bioluminescence sensing, and thermal monitoring. The sensor array consists of nine parallel pixel groups and nine corresponding signal conditioning blocks. Each pixel group comprises one temperature sensor and 16 tri-modality sensor pixels, while each tri-modality sensor pixel can be independently configured for extracellular voltage recording, cellular impedance measurement (voltage excitation/current sensing), and optical detection. This sensor array supports multi-modality cellular sensing at the pixel level, which enables holistic cell characterization and joint-modality physiological monitoring on the same cellular sample with a pixel resolution of 80μm×100μm. Comprehensive biological experiments with different living cell samples demonstrate the functionality and benefit of the proposed multi-modality sensing in cell-based assay and drug screening.

2.1. Introduction

Cells, often called the “smallest building blocks of life”, are the basic structural, functional, and biological units of all known living organisms [1]-[3]. Fully understanding

the physiological behaviors of living cells and tissues is a prerequisite to further advance the frontiers in bioscience and biotechnologies, such as synthetic biology [4], stem cell manufacturing [5], and regenerative medicine [6]. Moreover, the physiological behaviors and responses of wide-type and genetically modified cells and tissues have been widely exploited as powerful tools in cell-based assays [32]. These assays are the key enablers in a plethora of high-impact applications, including characterizing the potency and toxicity of new drugs in pre-clinical pharmaceutical development [33] [34], determining the patient-specific treatments in personalized medicine [35], fast pathogen screening for epidemic disease detections [36] [37], and detecting biohazards and pollutants in environmental monitoring [38] [39].

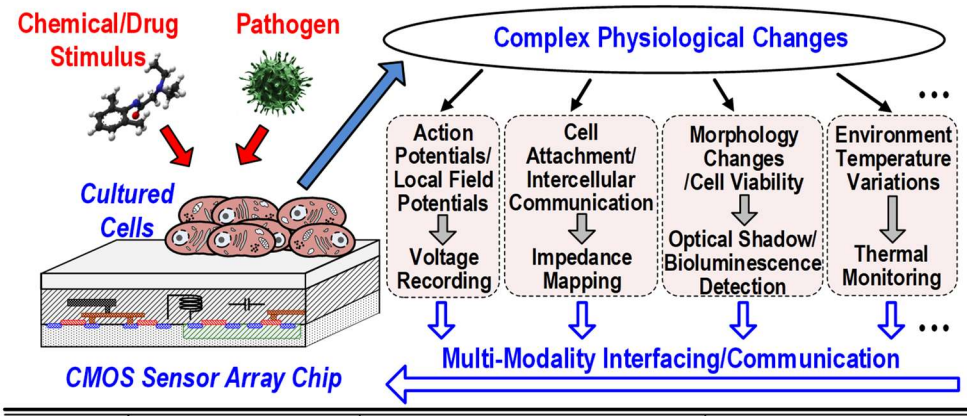

	Sensing Modality	Physiological Measurements	Sensing Circuits
Modality 1	Electrical voltage recording	Cellular action potentials and local field potentials	Voltage amplifier (sub-Hz to kHz)
Modality 2	Electrical impedance mapping	Cell attachment and intercellular communications	V-excitation and I-sensing (kHz to MHz)
Modality 3	Optical detection	Cell morphology changes (shape, etc.) and viability testing	Photodiode and amplifier
Modality 4	Thermal monitoring	Environmental temperature variations	Temperature sensor

Fig. 2.1. (a) The proposed multi-modality CMOS sensor array to capture the multi-physics physiological behaviors of cells when exposed to drug or pathogen stimulus.

However, cells are highly complex systems with numerous molecules operating in hundreds of pathways to maintain their proper functions, phenotypes, and physiological behaviors [1]-[3]. With this scale of complexity, cells often undergo concurrent multi-physics responses when subjected to external biochemical stimuli or physiological condition shifts (Fig. 2.1a).

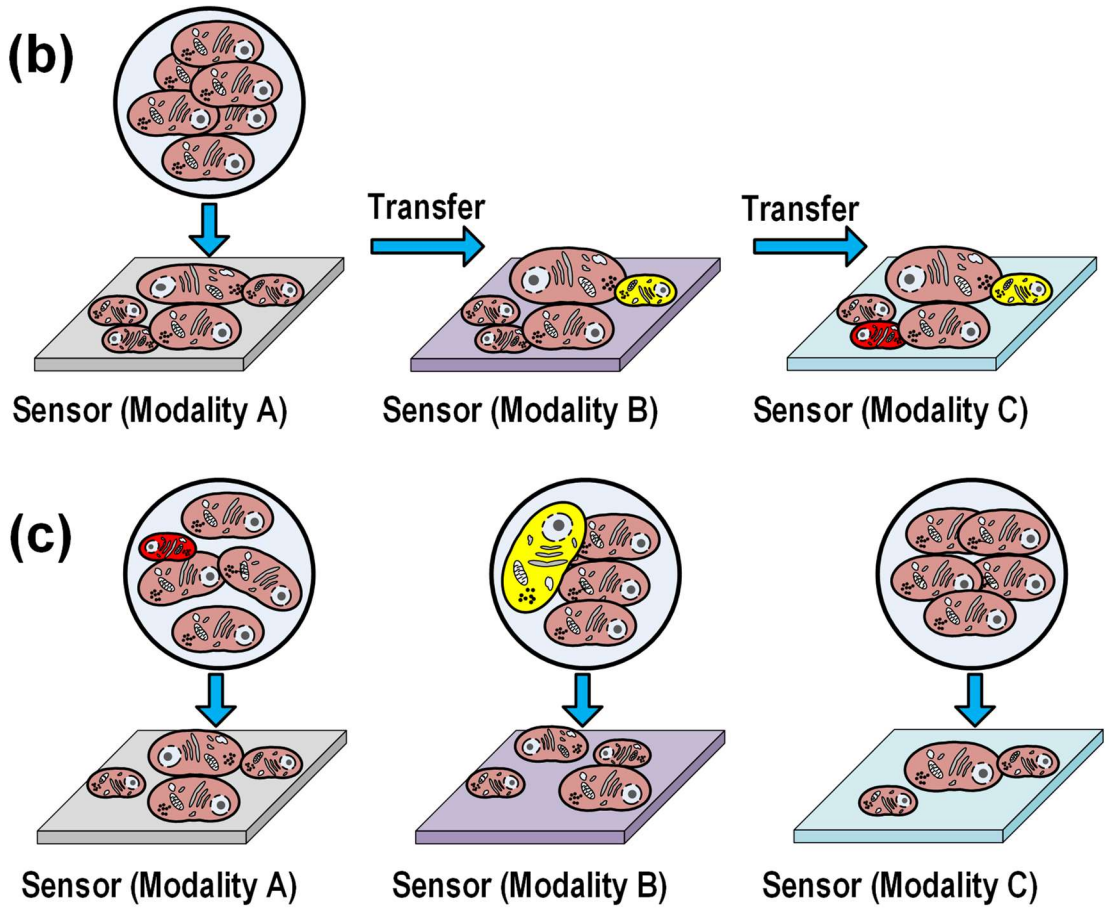

Fig. 2.1. (b) Sequentially transferring the cell samples through multiple single-modality sensors, resulting in a low throughput, potential abrogation of cellular functions, and incompatibility with concurrent joint-modality monitoring. (c) Parallel monitoring multiple cell samples with different single-modality sensors, suffering from sample-to-sample variations and compromised biological correlation among measurements of different modalities.

On the other hand, existing microelectronic sensors are mostly of single-modality, which can only respond to one type of physiological signals, e.g., electrochemical [10] [11] [40] [41], or optical [13] [14] from the cells. Such single-modality sensors fundamentally cannot capture the complex multi-physics physiological responses of cells, thus limiting the understanding of the cellular behaviors and dynamics. Although one may sequentially transfer the cell samples through multiple microelectronic sensors each with a different sensing modality (Fig. 2.1b), this approach will result in a low throughput and potential abrogation of cellular functions. Moreover, it cannot support concurrent monitoring of multiple cellular responses under drug administration and is not compatible with terminal biochemical assays. Another approach is to perform parallel screening of multiple samples each with a different single-modality sensor (Fig. 2.1c). However, since the multi-physical responses are recorded based on different cellular samples, potential sample-to-sample variations will substantially compromise the biological correlation among the measurements of different modalities.

To address these unmet challenges, we propose a fully integrated multi-modality cellular sensor array in CMOS. The sensor array includes nine parallel pixel groups, and each pixel group compromises one temperature sensor and 16 tri-modality sensor. Therefore, the entire sensor array can detect four distinct cell physiological responses, including extracellular voltage recording, cellular impedance mapping, optical detection with shadow imaging and bioluminescence sensing, and thermal monitoring [16] so that the multi-physics responses of the cells-under-test can be real-time characterized. Furthermore, this sensor array is compatible with standard low-cost CMOS processes. The proposed multi-modality sensor array offers a new cellular sensing platform, which allows

holistic understanding of cellular physiology, enables large-scaled high-throughput high-content drug screening, and potentially revolutionizes cell-based assays in the future.

This chapter is organized as follows. The proposed multi-modality sensor array system in CMOS is introduced in chapter 2.2. The sensor pixel design and programmable signal conditioning blocks are presented in chapter 2.3 and 2.4, respectively. The electrical measurements of the sensor array chip are shown in chapter 2.5. Extensive biological measurements using on-CMOS cultured cells are presented in chapter 2.6, demonstrating the use of the multi-modality CMOS sensor array in cell-based assays and drug detection.

2.2. Multimodality Sensor Array System

The sensor pixel array architecture is depicted in Fig. 2.2 with the top-level schematic shown in Fig. 2.3. The CMOS chip contains 9 pixel groups and 9 corresponding programmable signal conditioning blocks. Within each pixel group, there are 16 (4×4) tri-modality sensor pixels and one temperature sensor. Each tri-modality pixel can be independently configured for voltage recording, cellular impedance measurement (voltage excitation/current sensing), and optical detection. Therefore, the entire sensor array provides 144 tri-modality sensor pixels and 9 temperature sensors. These on-chip sensing modalities enable real-time multi-physics cellular monitoring of extracellular voltage recording, cellular impedance mapping, optical opacity/luminescence detection, and temperature monitoring. Moreover, such pixelated multi-modality sensing scheme opens the door to real-time joint-modality characterization of cell samples under normal physiological conditions or with external chemical/physical stimulus.

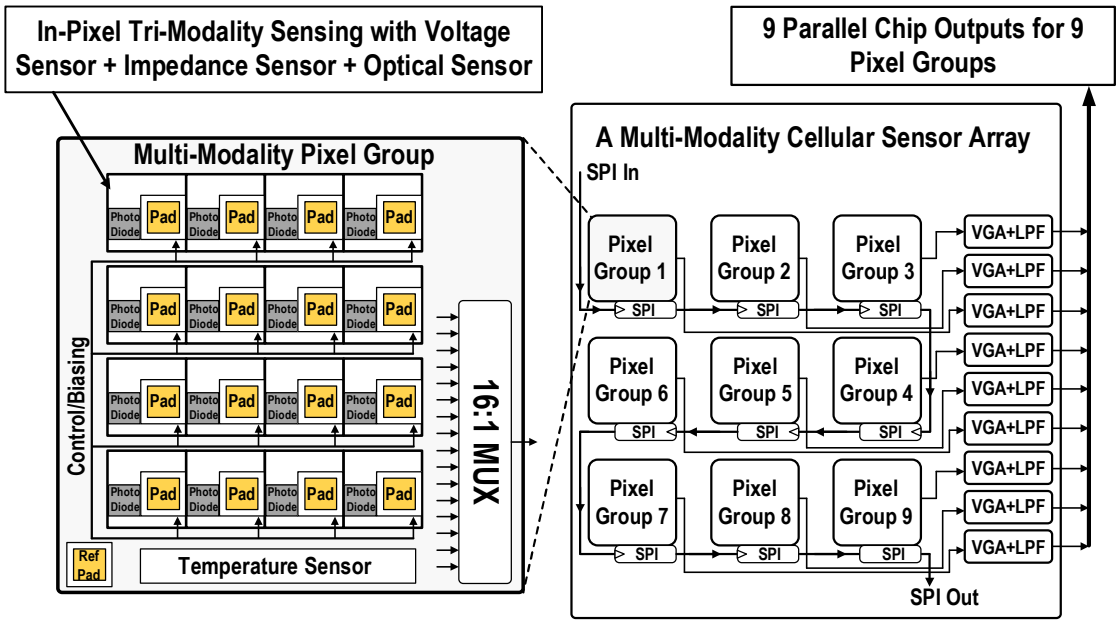

Fig. 2.2. The multi-modality sensor array architecture (right) and the pixel group architecture (left).

To facilitate extracellular voltage recording and impedance detection, each sensing electrode is AC-coupled to the cell culture medium to remove the DC voltage offset and drift of the electrode-electrolyte interface [10] [21]. Within each tri-modality sensor pixel, the sensing electrode occupies 40µm×40µm, which is shared by the extracellular voltage recording and impedance detection. A 40µm×40µm photodiode is also implemented in each pixel for cellular optical detections. Together with the in-pixel amplifiers and switches, the tri-modality sensor pixel occupies a footprint of 80µm×100µm.

Circuits sharing techniques are exploited for the sensor pixel front-end circuits to achieve tri-modality sensing with a compact size (Fig. 2.4). In particular, one in-pixel operational amplifier (OA) is shared between the voltage recording mode and the current sensing in the impedance detection mode. Five in-pixel switches configure the sensing

modality of the tri-modality pixel, and the 144 on-chip tri-modality sensor pixels can be configured independently. The detailed senor pixel circuit operations are presented in the following sections.

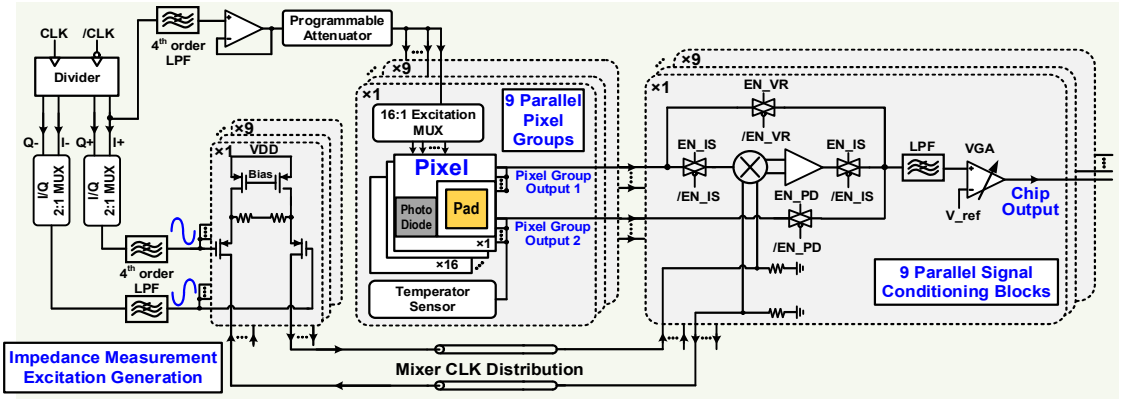

Fig. 2.3. The top-level circuit schematic of the CMOS multi-modality cellular sensor array chip.

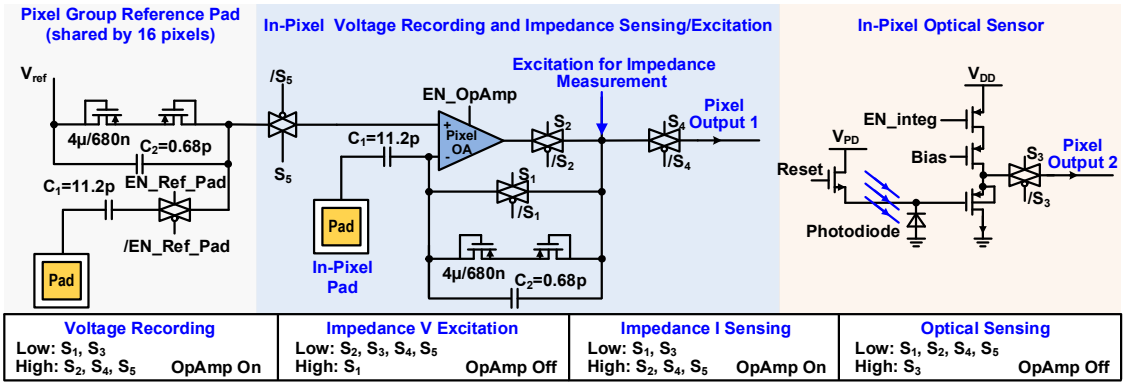

Fig. 2.4. The circuit schematic of the sensor pixel.

Each tri-modality sensor pixel has two electrical outputs. One is the selected output either for the voltage recording mode or the current sensing of the impedance detection mode, while the other output is for the optical sensor (Fig. 2.4). At the pixel group level, the outputs of its 4×4 tri-modality pixels are selected by a 16:1 multiplexer (MUX).

The selected tri-modality pixel output and the temperature sensor reading are then sent to the corresponding signal conditioning block, which comprises a down-conversion mixer, a programmable low-pass-filter (LPF), and an output variable-gain-amplifier (VGA) buffer. Shown in Fig. 2.3, if the selected pixel group output is from the voltage recording mode, it will pass through the switch EN_VR and is fed directly to the LPF and then the VGA buffer. The pixel group optical output or the temperature sensor reading is also fed directly to the LPF and then VGA by the switch EN_PD. On the other hand, if the pixel group output is from the current sensing in the impedance detection mode, it will first be sent to the double-balance mixer by the switch EN_IS for down-convertion (Fig. 2.3). The mixer local oscillator (LO) signal is then sequenctially set as the in-phase (I) and quadrature (Q) signals, so that complex impedance can be coherently detected. The down-converted signal then passes through the LPF to filter out the unwanted mixing tones and the LO leakage, while the VGA serves as the output buffer.

2.3. Sensor Pixel and Pixel Group Implementation

Various circuit sharing techniques are exploited in the tri-modality sensor circuit to achieve compact pixel size and a high spatial resolution. The circuit details are presented below.

2.3.1. Extracellular Voltage Recording Mode

The pixel configuration for the voltage recording mode is shown in Fig. 2.5. In this mode, the control switches S_2, S_4, S_5 and the pixel operational amplifier (OA) are turned on to form a low-noise voltage amplifier, while the switches S_1, S_3, and the optical sensor path are turned off. The capacitor C_1 (11.2pF) blocks the DC voltage offset and drift at the

electrode-electrolyte interface [10] [21]. It also prevents DC currents charging the cells to avoid cellular damages [42]. The pixel OA is a one-stage common-source amplifier with a current-mirror active load.

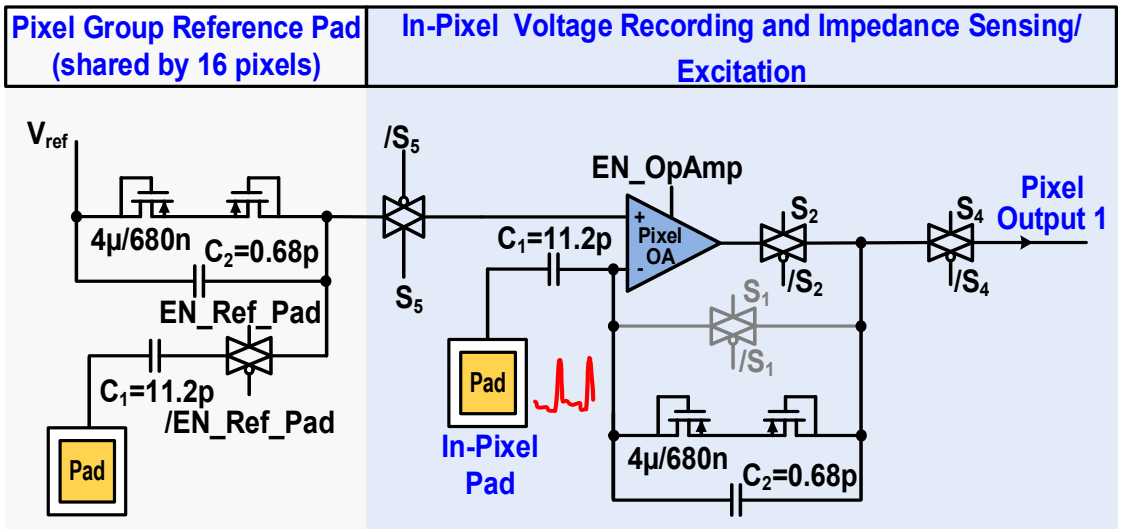

Fig. 2.5. The tri-modality pixel configured for the extracellular voltage recording mode.

The low-noise pixel voltage amplifier amplifies two types of extracellular electrical signals, i.e., the local-field potentials (LFPs) and the action potentials (APs). The LFPs from the neurons represent the averaged electrical activity of the neurons surrounding the recording site with a typical bandwidth from sub-Hz to 300Hz. On the other hand, the action potentials (APs) from cardiomyocytes or neurons representing cellular electrical activity under excitation often with a higher frequency range from 300Hz to 10kHz [43]. The OA in-band closed-loop gain is set by the capacitance ratio of C_1/C_2 as 23.5dB. A MOS-bipolar pseudo-resistor [7] of 230GΩ is employed in the feedback path to bias the inverting input of the OA. This resistor and the feedback capacitor C_2 (0.68pF) provide a low cut-off frequency of 0.5Hz. Such a low cut-off frequency is critical to monitor the

LFPs. Both capacitors C_1 and C_2 are implemented as MIM capacitors, and they are placed beneath the sensing electrode for area saving.

In practice, the MOS-bipolar pseudo-resistor suffers from a leakage current. Due to its large resistance value (230GΩ), even a small leakage current can create a substantial DC voltage drop across the resistor and thus a DC offset between the inverting input and the output of the OA. Extensive simulations across process corners and temperature settings (from 15°C to 45°C) have been performed to characterize this DC voltage drop. The simulated DC voltage drop is less than 230mV, ensuring negligible effects on the OA operation.

The non-inverting input of the in-pixel OA is biased by the reference voltage V_{ref} (1.4V), shared among the 16 tri-modality pixels in each pixel group. To better control the DC output voltage of the in-pixel OA, a replica 230GΩ pseudo resistor and a 0.68pF capacitor are added between the reference voltage V_{ref} and the non-inverting input of the OA. With a similar leakage current and DC voltage drop of the two pseudo resistors, the DC output voltage of the in-pixel OA can closely track the reference voltage V_{ref}.

Furthermore, a differential measurement scheme is employed in the voltage recording mode to suppress the common-mode noise and offset in the measurements. This is enabled by a pseudo reference Au electrode shared among 16 tri-modality pixels in each pixel group. When the switch EN_Ref_Pad is on, the reference electrode samples the background potential and noise of the nearby cellular environment, and this background potential is subtracted by the OA to achieve the differential measurement.

2.3.2. Optical Sensing Mode

For the optical sensing, one reverse-biased p+/nwell/psub photodiode (40μm×40μm) is implemented in each tri-modality pixel (Fig. 2.4). In the optical sensing mode, only the switch S_3 is turned on, while all the other switches and the pixel OA are turned off. The active pixel sensor (APS) architecture [44] is employed here, which consists of an NMOS reset gate, one PMOS source follower, and a PMOS cascode load. During the diode reset, the NMOS reset transistor is turned on and brings the diode cathode voltage to V_{PD}. During the optical sensing, the NMOS reset transistor is off, and the photodiode generates the photon current. This current is integrated over the total parasitic capacitance of photodiode cathode node, and the integrated voltage is buffered by the source follower. The body node of the PMOS source follower is tied to its source terminal to cancel the body effect for improved linearity. In addition, the correlated double sampling (CDS) scheme is used to suppress the reset noise, DC offset, and the device flicker noise [15]. Each photodiode is surrounded by a metal shield to minimize the crosstalk from the adjacent pixels [13].

2.3.3. Impedance Measurement Mode

The cellular impedance measurement mode is configured and performed as follows. One pixel (V-excitation electrode) is first selected for the AC voltage excitation. This voltage excitation initiates an AC current through the nearby cellular structures, and another pixel (I-sense electrode) is enabled to detect this current. Thus, the cellular impedance between these two pixels can be fully characterized. Since arbitrary two pixels can be selected among the 144 tri-modality pixels in the sensor array, the impedance sensing region is fully reconfigurable.

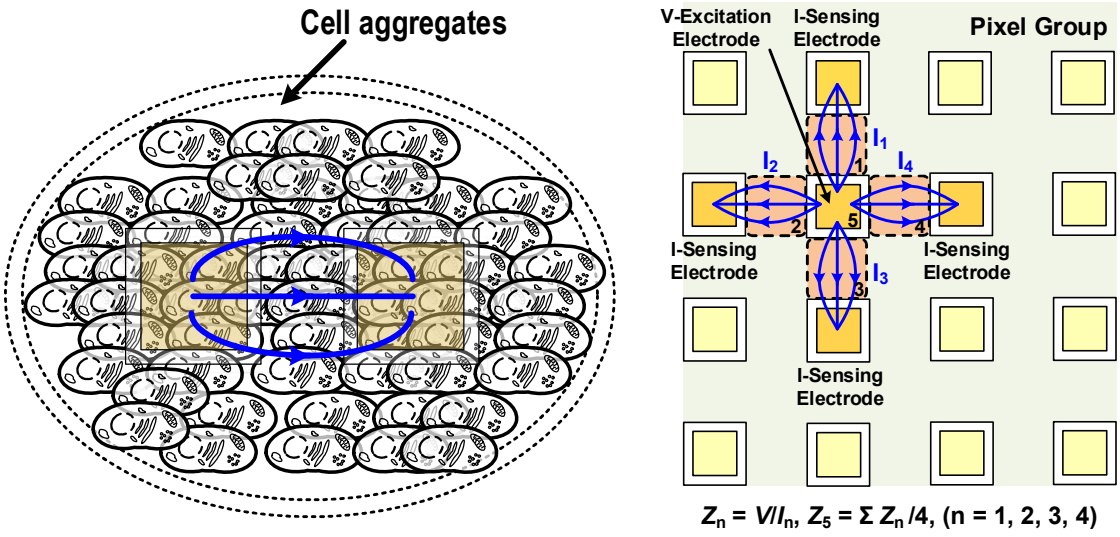

Fig. 2.6. Cellular impedance measurement by voltage excitation and current sensing.

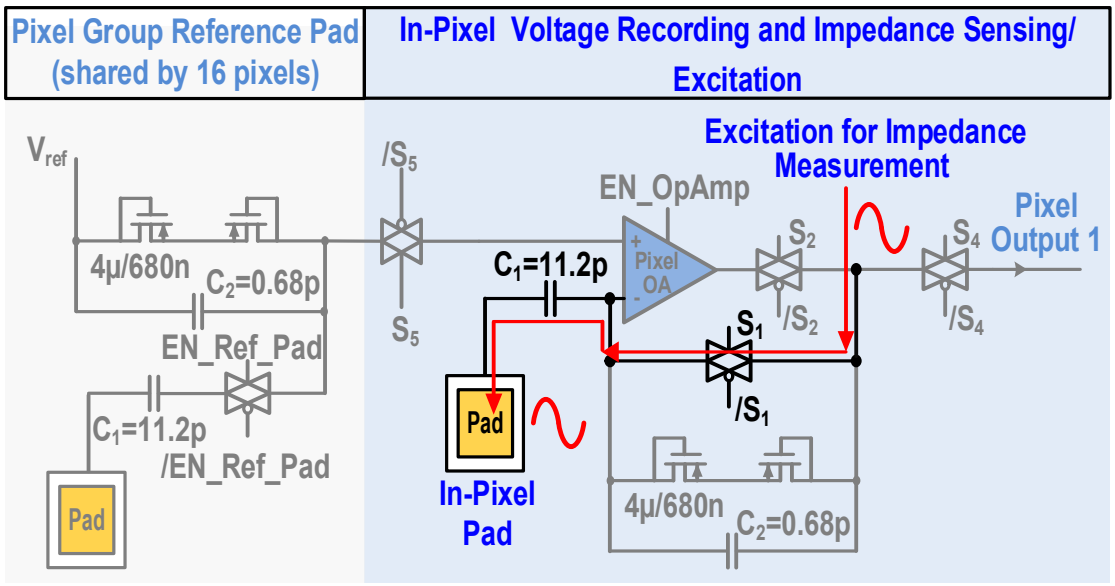

Fig. 2.7. The tri-modality pixel configured for voltage excitation in the impedance measurement mode.

In practice, a 2-dimensional (2D) impedance mapping is highly useful in characterizing the cell location, tissue structure, and cell attachment to the surface. In this 2D impedance mapping, after selecting each voltage excitation pixel (V-excitation electrode), its adjacent four pixels are then sequentially enabled for the current sensing (I-sense electrodes), shown in Fig. 2.6. By measuring the AC currents through the four nearby pixels I_n (n=1, 2, 3, 4), the cellular impedance Z_n (n=1, 2, 3, 4) between the V-excitation electrode and its adjacent I-excitation electrode are measured. Next, the cellular impedance on top of the V-excitation electrode Z_5 is calculated as the average of the impedance values measured with the four nearby I-sensing electrodes. Considering the fact that one pixel group consists of 4×4 electrodes which can be configured as either V-excitation electrode or I-sensing electrode, this leads to a total impedance mapping resolution of 7×7 within one pixel group and 21×21 for the entire array chip.

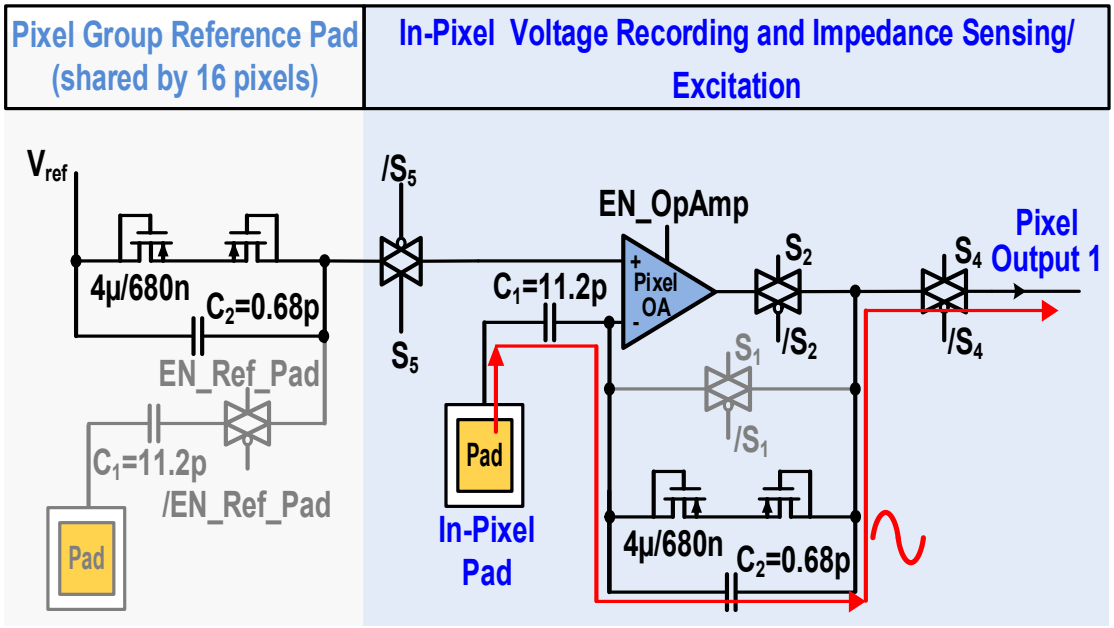

Fig. 2.8. The tri-modality pixel configured for current sensing in the impedance measurement mode.

The pixel front-end circuit configurations for the impedance measurement are further explained below. In the voltage excitation mode, the excitation signal is derived from an off-chip clock (CLK) after a divide-by-2 circuit, and a 4^{th} order reconfigurable LPF suppresses its harmonic signals (Fig. 2.3). A programmable attenuator offers the desired attenuation and avoids saturating the current sensing circuit. The excitation voltage is then buffered by a 1:16 MUX to the selected excitation pixel. Within the excitation pixel (Fig. 2.7), only the switch S_1 is turned on, so that the excitation signal bypasses the pixel OA and fed directly to the electrode.

In the current sensing mode, at the pixel level (Fig. 2.8), the resulting current via the nearby cellular environment first flows through the pixel electrode and is then converted to the voltage signal by the feedback capacitor C_2. The frequency dependence of the capacitive loads (C_1 and C_2) is later calibrated out. The detected current signal is then buffered to the corresponding signal conditioning block (Fig. 2.3). To characterize the complex cellular impedance, a coherent quadrature down-conversion architecture is employed [10]. A double-balanced mixer performs the down-conversion, and its LO signal is derived from the same off-chip CLK signal as the voltage excitation signal to ensure the coherent detection. Note that the divide-by-2 circuit generates the in-phase (I) and quadrature (Q) LO signals, which then sequentially drive the mixer to achieve the complex impedance detection. The reconfigurable LPF after the mixer suppresses the unwanted mixing terms and the VGA buffers the impedance detection outputs (Fig. 2.3).

The impedance measurement mode operates from 500kHz to 4MHz, sufficient to characterize the cellular impedance [45].

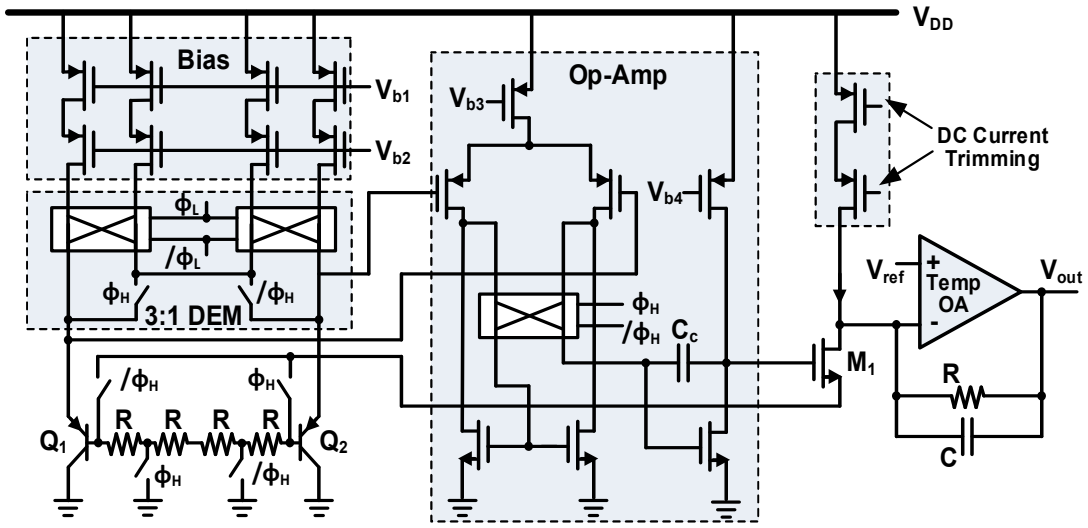

Fig. 2.9. The schematic of the temperature sensor.

2.3.4. Temperature Sensor

The core of the temperature sensor is a Proportional-to-Absolute-Temperature (PTAT) circuit, similar to the design in [24] (Fig. 2.9). Two substrate PNP transistors (Q1 and Q2) are biased by four identical cascode PMOS current sources with the current ratio of 3:1. The dynamic element matching (DEM) and chopper-stabilization schemes are employed to minimize the component mismatches in the PMOS current sources, the resistors, and the PNP transistors, and cancel the OA input DC offset. Several sets of complementary switches controlled by ΦL and ΦH perform the DEM and chopping operations. The DC current offset of the transistor M1 is suppressed by the cascode PMOS trimming current. The nine independent on-chip temperature sensors share the same current trimming signal. Finally, the LPF in the following signal conditioning block suppresses the element mismatches and DC offset and completes the DEM and chopping operations (Fig. 2.3).

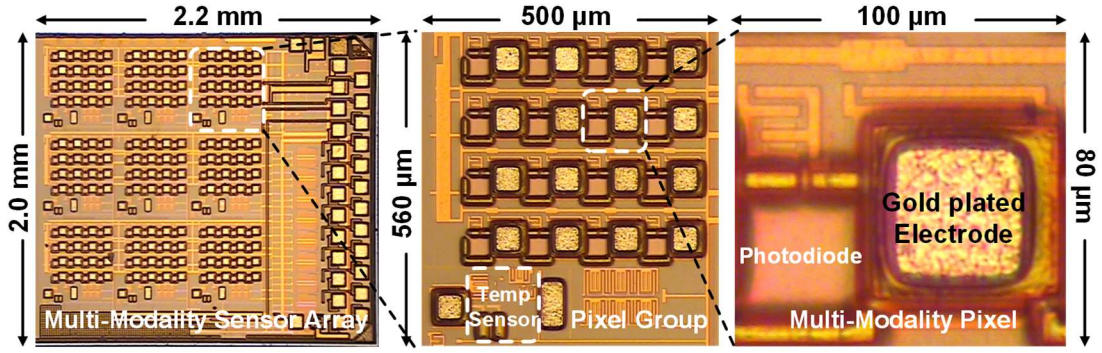

Fig. 2.10. Chip microphotograph of the CMOS multi-modality sensor array chip (left), pixel group (middle), and pixel (right).

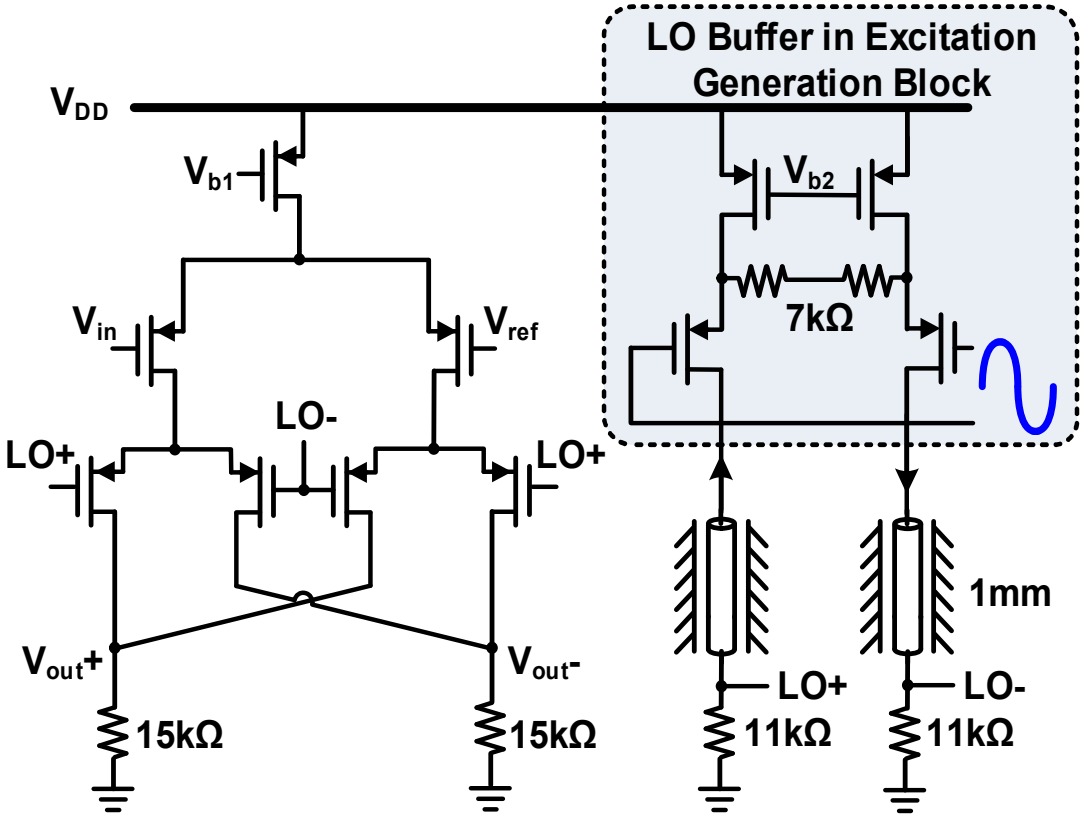

Fig. 2.11. The schematic of the pseudo-differential double-balanced mixer and its LO distribution for down-converting the impedance measurement outputs.

2.4. Signal Conditioning Block

Nine parallel signal conditioning circuit blocks process the outputs from the corresponding parallel pixel groups and enhance the array throughput (Fig. 2.3). The programmable low-pass-filters (LPFs) and the variable-gain-amplifiers (VGAs) directly process the output signals from the voltage recording, optical detection, and temperature sensing modes, while the impedance measurement outputs are first down-converted by the mixers and then processed by the LPFs and VGAs. An on-chip Serial-to-Parallel-Interface (SPI) is integrated for digital programming. The circuit details are presented below.

2.4.1. Down-Conversion Mixer

A PMOS-based pseudo-differential double-balanced mixer is used to down-convert the measured impedance detection signal (Fig. 2.11). The mixer LO signals are derived from the LO buffer in the excitation generation block, and the I/Q LO signals are sequentially applied to the mixer for quadrature down-conversion and coherent detection of complex cellular impedance (Fig. 2.3). Due to the long on-chip routing between the mixer and the excitation generation circuit (around 1mm), shielded transmission line structures are used to distribute the LO signal on-chip with minimized coupling to other circuits.

2.4.2. Programmable LPF and VGA

A programmable second-order Sallen-Key LPF [46] is employed with 3-bit digital controls on its cut-off frequency. To optimize the trade-off between the total integrated noise and the bandwidth in extracellular voltage recording, the cut-off frequency of this

LPF is tunable from 400Hz to 600kHz. The LPF is then followed by a 5-bit VGA with a programmable gain from 0dB to 18dB as the output buffer for the chip.

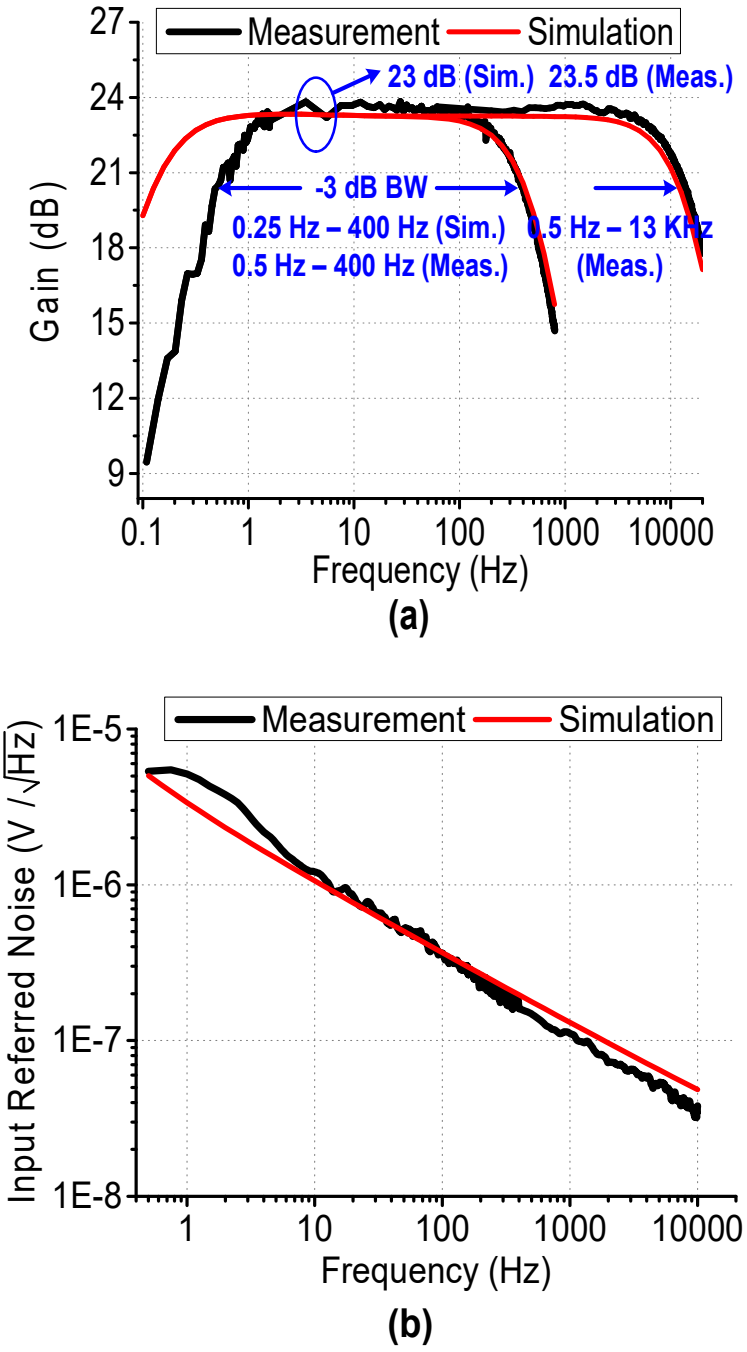

Fig. 2.12. (a) Measured and simulated voltage gain and (b) the input referred voltage noise PSD of the pixel when configured in the voltage recording mode.

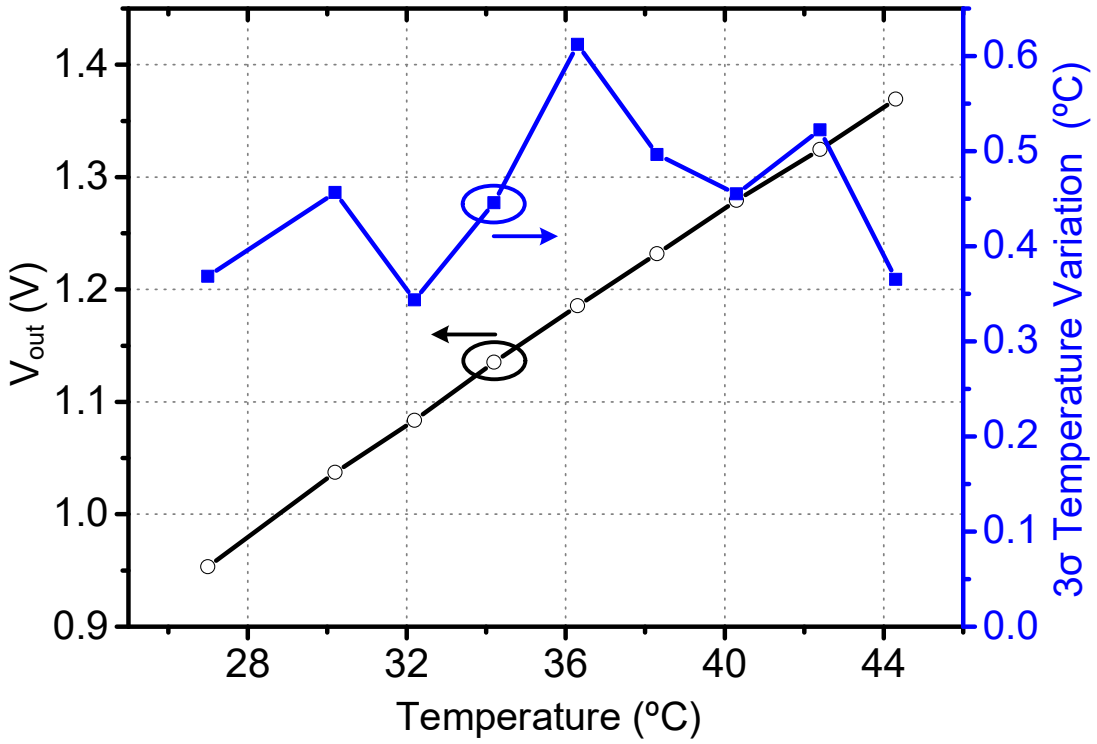

Fig. 2.13. Measured averaged temperature sensor output voltage from the nine on-chip temperature sensors and the 3σ variation versus the ambient temperature.

2.4.3. Voltage Excitation Generation Block

A divide-by-2 circuit based on current-mode-logic (CML) latches are utilized to generate the quadrature LO signals [28]. Glitches during the divided-by-2 operation are removed using a Schmitt trigger. The harmonic tones in the voltage excitation signal will generate harmonic currents through the cells. However, these harmonic currents will be down-converted by the mixer through its harmonic mixing and thus distort the impedance measurement. Therefore, a 4th order programmable Sallen-Key LPF is employed to suppress these harmonic tones in the voltage excitation signal and achieves a 30dB 3rd-

order harmonic rejection. A programmable attenuator is also employed to scale the voltage excitation signal and avoid saturating the current sensing circuit.

2.5. Electrical Measurement Results

The microphotograph of the multi-modality CMOS sensor array chip is shown in Fig. 2.10. The chip occupies 2.2mm×2.0mm in a standard 0.13μm CMOS process. The close-in views of the pixel group (560μm×500μm) and the tri-modality pixel (100μm×80μm) are also shown.

To suppress the 60Hz power-line noise in the measurement, the setup is powered by D-type batteries and enclosed in a grounded metal box for electromagnetic isolation. The digital programming signals for the CMOS chip are generated by the digital I/O channels in a Data-AcQuisition module DAQ (Measurement Computing USB 1608G), while the nine parallel analog outputs from the chip are read by the parallel analog channels of the DAQ module and digitized by its 16-bit analog-to-digital-convertors (ADCs).

To characterize the performance of the voltage recording mode, a Dynamic Signal Analyzer (Agilent 35670A) is used to measure the voltage gain, bandwidth, and the input-referred noise power spectral density (PSD) of the sensing pixels. The voltage gain and the input-referred noise PSD are shown in Fig. 2.12. The measured low cut-off frequency is 0.5Hz with a mid-band gain of 23.5dB, sufficient to detect the low-frequency cellular local field potentials. The difference between the simulated and measured low cut-off frequency is due to the inaccuracy in the modeling of the MOS-bipolar pseudo resistor. The averaged integrated noise from 0.5Hz to 400Hz is 11.1μVrms with a 3σ variation of 3.7μVrms. The averaged integrated noise from 0.5Hz to 10KHz is 12.7μVrms with a 3σ variation of

3.5μVrms. The measurement result matches well with the simulation. The DC power consumption of the pixel OA is 165μW with a supply voltage of 3.3V and a reference voltage of 1.4V.

The temperature sensor is characterized using a temperature chamber (Half Cube Model 105). Figure 2.13 shows the measured averaged output voltage and the 3σ variations from the nine independent on-chip temperature sensors versus the ambient temperature. The temperature sensor response slope is 24mV/ºC. The maximum 3σ temperature variation of the nine temperature sensors is within 0.6 ºC.

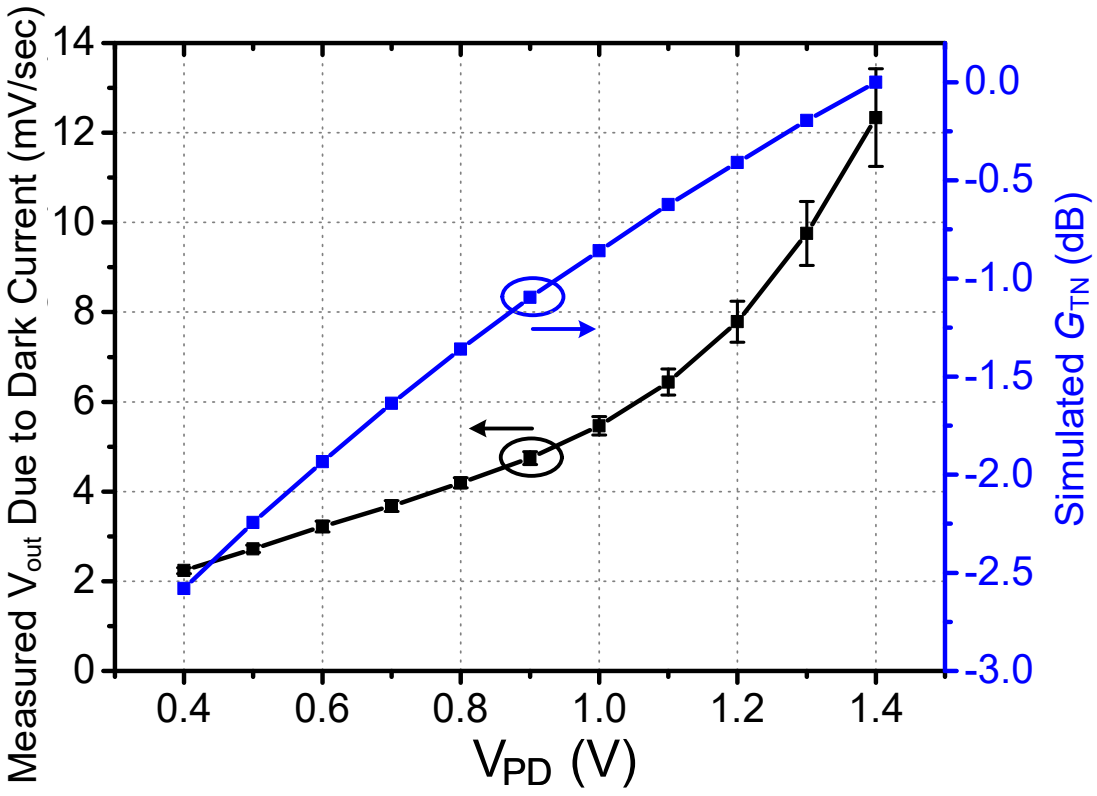

Fig. 2.14. Measured pixel output voltage due to the photodiode dark current and simulated normalized transducer gain of the in-pixel optical sensor versus photodiode biasing voltage VPD.

For the optical detection, the pixel photodiode dark current is characterized at different photodiode biasing voltages VPD (Fig. 2.14). The measurement is performed in a dark room, and the reset frequency is 0.05Hz with a 5% duty cycle. The dark current variation across the entire chip is marked using the error bar at each VPD value in Fig. 2.14. The measured dark current increases substantially if the photodiode biasing voltage is above 1V. However, the transducer gain GT of the optical detection also increases with its reverse biasing voltage due to the decreased diode junction capacitance, as shown in (1) where V_{out} is the output voltage of the source follower (Fig. 2.4), P_{inc} is the incident light power, R_λ is the diode responsivity, T is the integration time, C_{par} is the total parasitic capacitance of the photodiode cathode node, QE is the quantum efficiency, λ is the wavelength, q is the electron charge, ħ is the Planck constant, and c is the speed of the light. The simulated normalized transducer gain GTN is also plotted in Fig. 2.14, where the normalized transducer gain GTN is defined as

$$G_{\mathrm{T}} = \frac{V_{\mathrm{out}}}{P_{\mathrm{inc}}} = \frac{R_\lambda T}{C_{\mathrm{par}}} = \frac{QE\lambda qT}{C_{\mathrm{par}}\hbar c}, \tag{1}$$

$$G_{\mathrm{TN}} = 20\log\left(\frac{G_{\mathrm{T}}}{G_{\mathrm{T}|V_{\mathrm{PD}}=1.4\mathrm{V}}}\right). \tag{2}$$

Assuming a constant diode responsivity R_λ versus biasing voltage, then the normalized transducer gain is the capacitance ratio versus photodiode reverse-biased voltage. Considering the trade-off among the dark current, the transducer gain, and the dynamic range, the photodiode biasing voltage is chosen at 1V for general cellular optical

measurements, such as optical shadow imaging. However, for measurements with a low light intensity, e.g., bioluminescence experiments, a low V_{PD} of 0.4V is used to minimize the dark current.

2.6. Biological Measurement Results

The proposed CMOS multi-modality sensor array supports a large variety of cell-based assays with different sensing modalities, including extracellular LFP and AP voltage recording, electrochemical impedance mapping, optical shadow imaging, and bioluminescence detection. Moreover, as a unique functionality, it also enables concurrent real-time joint-modality measurement to capture complex multi-physics cellular responses during drug or chemical administrations.

In this section, the packaging of the CMOS multi-modality sensor array is first presented. Then, the methods of culturing multiple types of cells on CMOS are introduced. These cells include human cardiomyocytes (CMs) derived from human embryonic stem cells (ESC), mouse neurons (MNs) derived from a progenitor MN green-fluorescent-protein (GFP) reporter mouse ESC line, and a human ovarian cancer cell line (HeyA8-F8). These on-CMOS cultured cells are then utilized for multiple cell measurements and cell-based assays by using the CMOS multi-modality sensor chip. These experiments demonstrate the functionalities of our CMOS multi-modality sensor array.

2.6.1. CMOS Sensor Array Chip Packaging

Gold plating is utilized to treat the pixel electrode and enhance their biocompatibility and robustness for biological measurements [10]-[21] (Fig. 2.10). Besides the gold plating,

this CMOS multi-modality sensor array chip does not require any other post processing step. This makes the solution compatible with low-cost mass production and useful for high-volume applications such as drug screening and development.

The CMOS chip is mounted on a PCB using conductive epoxy. A Polydimethylsiloxane (PDMS) structure provides electrical isolation and seals the bonding wires while maintaining the packaging biocompatibility. The CMOS chip surface is directly exposed to the cell samples and the culture medium. A standard 35mm plastic cell culture dish with drilled-out bottom is mounted on the PCB to hold the cellular samples. A fully packaged module is shown in Fig. 2.15.

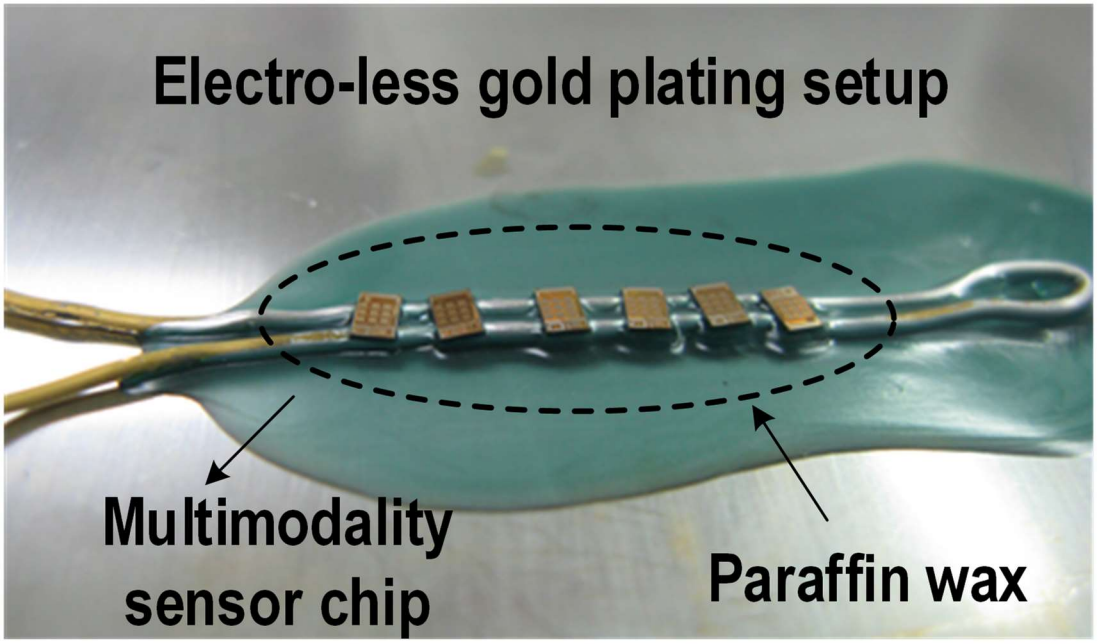

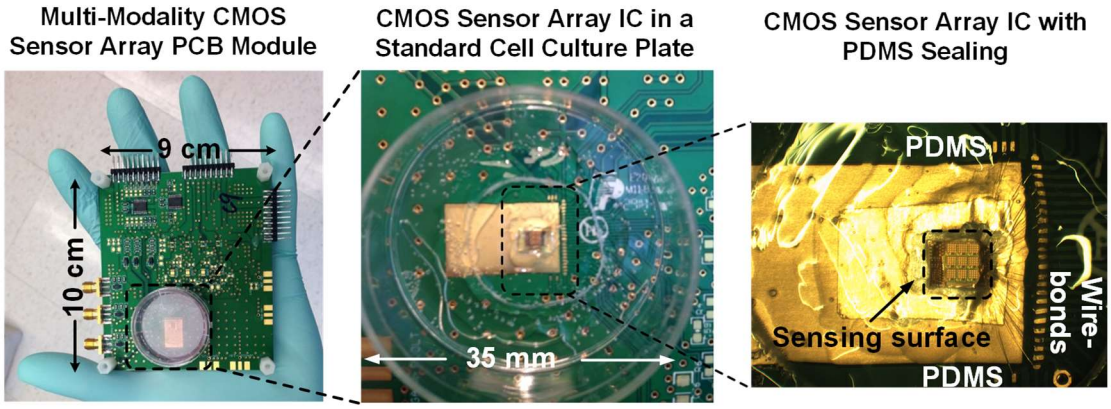

Fig. 2.15. The photograph of a fully packaged multi-modality sensor module.

2.6.2. On-Chip Cell Culture

Human cardiomyocytes (CMs), mouse neurons (MNs), and human ovarian cancer cells are successfully cultured on our CMOS multi-modality sensor chip. The cell culture methods are presented below.

For culturing the mouse neurons (Fig. 2.16a), the TG25 Mouse ESCs are first cultured in a monolayer in the presence of the leukemia inhibitory factor (lif) until reaching 70% confluence. Then, 1000 cell embryoid bodies (EBs) are formed by forced aggregation in micro-wells for 24 hours. EBs are further cultured in suspension on a rotary culture system for 5 more days in the presence of neural induction factors, smoothened agonist (SAG, 1μM) and retinoic acid (RA, 2μM). Finally, the CMOS sensor chip is sterilized using 70% ethanol and coated with laminin, an epithelial cell adhesion glycoprotein. EBs of 1ml are then transferred to the chip surface for maturation and later assay measurements [25].

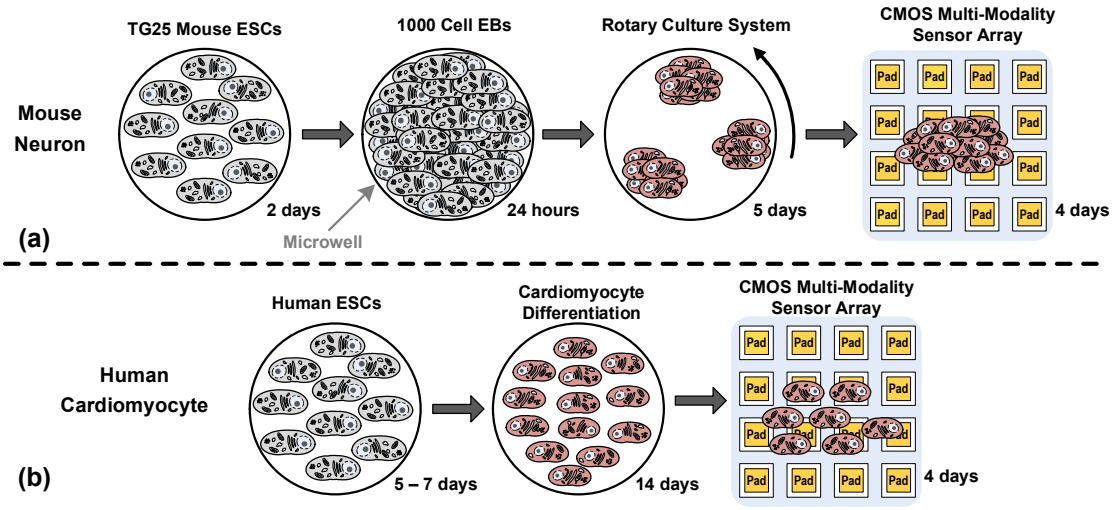

Fig. 2.16. Cell culture steps on CMOS sensor. (a) Mouse Neurons (MNs) and (b) Human Cardiomyocytes (CMs).

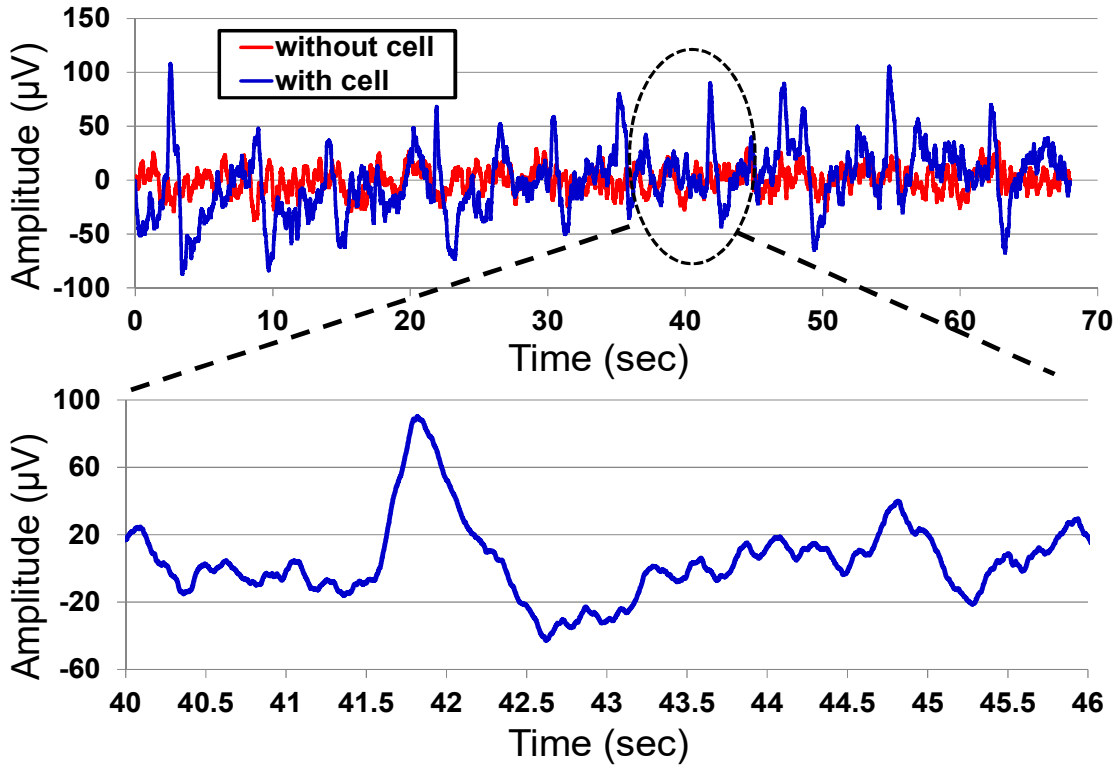

Fig. 2.17. Measured input-referred extracellular voltage recording signals with and without human CM cells.

For culturing the human cardiomyocytes (Fig. 2.16b), human ESCs are first cultured in a monolayer until confluence. Then, cardiomyocytes are directly differentiated through the use of small molecules Gsk3 inhibitor and Wnt inhibitor for 14 days. Finally, the CMOS chip is sterilized using 70% ethanol and coated with a Matrigel matrix as a protein mixture layer to enhance cell culture and attachment. Cardiomyocytes are then seeded onto the CMOS chips as either single cells or aggregated cardio spheres [26].

For culturing the ovarian cancer cells (HeyA8-F8), the CMOS chip surface is sterilized by 70% ethanol and then washed three times with sterile Phosphate Buffered Saline (PBS). To increase cell adhesion to the chip surface, 0.1% gelatin is added onto the chip for 30 minutes before being aspirated. Gelatin is a derivative of collagen and one type of common extracellular matrix protein. Ovarian cancer cells are then seeded directly onto the CMOS chip and allowed to attach before adding 1mL of cell culture media.

2.6.3. Extracellular Potential Recording

Human Cardiomyocytes (CMs) are used for demonstrating the extracellular voltage recording of the CMOS multi-modality sensor array chip. The measured input-referred extracellular voltage recording signals with and without active CM cells are shown in Fig. 2.17. Spontaneous beatings are detected and easily distinguished from the sensor noise floor. The measured period of the autonomous cell beating spikes is about 5~7 s, which is further confirmed by visual inspections through a stereo microscope.

2.6.4. Real-Time 2D Cellular Impedance Mapping for Cell Detachment Experiments

Cell adhesion to the culture surface is essential for the growth and viability of mammalian cells as well as the formation of tissues. Moreover, cell attachment can be utilized to perform cell migration assays, which is widely used in cancer studies [48]. The cells and the culture medium have difference impedance, and typically the cells present higher cellular impedance values. Thus, the cell attachment to the CMOS chip surface can be detected by the 2D impedance mapping. Note that optical detections, i.e., shadow imaging or fluorescence microscopy, only yield the 2D distribution of the cells, and they cannot provide the surface attachment information.

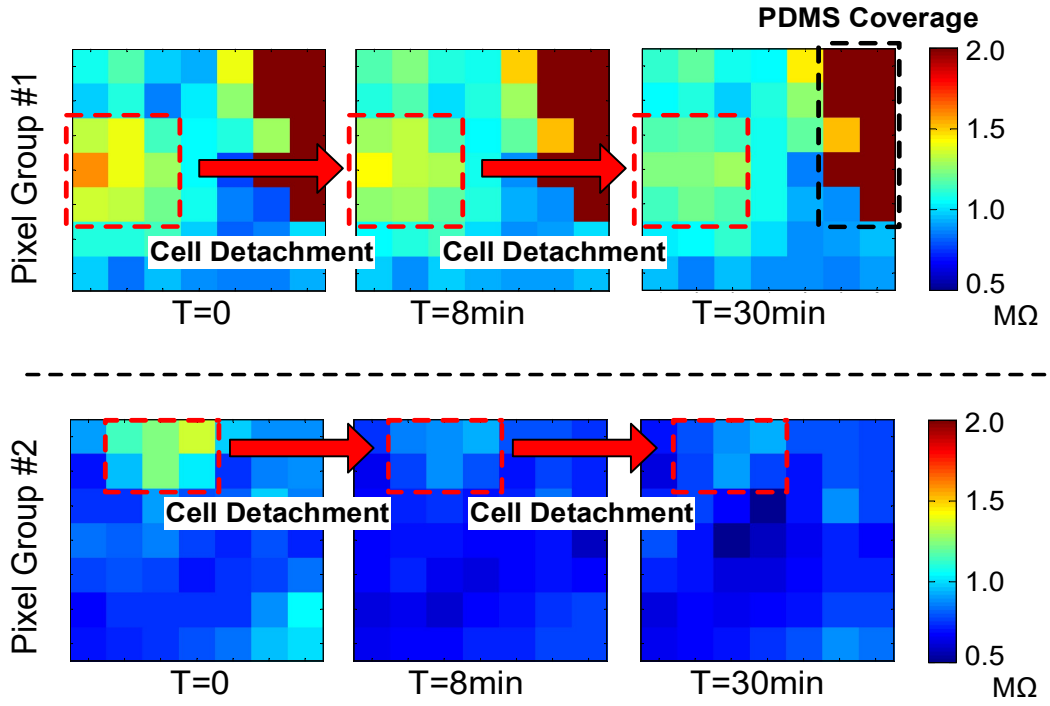

Fig. 2.18. Measured real-time 2D cellular impedance mapping of two pixel groups after accutase administration.

A cell detachment experiment with an excitation frequency of 1MHz and an excitation voltage of 10-100mV is performed to demonstrate that 2D impedance mapping can be used to characterize the cell attachment. On-CMOS cultured human ovarian cancer cells (HeyA8-F8) are used in this demonstration. The cell detachment is triggered by applying accutase to the culture medium, and accutase is a natural enzyme mixture with proteolytic and collagenolytic enzyme activity. It has been widely used in the cell detachment, analysis of cell surface markers, virus growth assays, and tumor cell migration assays [47]. After the human ovarian cancer cells are seeded onto the CMOS multi-modality sensor array chip, accutase is applied to the culture medium, and a real-time 2D impedance mapping is measured versus time. Typically, accutase suspends the cells within 15 minutes. Therefore, after the accutase administration, the measured 2D cellular impedance is expected to first decrease and then stay constant after the cells are fully detached from the CMOS chip surface. The measured impedance mapping results of two pixel groups are shown in Fig. 2.18. A rapid impedance decrease can be seen after 8mins, indicating the cell detachment. The real-time measured impedance values at 8 different sensing pixels are further summarized in Fig. 2.19. The measured impedance values first decrease when accutase is applied and then become constant after full cell detachment. These results align well with the mechanistic effect of accutase. Therefore, the multi-modality sensor array chip can be utilized in cell surface adhesion and cell migration assays, for example studying tumor cell migrations [48].

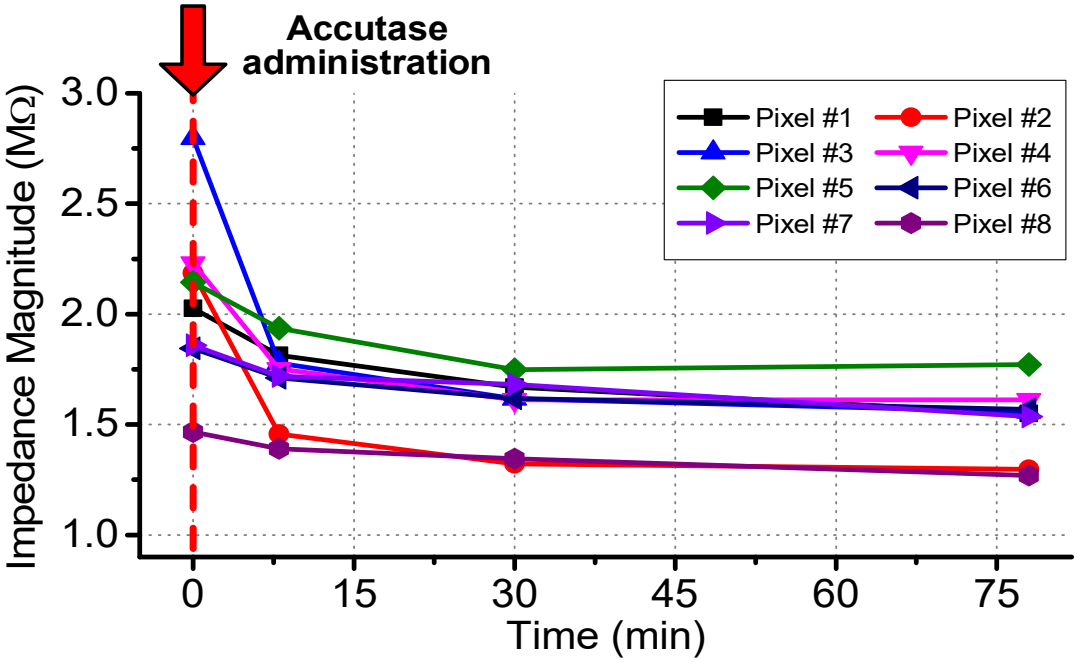

Fig. 2.19. Measured impedance magnitude versus time at 8 different sensing pixels after accutase administration at T=0.

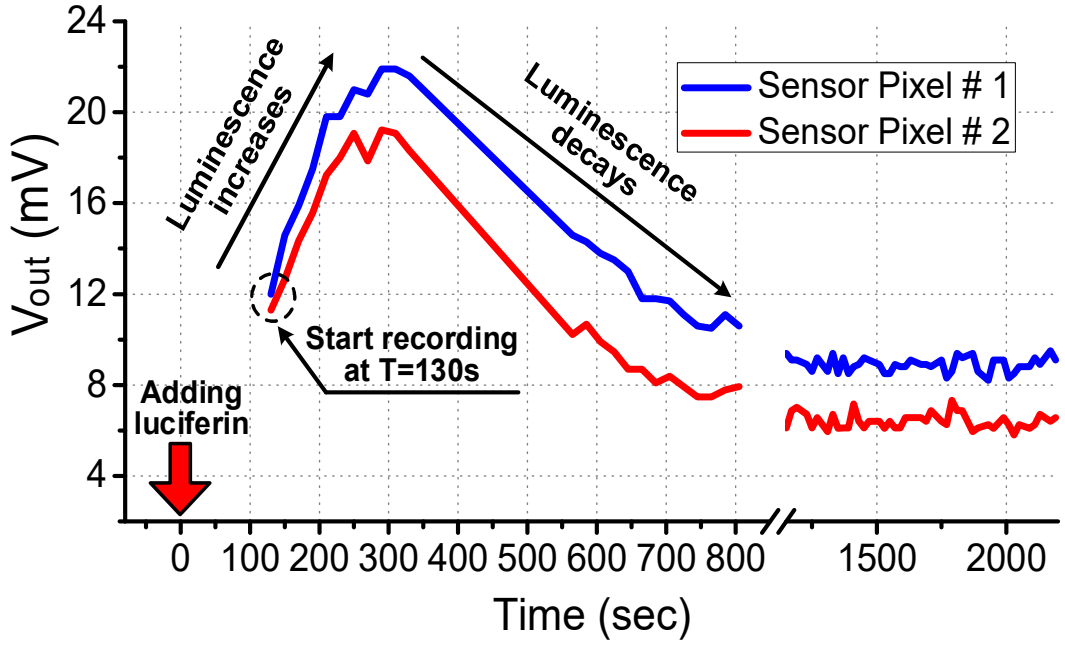

Fig. 2.20. Real-time measured optical sensor outputs at two different sensor pixels for the bioluminescence experiment with human ovarian cancer cells.

2.6.5. Real-Time Bioluminescence Measurement

The human ovarian cancer cells (HeyA8-F8) can constitutively express firefly luciferase. Thus, when luciferin is added to the culture medium, these cancer cells will exhibit luminescence emission. This is because luciferase catalyzes the reaction of luciferin, oxygen, and adenosine triphosphate (ATP) to yield unstable oxyluciferin, which then emits luminescence light during its relaxation back to the ground energy state. In general, upon the luciferin administration, the luminescence emission will reach its peak after about 5 minutes and can be detected for about half an hour, depending on the number of cells and the luciferin concentration. The bioluminescence information can be used to verify the viability of the HeyA8-F8 cancer cells and can be further extended to other bioluminescence cell-based assays.

Since the intensity of the bioluminescence light is generally weak, the background noise, such as the photodiode dark current, should be suppressed and calibrated. The photodiode biasing voltage VPD is set as 0.4V to minimize the dark current (Fig. 2.14). Moreover, dark current in each sensing pixel is recorded before the measurement and then subtracted after the bioluminescence recoding. During the bioluminescence measurement, the culture medium is first removed and immediately replaced with medium supplemented with 200μg/mL of luciferin at T=0. The CMOS sensor chip starts data recording after a 130-second setup time. During the optical detection, the photodiode reset pulse width is 1 second and the repetition rate is 0.05Hz. Thus each photo current integration window is 19 seconds, and the optical detection data is refreshed every 20 seconds. The optical sampling rate is sufficient to record the bioluminescence emission and can be increased if needed. The Correlated Double Sampling (CDS) technique is employed. The measured

bioluminescence emission peaks at around 300 seconds (5 minutes) after the luciferin administration and fully decays after 800 seconds (13.3 minutes). These data agree well with the luciferin mechanistic effect. This real-time bioluminescence experiment demonstrates that the CMOS sensor array chip is capable of measuring low-intensity optical signals and supports bioluminescence as one of the sensing modalities.

2.6.6. Joint-Modality Cellular Measurement with 2D Impedance Mapping and Optical Shadow Imaging

The unique advantage of the proposed multi-modality cellular sensor array is its capability of real-time joint-modality measurement of the same cellular samples, so that the living cells and tissues can be holistically characterized.

In this experiment, we demonstrate a joint-modality cellular measurement with 2D impedance mapping and optical shadow imaging. Mentioned in the Section 2.6.4, the 2D impedance mapping monitors the cell attachment, while the optical shadow imaging can track the location and area information of the cells. On-chip cultured GFP labeled mouse neuron (MN) aggregates are used in this joint-modality experiment.

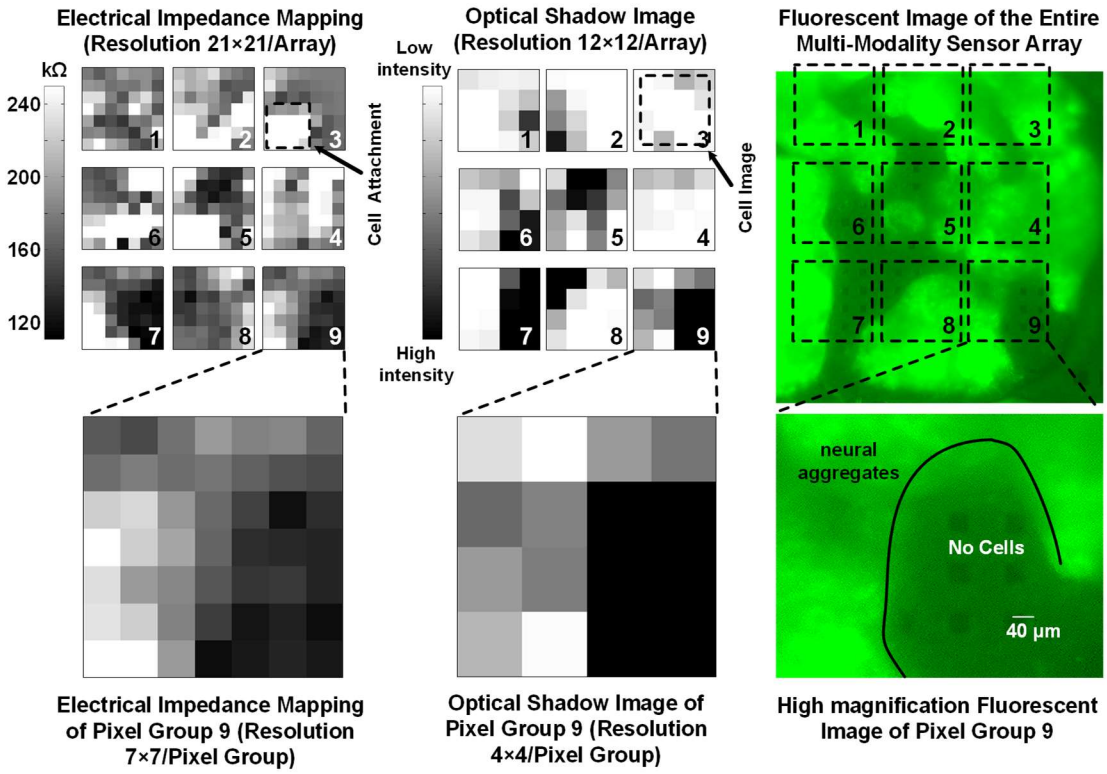

Fig. 2.21. Joint-modality measurement of the on-chip cultured and GPF labeled mouse neuron (MN) aggregates, including the reference fluorescent image (right), the optical shadow image (middle), and the 2D cellular impedance mapping (left).

After the MNs are seeded onto the CMOS chip and reach maturation, a fluorescent imaging is first performed using standard fluorescent microscope as the reference imaging. Then, the optical shadow imaging of the MNs are captured using the underlying CMOS multi-modality sensor array chip. Since both images provide the 2D location and area information of the MN aggregates, a close matching can be found between the two images and shows the functionality of the optical shadow imaging (Fig. 2.21). Next, the 2D cellular impedance mapping is performed by the CMOS sensor array chip with an excitation frequency of 1MHz. Close-in views of the pixel group 9 are also shown in Fig. 2.21.

Although static images are shown, the multi-modality measurements by the CMOS chip are actually performed in a real-time fashion.

Table 2.1. Performance Summary and Comparison with Recently Reported CMOS Biosensor*

	Sensing Modality	Multi-Modality	Sensor Array	Array Pixel Size	On-Chip Cell Assays	Technology
This Work	Voltage Recording + Optical + Impedance + Temperature	✓	✓	80 × 100 μm²	Neuron + Cardiomyocytes + Ovarian Caner	0.13μm standard CMOS
[8]	Voltage Recording	×	✓	7.8 × 7.8 μm²	Snail Neuron	0.5μm standard CMOS
[10]	Impedance	×	✓	90 × 90 μm²	(DNA molecules)	0.35μm standard CMOS
[13]	Fluorescence	×	✓	250 × 250 μm²	(DNA molecules)	0.35μm standard CMOS
[14]	Fluorescence	×	✓	185 × 415 μm²	×	0.25μm standard CMOS
[34]	Magnetic Movement Tracking	×	✓	300 × 300 μm²	Mouse Cardiomyocytes	65nm standard CMOS
[50]	pH+Fluorescence	✓	✓	130 × 130 μm²	×	0.5μm modified CMOS
[51]	pH+Temperature+Impedance	✓	×	N.A.	×	0.35μm CMOS +Nanowire+MEMS
[52]	Pressure+Oxygen+Temperature	✓	×	N.A.	×	0.18μm CMOS + MEMS

* This is a general comparison table for recently reported CMOS biosensors. Please note that these designs are tailored for different biomedical applications.

Note that such a joint-modality cellular characterization provides additional cell information and cannot be achieved by single-modality sensing. For example, the measurement results of the pixel group 3 are highlighted in Fig. 2.21. The 2D shadow imaging indicates that MN cell aggregates are located in most of the region in the pixel group 3, which matches well with the reference fluorescent image. However, the 2D impedance mapping reports low impedance values on the upper right corner of the pixel group 3. This suggests that the MN cells are not fully attached in this upper right corner. This is potentially due to the PDMS packaging at the CMOS chip edge. These real-time

multi-modality measurement results thus demonstrate the unique advantage of the proposed multi-modality sensor.

2.7. Conclusion

This chapter demonstrates a fully integrated multi-modality sensor array in a standard 130nm CMOS process. The sensor array characterizes four different cell physiological parameters, i.e., extracellular voltage recording, cellular impedance mapping, optical shadow imaging/bioluminescence imaging, and temperature monitoring in a real-time joint-modality fashion. Electrical measurements and extensive biological experiments with different types of living cells are performed to demonstrate the functionalities of the proposed multi-modality sensing in holistic cell characterization, cell-based assay and drug screening. Methods for on-CMOS culturing of different types of cells are also presented. A performance comparison with recently reported CMOS biosensors is summarized in Table 2.1.

CHAPTER 3

A HIGH-DENSITY CMOS MULTIMODALITY JOINT SENSOR AND STIMULATOR ARRAY WITH 1024 PIXELS FOR HOLISTIC REAL-TIME CELLULAR CHARACTERIZATION

This chapter presents a fully integrated CMOS multi-modality joint sensor/stimulator array with 1024 pixels for real-time holistic cellular characterization and drug screening. The proposed system consists of 4 pixel groups and 4 parallel signal-conditioning blocks. Every pixel group contains 16×16 pixels, and each pixel includes one 28μm×28μm gold-plated electrode, four 12μm×12μm photodiodes, and in-pixel circuits, within a 58μm×58μm pixel footprint. Each pixel supports real-time extracellular potential recording, optical detection, charge-balanced biphasic current stimulation, and cellular impedance measurement for the same cellular sample. The proposed system is fabricated in a standard 130nm CMOS process. Rat cardiomyocytes are successfully cultured on-chip. Measured high-resolution optical opacity images, extracellular potential recordings, biphasic current stimulations, and cellular impedance images demonstrate the unique advantages of the system for holistic cell characterization and drug screening. Furthermore, this paper demonstrates the use of optical detection on the on-chip cultured cardiomyocytes to real-time track their cyclic beating pattern and beating rate.

3.1. Introduction

Recently, there is an increasing interest to explore hybrid biotic/abiotic systems that utilize built-in cellular machineries in conjunction with micro-/nano-electronics to achieve unprecedented sensing and actuation capabilities beyond conventional electronics-only devices [40] [53]-[55]. Cell-based assays are an excellent example of such "cell-electronics" hybrid systems that present unique advantages for chemical sensing and drug screening [56]-[58]. First of all, compared to traditional biochemical assays, cell-based assays use the actual physiological responses of living cells to discover and examine new drugs, and therefore provide physiologically relevant information to accurately capture the efficacy, toxicity, and metabolism of the drug leads in cellular environments. The cell-based screenings for drug safety and toxicity assessments are critical for new drug discovery. For example, cardiac toxicity is one of the main causes for drug withdrawal from the market [59]-[61]. Moreover, cell-based assays can potentially achieve a high sensitivity and specificity, in that a minute amount of drug can lead to a cascade of physiological responses for signal "amplification" and "filtering" and result in output signals that are easily detectable by electronics. Cell-based assays also support "sample-in-answer-out" fast responses that are mostly limited by the intrinsic response time of the cells [34]. Therefore, cell-based assays have been widely used in numerous high-impact applications such as drug discovery, epidemic disease detection, and environmental monitoring [37] [62] [63]. In addition, cell-based assays are conducive to personalized medicine, as patient derived cells can be employed to test the patient-specific potency, efficacy, and toxicity of drugs.

To implement micro-/nano-electronic cellular sensors and actuators, CMOS processes have become a very promising technology platform due to their high spatiotemporal resolution, unparalleled analog and digital signal processors, low power, low cost, and high level of integration. A wide variety of single-modality CMOS cellular sensors have been successfully demonstrated to capture one category of cellular physiological responses, e.g., neural recording and stimulation systems [7]-[9] for measuring neuron activities, electrical impedance sensors [10] [12] [64] for cell-growth assay and detecting myocardial ischemia, pH sensors for cellular metabolism assay [65]-[67], magnetic cell-based sensor for measuring cardiac beating rate [34] [68] [72], and optical sensors [13]-[15] for DNA sequencing. In parallel, CMOS actuators support various cellular manipulation, including electrical [73], optical [74], thermal [75], and magnetic [53].

However, when exposed to drug or biochemical stimulus, cells often exhibit complex behaviors that demand multi-physics and multi-parametric modeling. Therefore, a holistic understanding of cells with multi parametric cellular responses is of paramount importance [31]. The key objective is to real-time capture multi-physical cellular physiological responses from the same cellular sample with a high spatiotemporal resolution. In addition, it is highly desired to support cellular stimulations or actuations, which enable various in-depth cellular studies. For example, electrical stimulation promotes the cardiac differentiation of human cardiac progenitor cells [76], and the maturation of cardiomyocytes derived from human embryonic stem cells [77], and it also can be used to study cellular behaviors under various neurological and cardiovascular diseases[78]-[82].

Despite many successful demonstrations of single-modality cellular sensors, such multi-modality cellular interface platform however remains elusive. A 144-pixel multi-modality sensor array [16]-[18] including in-pixel extracellular potential recording, impedance sensing, and optical detection, is implemented with a pixel size of 80μm×100μm, electrode size of 40μm×40μm, and photodiode size of 40μm×40μm. However, this multi-modality cellular sensing array suffers from poor spatial resolution, since each sensing pixel needs to integrate complex in-pixel circuits for multi-modal sensing.

To address these challenges, in this chapter we present a 1024-pixel multi-modality CMOS cellular interfacing array with joint sensor and stimulator for holistic real-time cellular characterization and drug screening applications [19]-[20]. Each pixel can be independently configured to perform extracellular potential recording, cellular impedance sensing, and optical detection, as well as charge-balanced biphasic current stimulation. Each pixel contains a 28μm×28μm gold-plated electrode and four 12μm×12μm photodiodes, achieving 1024 multimodality pixels and 4096 optical detection sites with a total cellular interfacing field-of-view (FoV) of 1.85mm×1.85mm. The rat cardiomyocytes are successfully cultured on the CMOS chip surface coated with fibronectin. The measured optical shadow images of on-chip cultured rat cardiomyocytes achieve high spatial resolution and closely match the reference stereomicroscope images; this obviates the use of bulky and expensive conventional optical setups for applications where contact-based cell imaging is sufficient. Extracellular potential recordings are also performed at multiple pixels with the on-chip cultured rat cardiomyocytes and successfully capture the transient cardiomyocytes extracellular potentials with high signal-to-noise ratio (SNR) to measure

cardiac beating rates. In addition, we demonstrate that transient cardiac muscle contraction and relaxation events as well as their beating rates can be captured by real-time optical detection using our CMOS platform. This chapter is organized as follows. Chapter 3.2 shows the system architecture and circuit details of the 1024-pixel CMOS multimodality cellular interfacing array. Chapter 3.3 describes in-house biocompatible packaging techniques for CMOS multimodality cellular interfacing array chip. The CMOS chip electrical characterizations are shown in chapter 3.4, and comprehensive cell-based measurements with on-chip cultured rat cardiomyocytes are presented in chapter 3.5.

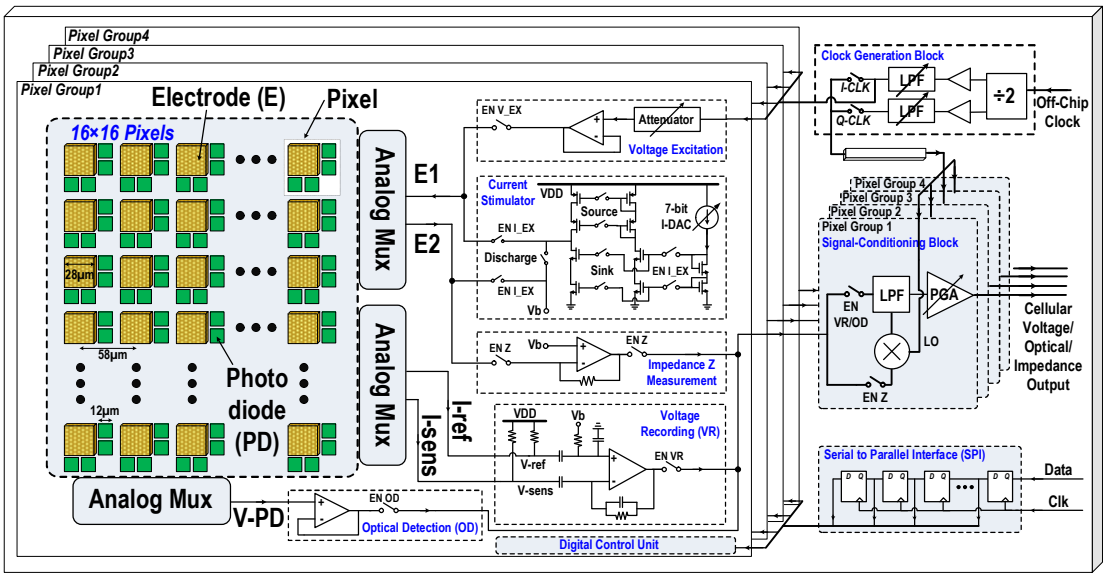

Fig. 3.1. The system-level schematic of the proposed 1024-pixel CMOS multimodality cellular interfacing array.

3.2. Multi-Modality Joint Sensor/Stimulator Array Design

The system-level schematic of the proposed 1024-pixel CMOS multimodality cellular interfacing array is shown in Figure 3.1. It consists of 4 parallel pixel groups, 4

corresponding signal-conditioning blocks, a clock generation block, and a serial-to-parallel-interface (SPI) circuit. Each pixel group contains 16×16 multimodality pixels and shared circuits, including a voltage excitation buffer, a 7-bit charge-balanced biphasic current stimulator, a trans-impedance amplifier (TIA), a low-noise amplifier, an optical detection buffer, and a digital control unit. Each pixel has one 28μm×28μm electrode, four 12μm×12μm photodiodes, achieving total 1024 multimodality pixels and 4096 optical detection sites per CMOS multimodality cellular interfacing array chip. The signal-conditioning block includes a double-balanced mixer, a programmable low-pass filter, and a programmable gain amplifier to further process output cellular signals. The clock generation block includes a divide-by-2 circuit, programmable 6^{th}-order low-pass filters, and buffers for coherent complex impedance sensing.

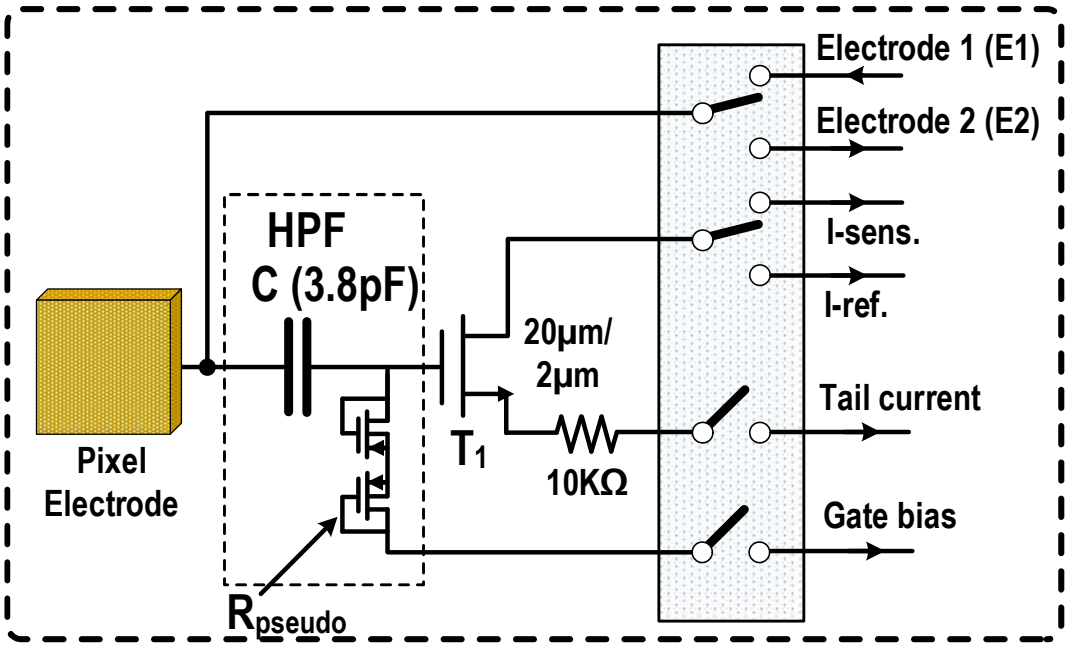

Fig. 3.2. In-pixel circuit for extracellular potential recording, complex impedance sensing, and charge-balanced biphasic current stimulation.

The in-pixel circuit for extracellular potential recording, complex cellular impedance sensing, and charge-balanced biphasic current stimulation is shown in Figure 3.2. It consists of a gold-plated electrode, a series DC blocking capacitor (3.8pF), a single transistor amplifier (W/L=20μm/2μm), a pseudo resistor (≈400GΩ), a degeneration resistor (10kΩ), and reconfiguration switches. Controlled by the switches, the electrode is either directly coupled to the shared circuits in the pixel group for complex impedance sensing and biphasic current stimulation (electrode 1 and electrode 2 in Figure 3.2) or ac-coupled to the in-pixel single transistor amplifier for extracellular potential recording (I-sens., I-ref., tail current, and gate bias in Figure 3.2). The in-pixel circuit for optical detection is shown in Figure 3.3. It includes a reverse-biased p+/nwell/psub photodiode, an NMOS transistor for periodic reset, and a PMOS source follower for readout [16]-[18]. Each photodiode is shielded by metal walls (metal and via) to achieve optical isolation.

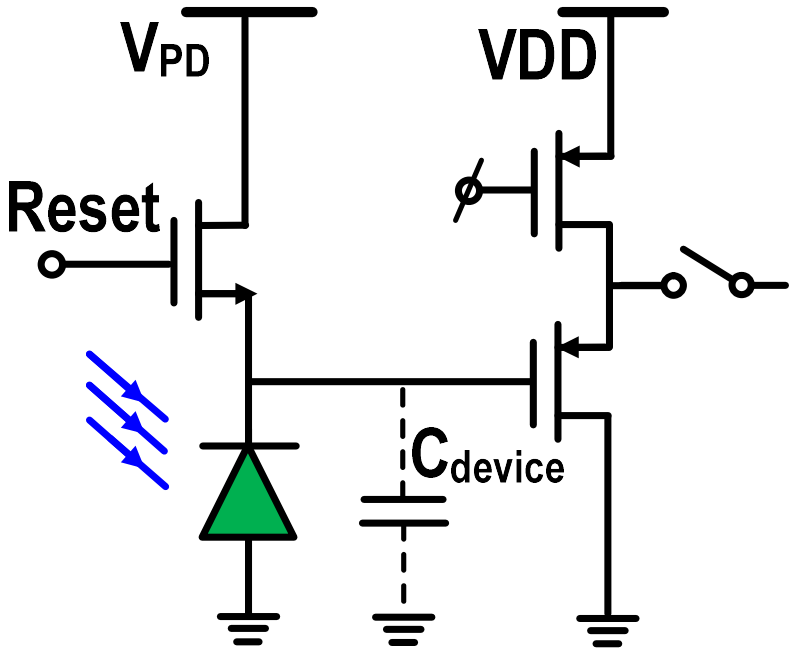

Fig. 3.3. In-pixel circuit for optical detection.

For optical detection, the photodiode cathode is first charged to the photodiode reverse-bias voltage V_{pd} with a short duration reset pulse. Then, the generated photocurrent discharges the cathode node until the cathode node potential become 0, which is buffered out by the PMOS source follower. Note that the input-referred voltage dynamic range at the cathode node is from V_{pd} to 0 and each pixel has 4 photodiodes and their corresponding readout circuits.

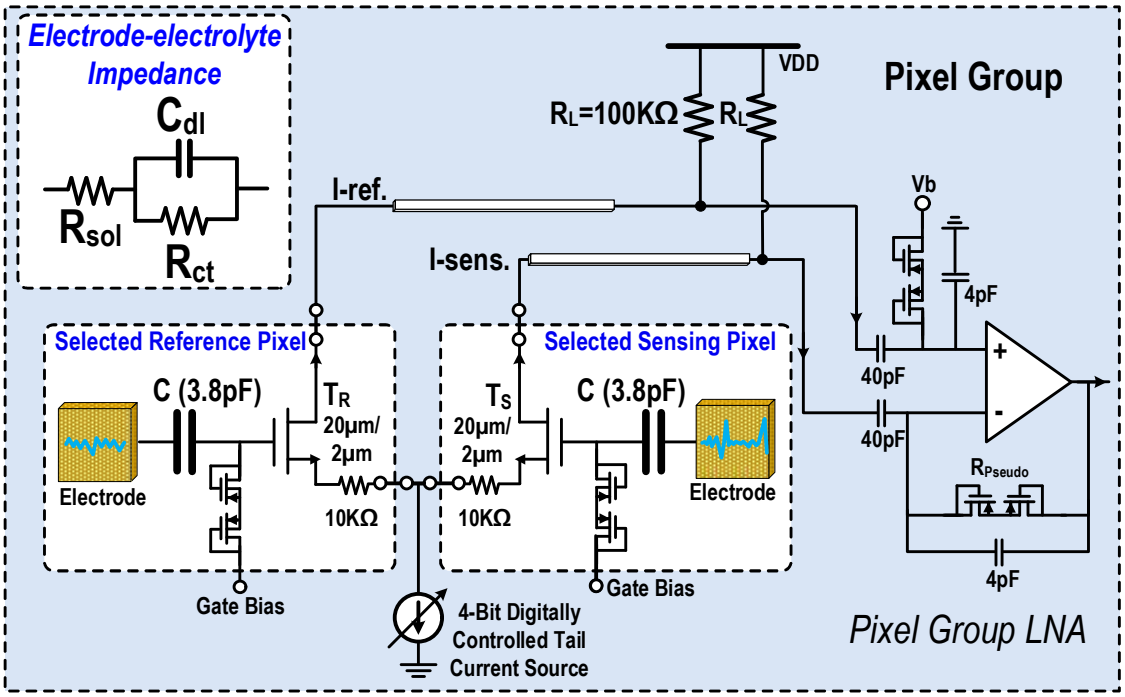

Fig. 3.4. Circuit schematic when two pixels within one pixel group are configured for differential extracellular potential recording.

Next, we will present the circuit details when the pixel group is configured for extracellular potential recording. Figure 3.4 shows the circuit schematic in this modality configuration. First, two pixels can be arbitrarily selected from the same pixel group (total

256 pixels) to perform differential cellular potential detection with one pixel for the sensing and the other pixel as the reference. Two in-pixel transistors T_R and T_S, load resistors R_L implemented in pixel group, and 4-bit digitally controlled current source implemented in pixel group are configured as a fully differential amplifier with high-pass response. The voltage gain of the front-end amplifier is programmable from 5dB-to-14dB with high-pass lower cut-off frequency of 0.1Hz, which is sufficient to accurately capture low-frequency local field potential. Compared to the active sensor pixel architecture where a low noise amplifier is implemented in each pixel [16]-[18], only one transistor is implemented in each pixel in this design, achieving a substantial pixel size reduction. In addition, compared to the passive sensor pixel architecture [9], the cellular voltage signals are first converted to current signals in pixel by the differential amplifier and then distributed in the current mode; this differential current-mode signaling minimizes the capacitive cross talk among pixels and achieves a fully differential measurement for high common-mode rejection. The detected biopotential signals are further amplified by pixel group low-noise amplifier with 20.3dB voltage gain. The in-pixel degeneration resistor of 10kΩ is used to desensitize the mismatches between the sensing pixel transistor T_S and the reference pixel transistor T_R and between the sensing pseudo resistor and the reference pseudo resistor. The resistor loads R_L of 100kΩ are implemented in each pixel group instead of PMOS loads to minimize flicker noise. The thermal noise generated by the gate bias resistor (pseudo resistor) is filtered out through the double-layer capacitor C_{dl} at the electrode-electrolyte interface [21] shown in Figure 3.4 and the external solution bias electrode. The simulated integrated input-referred noise is $10.5\mu V_{rms}$ for the local field potential band (1-to-300Hz), $7.7\mu V_{rms}$ for the action potential band (300-to-6000Hz), and $12.1\mu V_{rms}$ for cardiomyocytes

recording (1-to-2000Hz). The 4-bit digitally controlled tail-current source implemented in pixel group can adjust the tail current between 2.5μA to 37.5μA. The voltage gain of the programmable gain amplifier (PGA) in the signal-conditioning block is adjustable from 1.7dB to 18.0dB, and therefore the total voltage gain is between 27dB and 52.3dB.

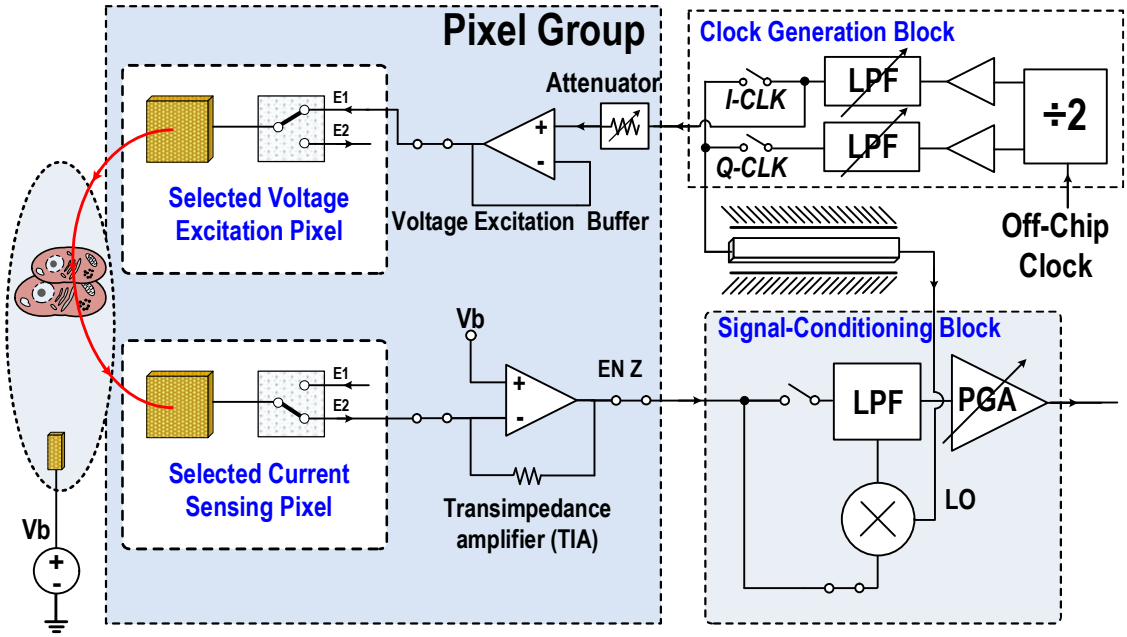

Fig. 3.5. Circuit schematic when the pixel group is configured for coherent complex impedance sensing modality.

Figure 3.5 shows the circuit schematic when the pixel group is configured for coherent complex impedance sensing. First, two adjacent pixels are selected with one for voltage excitation and the other for current sensing. The two selected in-pixel electrodes (E1 and E2) are DC-coupled and connected to voltage excitation buffer and current sensing TIA, respectively. The operation of coherent complex impedance sensing is as follows. First of all, the fully differential quadrature sinusoidal signals are generated by current-

mode logic divide-by-2 circuit and programmable 6^{th}-order low-pass filter. The in-phase signal is fed into the programmable attenuator and then drives the voltage excitation electrode. The resulting cellular current is flowing into the current-sensing pixel electrode, converted to an output voltage signal by TIA, frequency down-converted by the mixer, low-pass filtered, and further amplified by a PGA. The differential quadrature signals are sequentially applied to the mixer local oscillator (LO) port to coherently detect the complex cellular impedance. The simulated total trans-impedance gain for the current sensing chain is 4.6MΩ, including TIA gain of 129KΩ, mixer conversion gain of 13dB, and programmable gain amplifier gain of 18.0dB. The simulated total output voltage noise divided by the total trans-impedance gain with a mixer LO frequency of 100kHz and then integrated over a low-pass filter bandwidth of 700Hz is $54.1pA_{rms}$. Since electrodes are DC-coupled, equal DC bias points are critical for reliable impedance sensing and maintaining long-term electrode integrity [21]-[23] [83]-[85]. The voltage excitation buffer output DC voltage, culture medium external DC bias voltage, and input DC voltage of the TIA are set to V_b=VDD/2 to minimize undesired faradaic charge transfer [85]. In addition, the sinusoidal voltage excitation amplitude is kept below 50mV. The minimum impedance sensing time is determined by the programmable low-pass filter RC settling time in the signal-conditioning block after the mixer. With a low-pass filter cut-off frequency of 0.7kHz, the sinusoidal voltage excitation time is kept less than 4ms to minimize undesired electrochemical reaction at the electrode-electrolyte interface [85]. The electrode-electrolyte interface impedance can be modeled as solution resistance R_s in series with the double-layer capacitance C_{dl} in parallel with charge transfer resistance R_{ct} for simplicity [21] shown in Figure 3.4. The double-layer capacitance with the electrode size of

30μm×30μm for a gold electrode is between 50pF~100pF [23]. Therefore, we choose a relatively high frequency (100kHz-to-1MHz) to minimize the artifacts due to electrode-electrolyte interface impedance and achieve precise cellular impedance sensing.

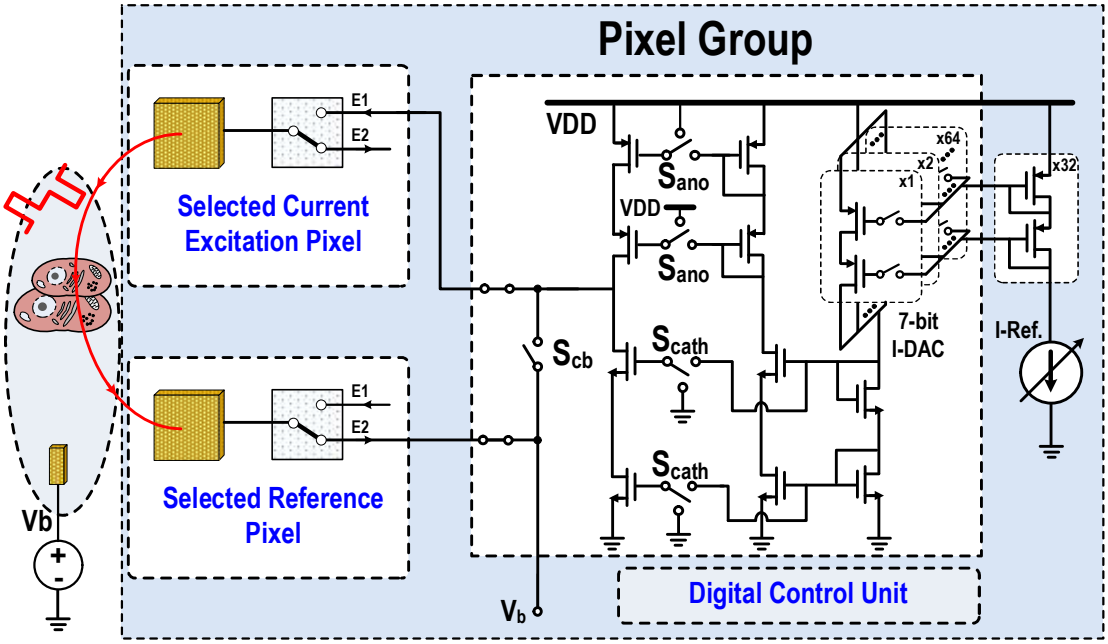

Fig. 3.6. Circuit schematic when the pixel group is configured for the charge-balanced biphasic current stimulation.

The charge-balanced biphasic current stimulation is critical for electrode safety and preventing cell damages, and its related circuits are shown in Figure 3.6. Two adjacent pixels are first selected with one for current stimulation and the other for reference/termination. Cathodic current (S_{cath}), anodic current (S_{ano}), and passive charge balancing (S_{cb}) periods are sequentially enabled to complete the biphasic current stimulation and preserve charge balancing for electrode safety [21]-[23] [83]-[85]. A 7-bit current digital-to-analog converter (I-DAC) and analog coarse control for I-DAC reference

current (I-Ref.) are implemented to cover biphasic current-stimulation range from 100nA to 32µA. The current strength, cathodic/anodic pulse width, interphase delay, and inter-pulse interval are fully programmable through SPI.

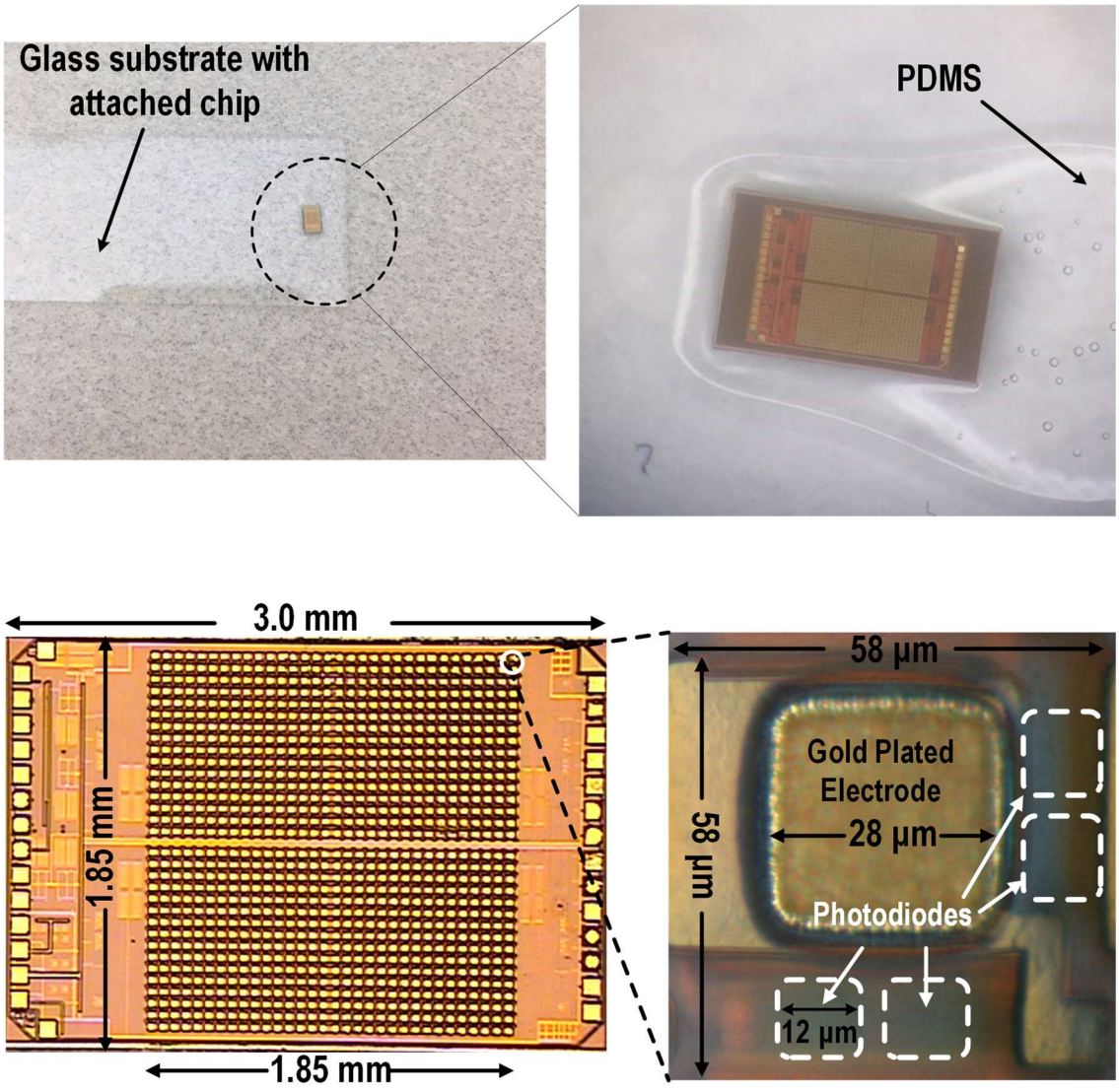

Fig. 3.7. Chip microphotograph.

3.3. In-House Biocompatible Packaging

The 1024-pixel CMOS multi-modality cellular interfacing array is fabricated in a standard 130nm CMOS process with a chip area of 2mm×3mm (Figure 3.7). Each pixel occupies 58µm×58µm and contains a 28µm×28µm gold-electrode and four 12µm×12µm photodiodes. Thus, each CMOS array chip achieves 1024 multimodality pixels and 4096 optical sensing sites with a wide FoV of 1.85 mm×1.85 mm.

Since the chip directly interfaces with living cells and corrosive culture medium, biocompatible packaging with high-quality sealing is critical to prevent chip damage and permit the long-term drug effect studies using living cells [86] [87]. Standard CMOS processes, however, mostly use aluminum as the top metal layer and polyimide for the top passivation dielectric layer. To protect the aluminum electrodes in the culture medium, an electro-less gold plating procedure of aluminum-zinc-nickel-gold composite layers is applied to the bare CMOS chips and explained as follows. First, a diced CMOS chip is attached to the glass substrate with black wax for easy handling. The chip is then washed with acetone, methanol, and isopropyl alcohol, and further cleaned with oxygen plasma ions. Next, the diced CMOS chip on the glass substrate is immersed in aluminum etchant (TRANSENE) and then nitric acid to completely remove the aluminum oxide layer on the aluminum metal pads. Finally, the diced chip on the glass substrate is sequentially immersed into off-the-shelf zinc (Zincate, TRANSENE), nickel (Nickelex, TRANSENE), and gold (Immersion gold CF, TRANSENE) solutions following the electro-less gold plating procedure. As the last step, the chip is immersed in an autocatalytic gold solution (AuBEL, UYEMURA) to thicken the gold layer up to 1µm.

The electro-less gold plating process is a self-limiting process, resulting in the maximum plated gold thickness upto 200nm-to-300nm. This is because the gold can only be grown on the other seed layers such as Nickel for our case and cannot be grown on top of the gold. However, the deposited gold layer with the thickness of 200nm-to-300nm is not enough to fully cover the electrodes and/or to reliably protect the electrodes. This is particularly important for the long-term cell culturing and long-term cell-based measurements. Furthermore, compared to the passive sensing such as extracellular potential recording, the actuation such as biphasic current stimulation and voltage excitation for impedance sensing requires enhanced aluminum electrode protections.

Therefore, after the immersion gold plating process, we immerse it into autocatalytic gold solution (AuBEL, UYEMURA). With autocatalytic process, the gold can be grown on top of the gold and thus gold layer thickness can be enhanced upto 1µm.

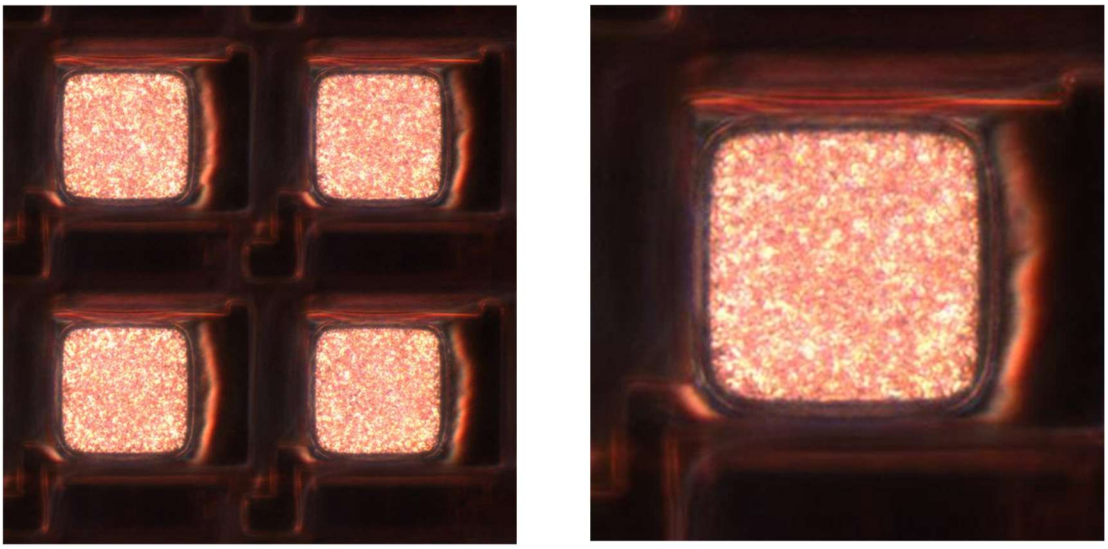

Fig. 3.8. (a) Dark-field microscope image of the electrodes after immersion gold process.

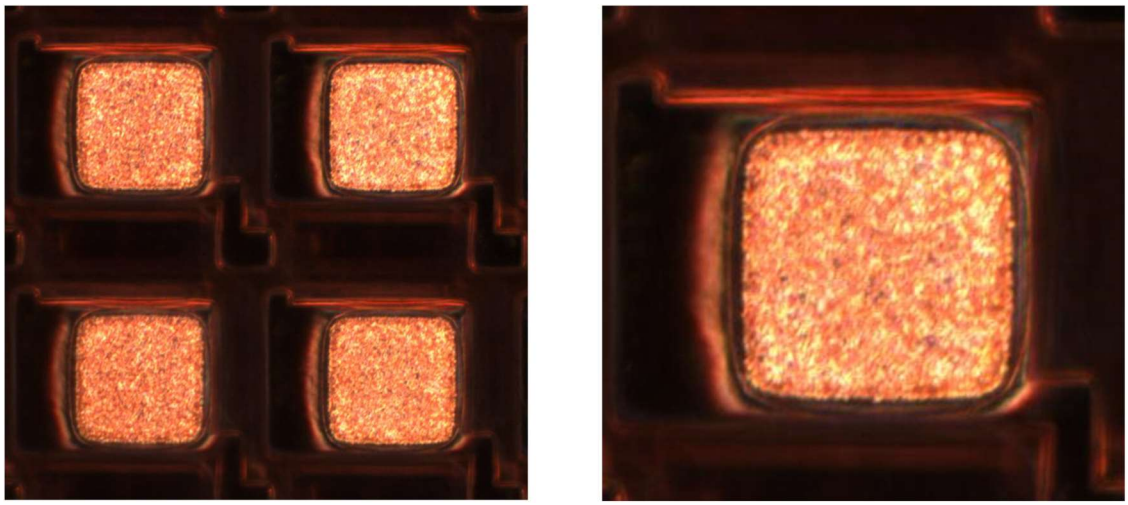

Fig. 3.8. (b) Dark-field microscope image of the electrodes immersed in the autocatalytic gold solution for 1 minute after immersion gold process.

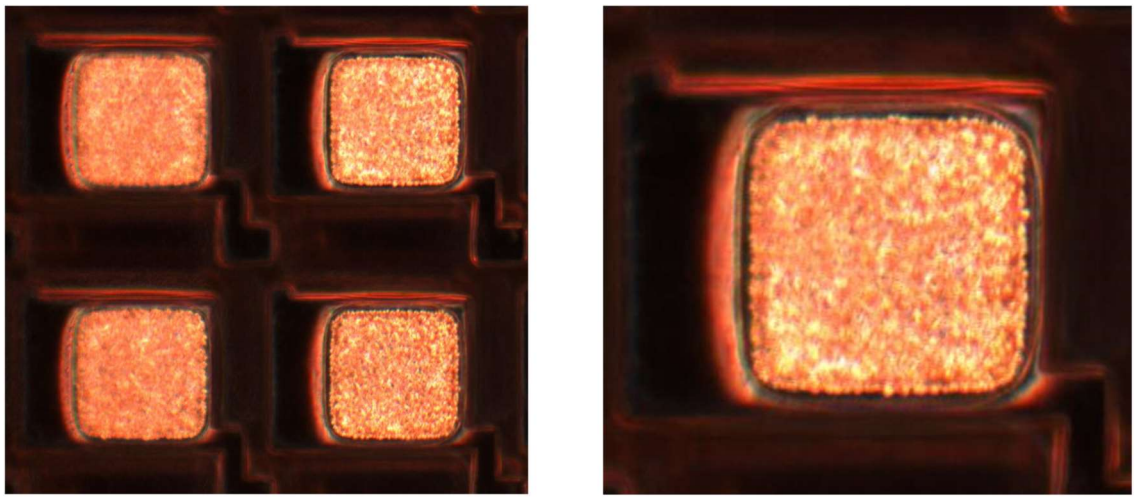

Fig. 3.8. (c) Dark-field microscope image of the electrodes immersed in the autocatalytic gold solution for 2 minutes after immersion gold process.

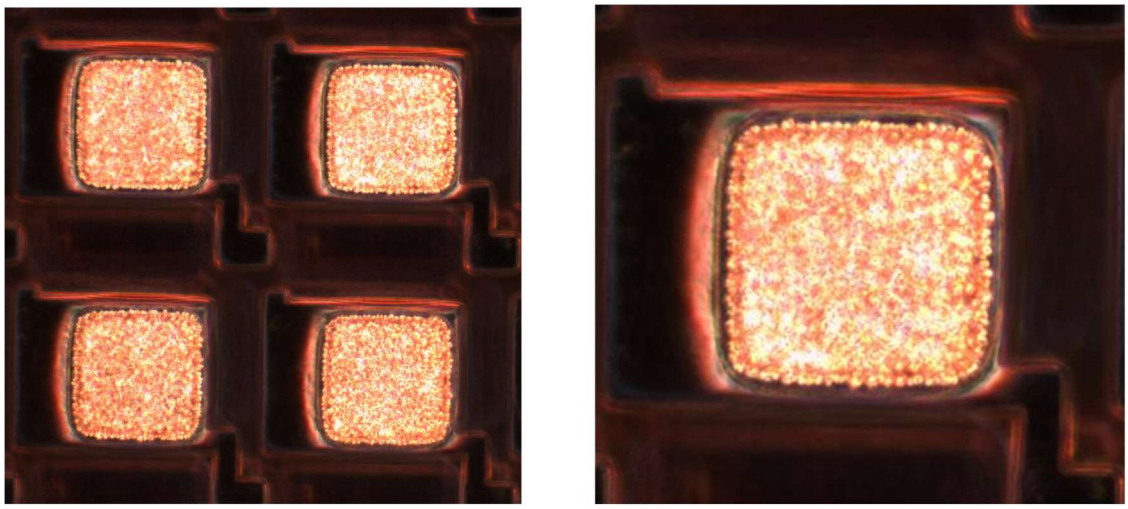

Fig. 3.8. (d) Dark-field microscope image of the electrodes immersed in the autocatalytic gold solution for 3 minutes after immersion gold process.

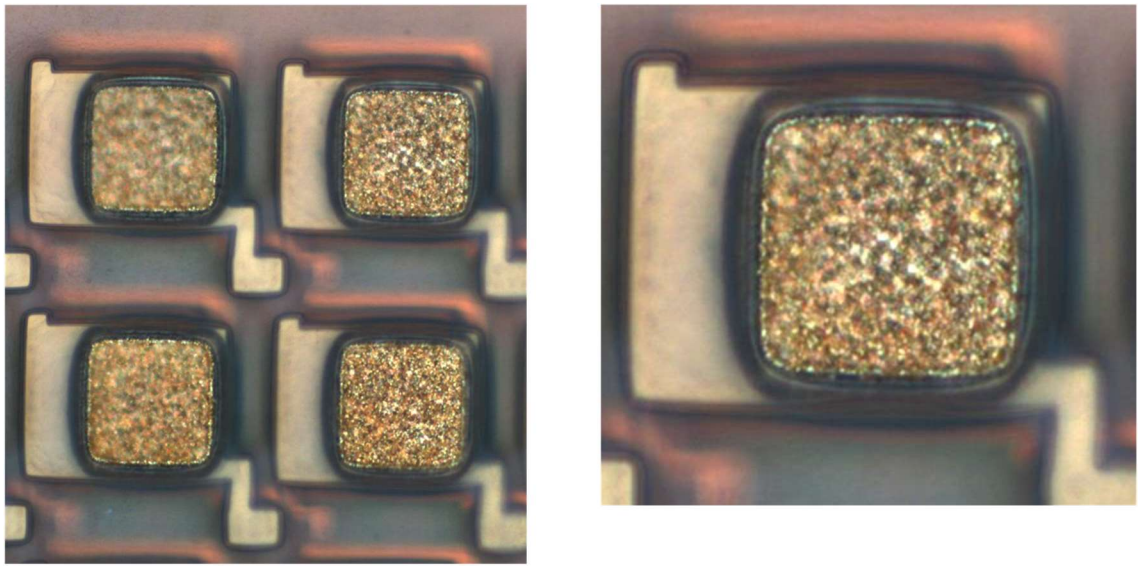

Fig. 3.8. (e) Bright-field microscope image of the electrodes immersed in the autocatalytic gold solution for 1 minute after immersion gold process.

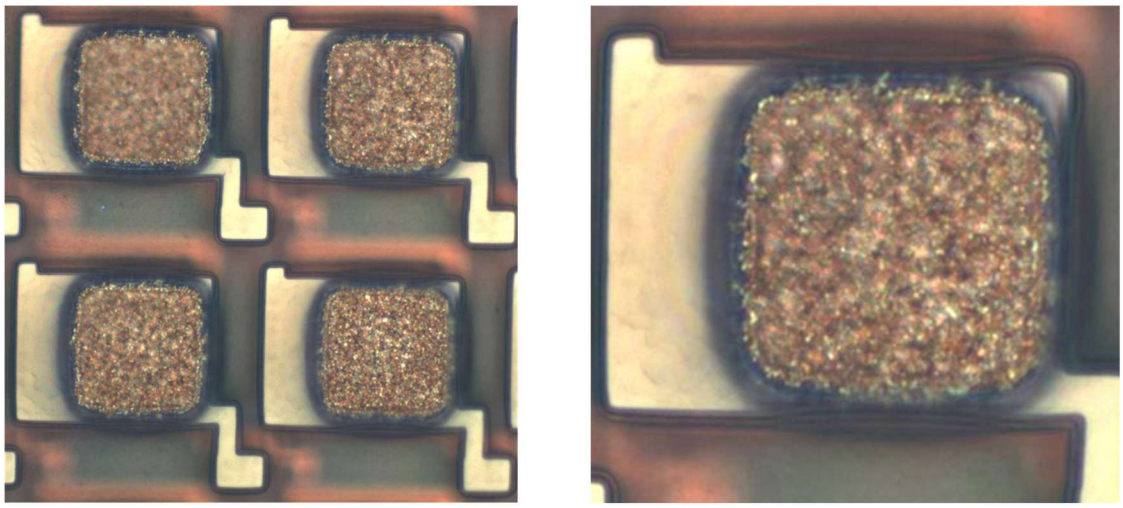

Fig. 3.8. (f) Bright-field microscope image of the electrodes immersed in the autocatalytic gold solution for 3 minutes after immersion gold process.

Figure 3.8. (a) shows the dark field microscope image of the electrodes right after the immersion gold process. The aluminum electrodes are fully covered by the gold layer but the gold layer thickness is below 300 nm. Note that the edge areas are particularly susceptible to culture medium attacks as the immersion gold cannot be grown and attached to the side polyimide passivation layers. Figure 3.8. (b), Figure 3.8. (c), and Figure 3.8. (d) show the dark-field microscope images of the electrodes after it is immersed in the autocatalytic gold solution for 1 minute, 2 minutes, 3 minutes, respectively. Figures clearly show that the gold layer thickness is increased and the gold around the edge area of the electrodes is enhanced and fully covers the electrode. Figure 3.8. (e) and Figure 3.8. (f) show bright field microscope images of the electrodes after it is immersed in the autocatalytic solution for 1 minute and 3 minutes, respectively. Figure 3.8. (f) clearly shows the enhanced gold layer on the electrodes. However, we cannot immerse the sensor chips

longer than 5 minutes. This is because the gold layer attachment to the previous composite layer of aluminum/zinc/nickel is weakened due to the excessive volume of gold layer.

Next, we immerse the gold-plated chip attached to glass substrate in the Dulbecco's Phosphate Buffered Saline (DPBS) solution for more than 3 weeks and we do not observe any chemical residues or bubbles on the gold electrodes.

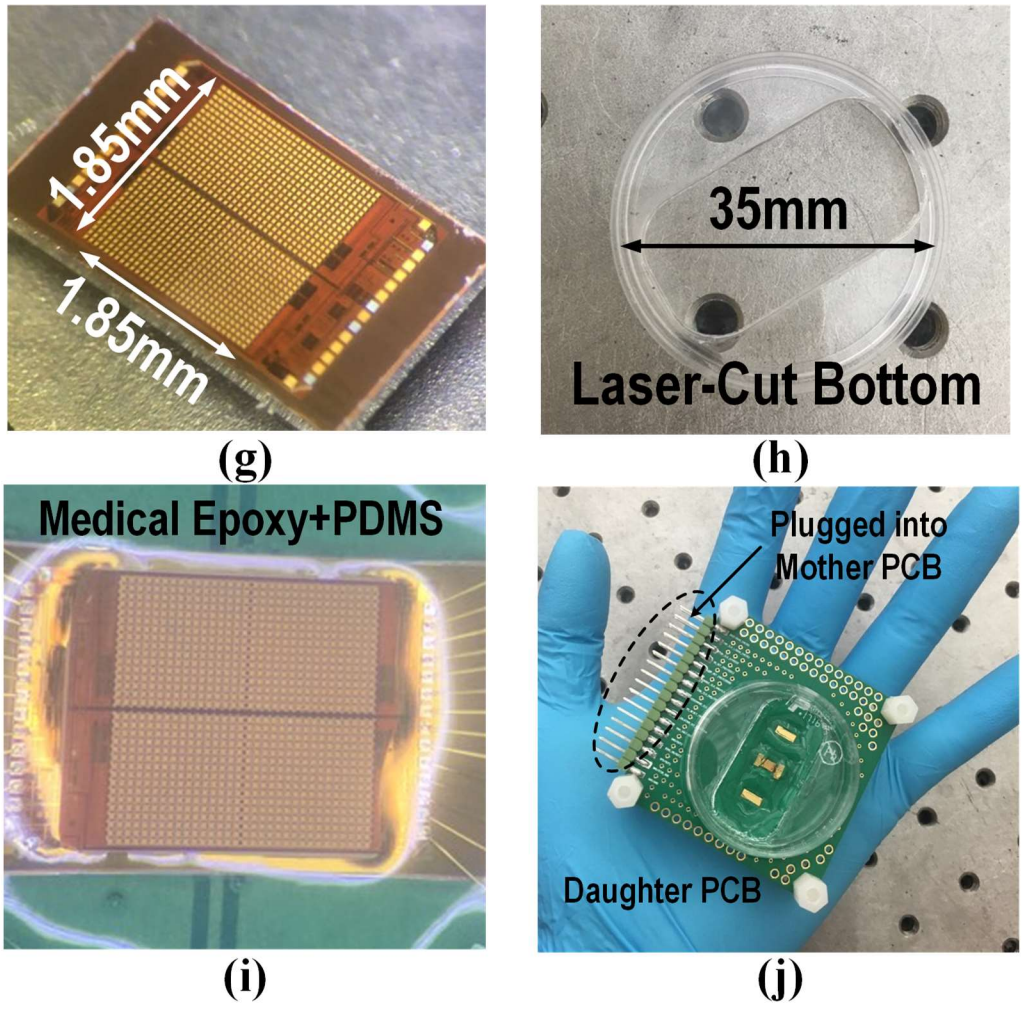

Fig. 3.8. (g) A multimodality cellular interfacing array with gold-plated electrodes, (h) a standard 35mm cell-culture plate with a laser cut bottom, (i) a biocompatible and robust packaging with a medical epoxy and PDMS, and (j) a fully packaged sensor module.

3.4. Electrical Measurements

In this section, we will show the electrical measurement results of the proposed 1024-pixel CMOS multimodality cellular interfacing array. The chip is fully packaged in the daughter PCB and plugged into the mother PCB. The FPGA (USB-1616HS, Measurement Computing Corp.) is used to program the CMOS chip through on-chip SPI and readout the chip outputs. D-type batteries are used for power supply to remove 60Hz noise, and the electrical measurements are performed in a fully shielded chamber.

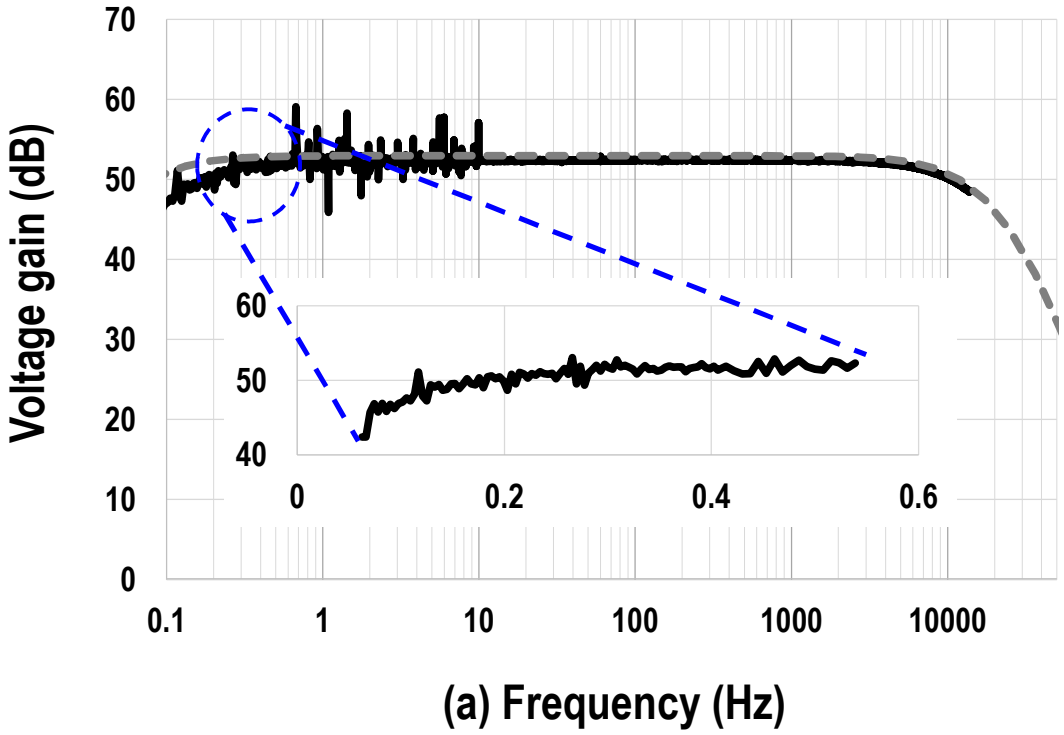

Fig. 3.9. (a) Measured total voltage gain.

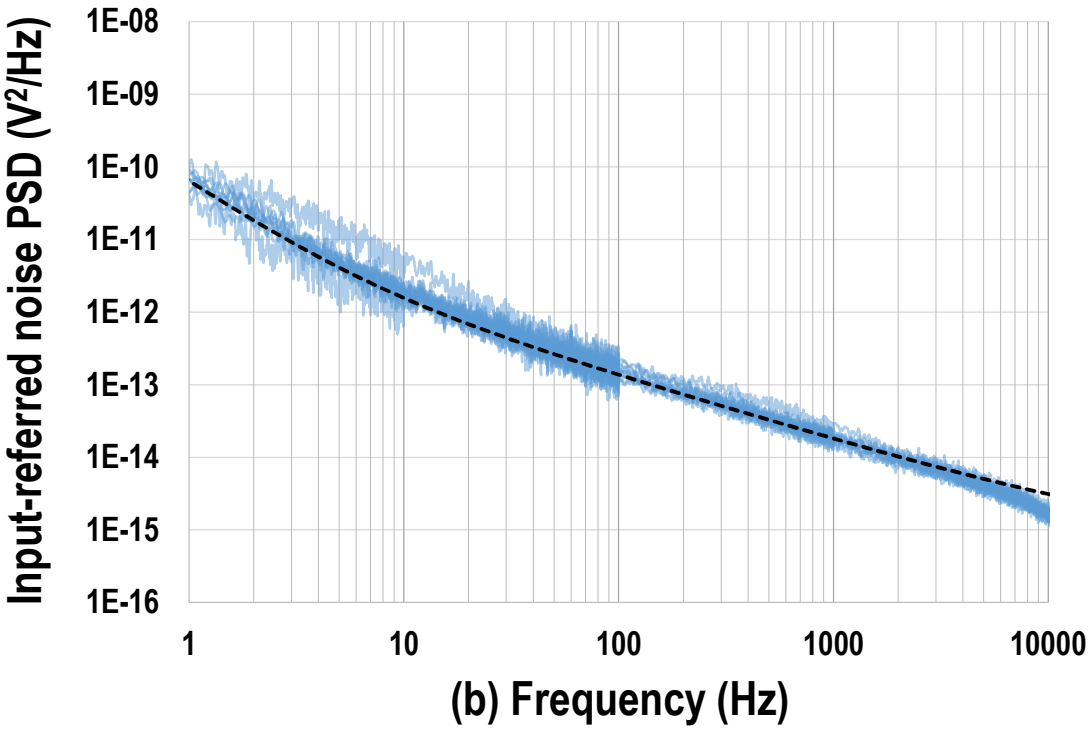

Fig. 3.9. (b) measured input-referred noise PSD for extracellular potential recording modality.

For the extracellular potential recoding mode, the voltage gain, common-mode rejection ratio (CMRR), and input-referred noise power spectral density (PSD) are measured using the dynamic signal analyzer (Keysight 35670A) with the tail current of 37.5μA to evaluate the extracellular potential recording functionality (Fig. 3.9 and Fig. 3.10). The measured average total voltage gain is 52.39dB with a standard deviation σ of 0.03dB, measured average CMRR is 67.2dB with σ of 3.94dB, and the measured low cut-off frequency is 0.1Hz. The measured average input-referred noise is 11.7μV_{rms} integrated from 1Hz to 300Hz (local field potential band) with σ=0.64μV_{rms} and 7.08μV_{rms} integrated from 300Hz to 6kHz (action potential band) with σ=0.36μV_{rms}. In general, to faithfully

capture cardiomyocytes action potentials, an analog bandwidth up-to 2kHz is required. The measured average input-referred noise is $13\mu V_{rms}$ integrated from 1Hz to 2000Hz with $\sigma=0.54\mu V_{rms}$ for cardiomyocytes recording.

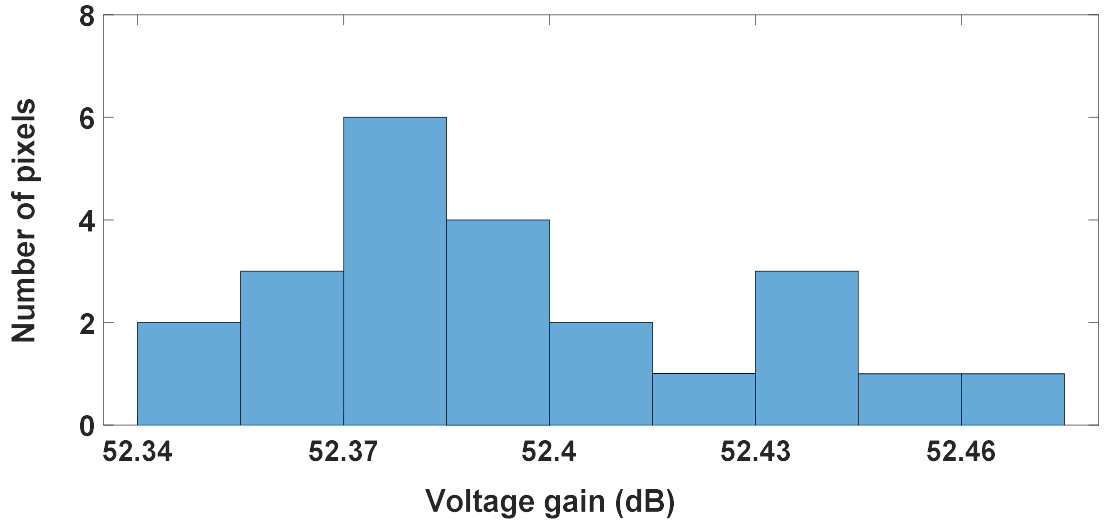

(a)

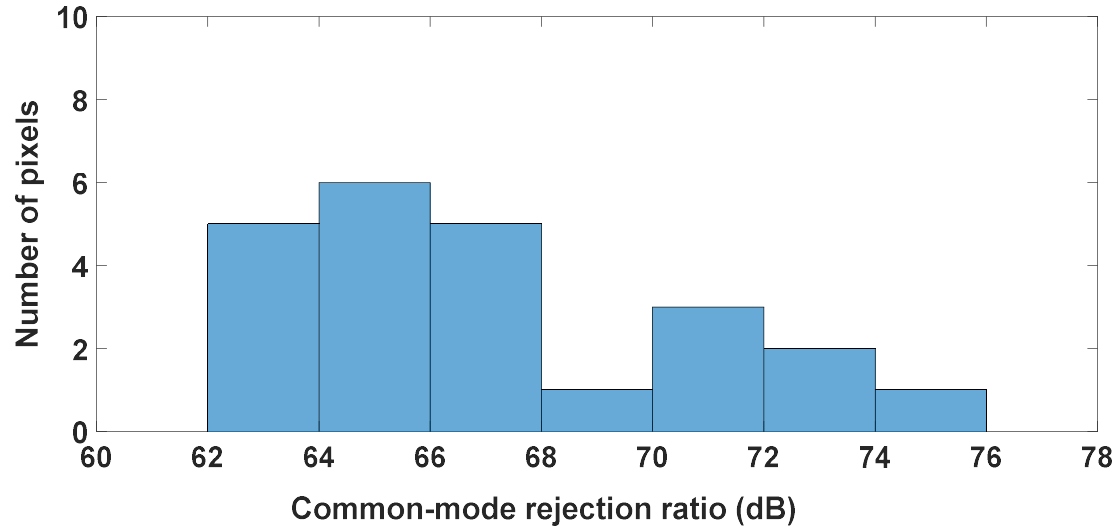

(b)

Fig. 3.10. (a) Measured total voltage gain and (b) common-mode rejection ratio (CMRR) histogram.

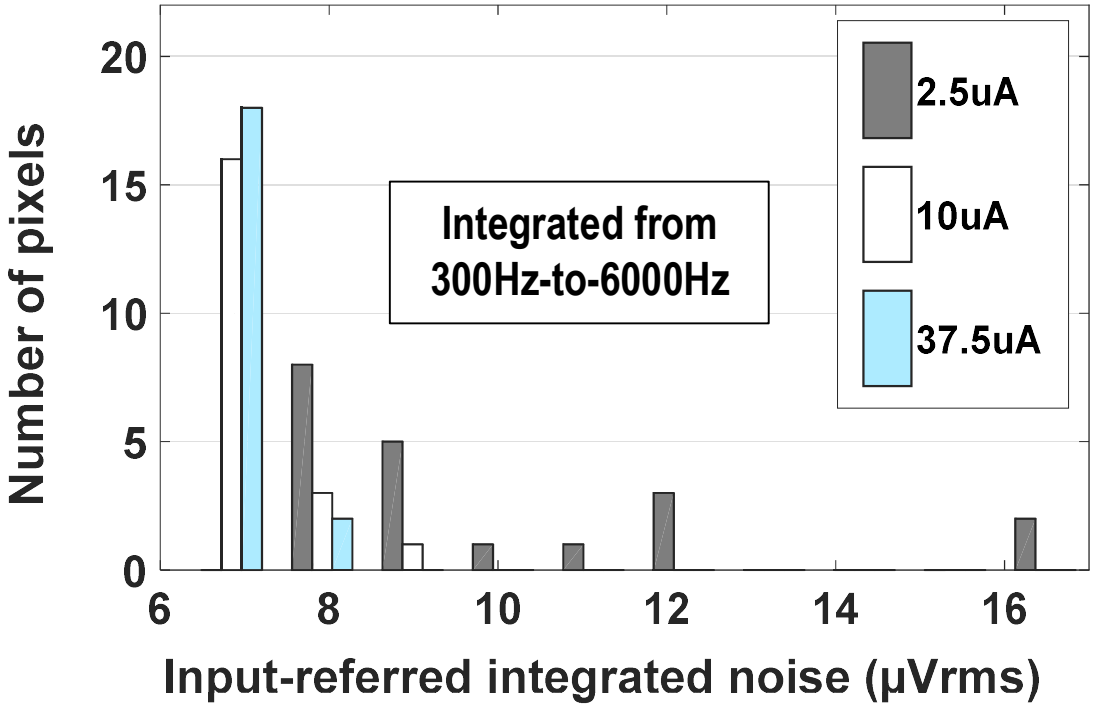

Fig. 3.11. Measured input-referred integrated voltage noise histogram versus different biasing tail current values.

The integrated input-referred voltage noise is also measured on multiple pixels with different tail current strength of fully differential amplifier in Figure 3.4. Figure 3.11 shows the histogram of the measured input-referred voltage noise integrated from 300Hz to 6kHz (action potential band) on 20 pixels with different tail currents. The total voltage gains with the tail current of 2.5μA, 10μA, and 37.5μA are 45.3dB, 50.1dB, and 52.3dB, respectively. The histogram shows that the integrated input-referred voltage noise variations decrease for larger tail currents. For example, the measured average input-referred integrated noises from 300Hz to 6kHz with the tail current of 2.5μA, 10μA, and 37.5μA are 9.94μV_{rms}, 6.99μV_{rms}, and 7.08μV_{rms} with σ=2.72μV_{rms}, σ=0.64μV_{rms}, and σ=0.36μV_{rms}, respectively.

This is because the increased tail current of the differential amplifier (Figure 3.4) increases the override voltages of sensing pixel and reference pixel transistors T_S and T_R, and therefore, the differential amplifier is less sensitive to mismatches. For the following cell-based measurements, we use the tail current of 37.5μA.

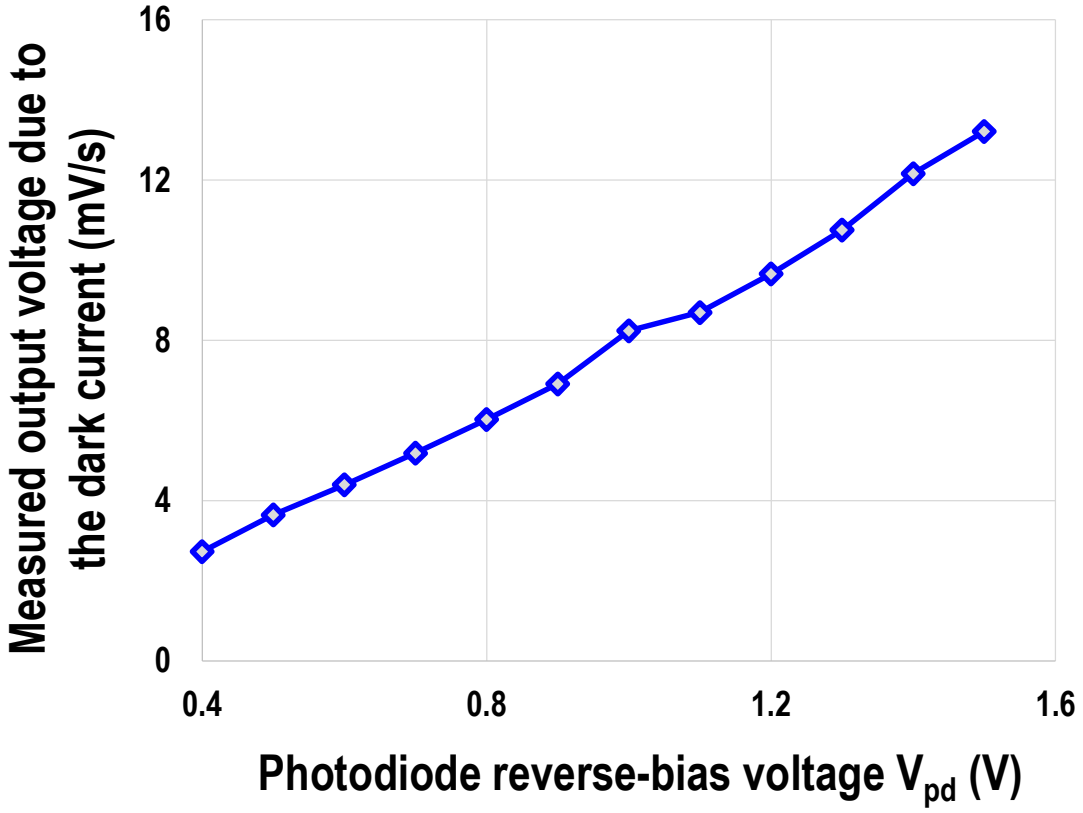

Fig. 3.12. Measured photodiode noise (dark current) versus photodiode reverse-bias voltage VPD.

Next, for the cellular optical detection mode, photodiode noise (dark current) with respect to the photodiode reverse-bias voltage V_{PD} is characterized and shown in Figure 3.12. We employ the correlated-double-sampling (CDS) scheme to remove the reset noise, offset, fixed pattern noise (FPN), and flicker noise [15] [88] using the FPGA. For

photodiode noise characterization, we enable the optical detection modality in the dark room and therefore, the output voltage slope is due to the photodiode dark current integration. Figure 3.12 shows the measured output voltage slope decreases as the photodiode reverse-bias voltage V_{pd} decreases. However, since the input-referred voltage dynamic range for the photocurrent integration is from V_{pd} to 0 (Figure 3.3), the voltage dynamic range decreases as V_{pd} decreases. Considering the trade-off between the linearity and photodiode dark current, we choose V_{pd} of 0.8V for the following cell-based measurements.

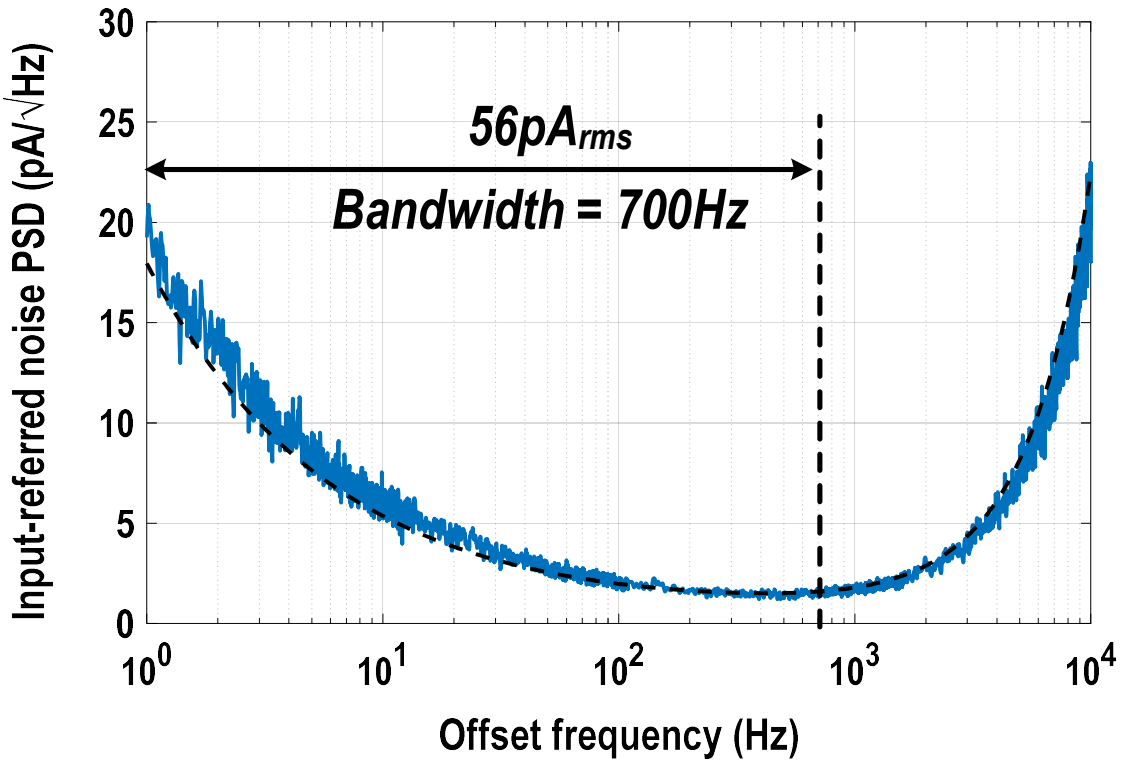

Fig. 3.13. Measured and simulated total output voltage noise power spectral density (PSD) divided by total trans-impedance gain A_{Total} with the mixer frequency of 100kHz.

For the cellular impedance mapping mode, Figure 3.13 shows the measured and simulated total output voltage noise power spectral density (PSD) divided by total trans-impedance gain A_{Total} for the entire current sensing chain, including the TIA, mixer, low-pass filter, and programmable gain amplifier (Figure 3.5). The total output voltage noise is measured with TIA input open condition with the mixer LO frequency of 100kHz and the low-pass filter cut-off frequency of 700Hz. The measured total output voltage noise is then divided by the total trans-impedance gain A_{Total}. The measured input-referred current noise integrated over the low-pass filter bandwidth of 700Hz is $56pA_{rms}$, achieving high sensitivity. The low noise current sensing circuit is essential to minimize the amplitude of the voltage excitation signal for electrode safety. Note that the trade-off exists between the measurement speed and the current sensing sensitivity.

The 7-bit biphasic current stimulator is also characterized. Two adjacent pixels are selected with one electrode for current stimulation and the other for reference. Both electrodes are wire-bonded to PCB traces and connected to a load resistor. Figure 3.14 shows the measured transient waveform for biphasic current stimulation with the load resistance of 33kΩ at the pulse frequency of 2Hz with the stimulation current of 10μA and pulse width of 0.2ms. To achieve charge balancing for electrode safety, cathodic current, anodic current, and passive charge balancing (discharge) periods are sequentially applied [89]. The pulse width, frequency, interphase delay, and current strength are fully programmable through the on-chip SPI.

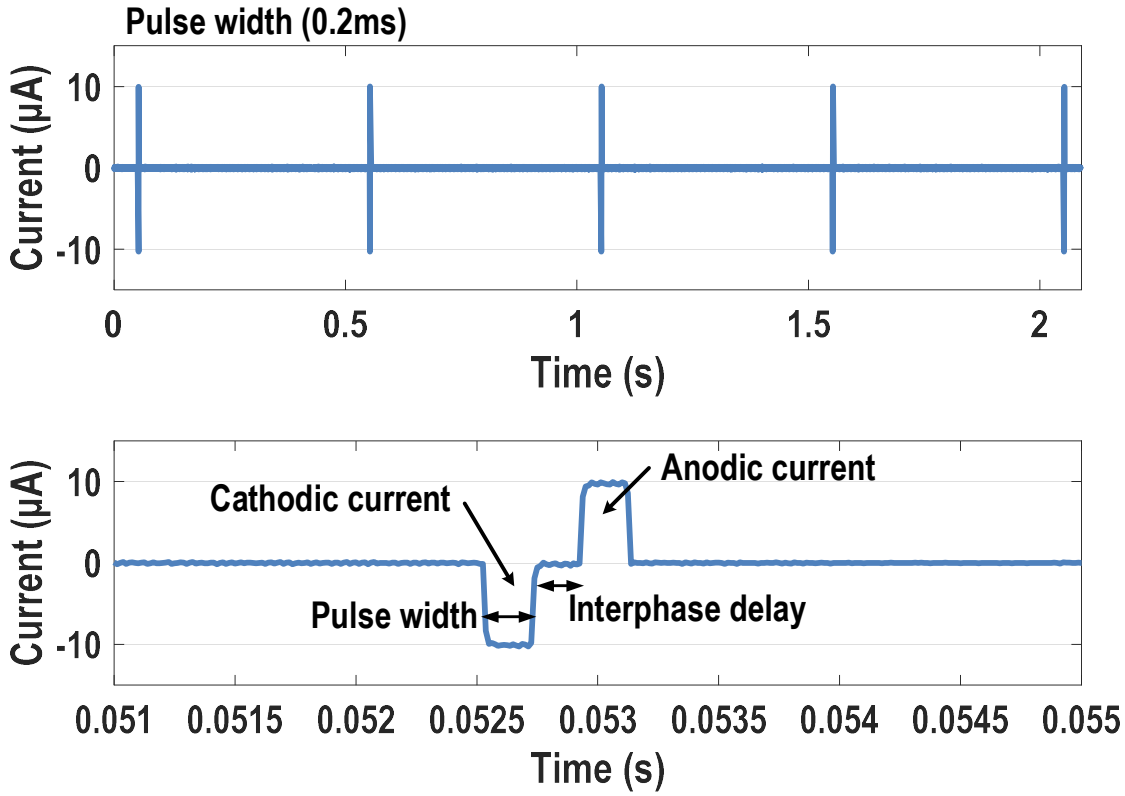

Fig. 3.14. Measured transient waveform for the biphasic current stimulation at the pulse frequency of 2Hz with the pulse width of 0.2ms, the current of 10μA, and the load resistor of 33kΩ.

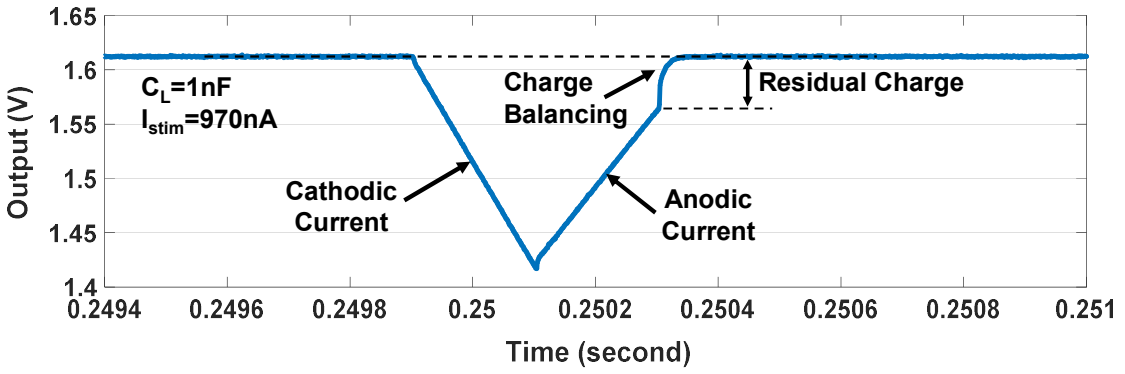

Fig. 3.15. Measured transient waveform for the charge-balanced biphasic current stimulation with the capacitor load of 1nF, the pulse width of 0.2ms, and the current amplitude of 970nA.

Next, two electrodes are connected to a load capacitor of 1nF. Figure 3.15 shows the measured cathodic current integration (negative slope) and anodic current integration (positive slope) on the load capacitor of 1nF with the current amplitude of 970nA, the pulse width of 0.2ms, and without the interphase delay. The measured cathodic current integration slope is 975V/s, which is close to the theoretical slope (970nA/1nF=970V/s). After anodic current pulse, the residual charges mainly due to the cathodic and anodic current strength and pulse width mismatches are properly discharged by the passive charge balancing period (S_{cb}), achieving the charge balancing. The measured differential nonlinearity (DNL) and integral nonlinearity (INL) of the 7-bit current stimulator are within +0.21/-0.36LSB and +0.43/-0.52LSB, respectively, shown in Figure 3.16.

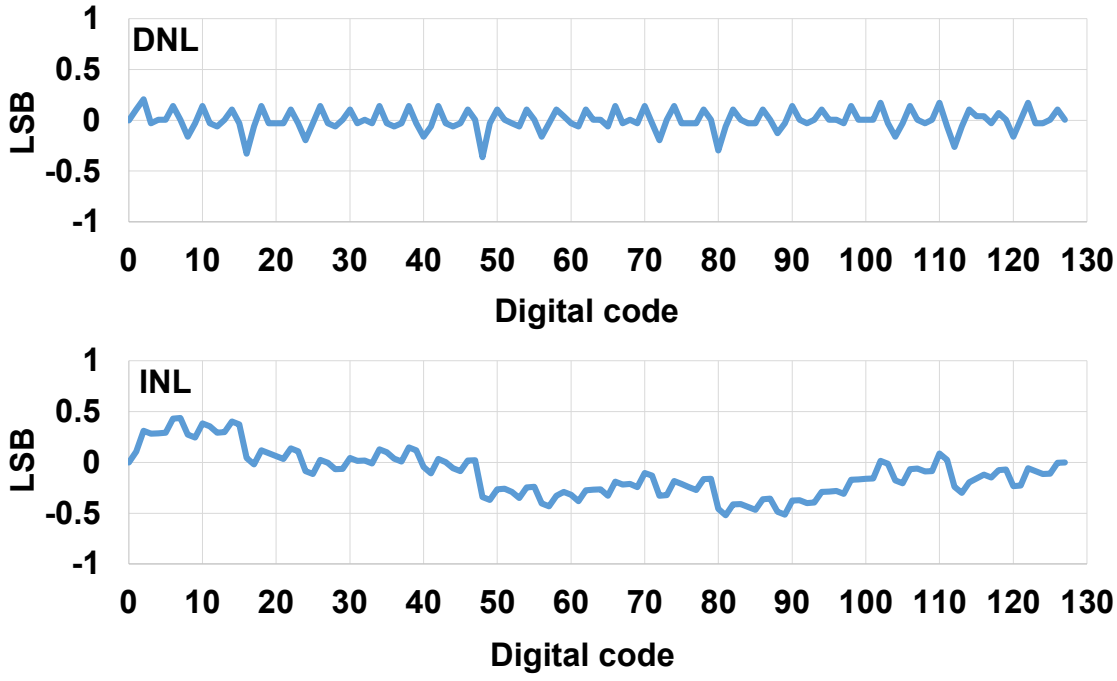

Fig. 3.16. Measured DNL and INL of the 7-bit charge-balanced biphasic current stimulator.

3.5. On-Chip Cultured Cell-Based Experiments

3.5.1. On-Chip Neonatal Rat Ventricular Myocytes (NRVM) Culture

Neonatal rat ventricular myocytes (NRVMs) were isolated from 1- to 2-day old neonatal rat Sprague-Dawley pups (Charles Rivers) as described previously [90] [91]. Three- fourths of the ventricle was excised and treated with trypsin (Worthington Biochemical Corporation, Freehold, NJ) overnight and then enzymatically treated with collagenase (Worthington Biochemical Corporation, Freehold, NJ). Freshly isolated NRVMs were re-suspended in M199 culture medium (Gibco) supplemented with 10% FBS, glucose, 2 mM GlutaMAX, penicillin, vitamin B12, HEPES buffer, and MEM non-essential amino acids (Gibco). Two 60-minute pre-plating steps were performed to reduce fibroblasts and enrich cardiac myocyte content in the culture. NRVMs were transduced with Ad-GFP day of isolation for 2 hours in suspension at room temperature (RT). Media was changed 24 hours after initial transfection. Spheroids were formed using Aggrewell^{TM} (STEMCELL, Vancouver, Canada). The Aggrewell 400^{TM} plate was sterile as provided from the vendor and was opened in a biosafety cabinet. A total of 0.5 mL of Rinsing Solution (STEMCELL, Vancouver, Canada) was added to each well and the plate was centrifuged for 2 min at 2,000g. The plate was then incubated for at least 30 minutes at RT or overnight at 4°C. The plate was washed with PBS prior to use and 0.5 mL of media was added to well and centrifuged for 3 min at 2,000g. Cell solution containing 1.2×106 NRVMs in a 0.5 mL volume was added to each well. Aggrewell plate was centrifuged for 5 min at 200g. Stereo microscope images are used to verify the cell distribution across the well. The plate was incubated overnight, and its media was replaced by removing 0.5 mL

from the plate edge and adding 0.5 mL fresh media. After 3 nights, the spheroids have formed and can be recovered from plate by gently jetting them out with a pipette.

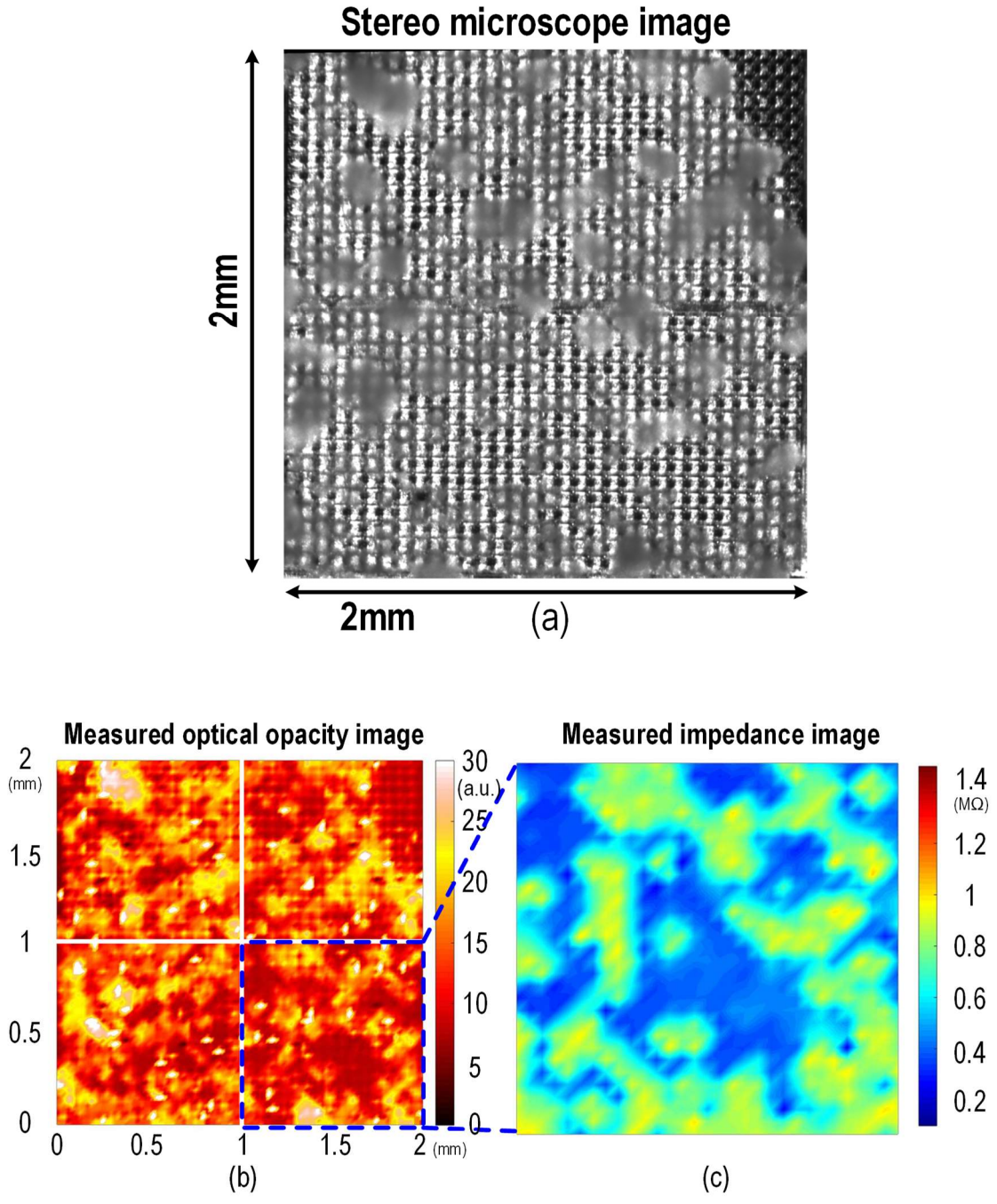

Fig. 3.17. (a) Stereo microscope image, (b) measured optical opacity image, and (c) measured impedance mapping of on-chip cultured rat cardiomyocytes.

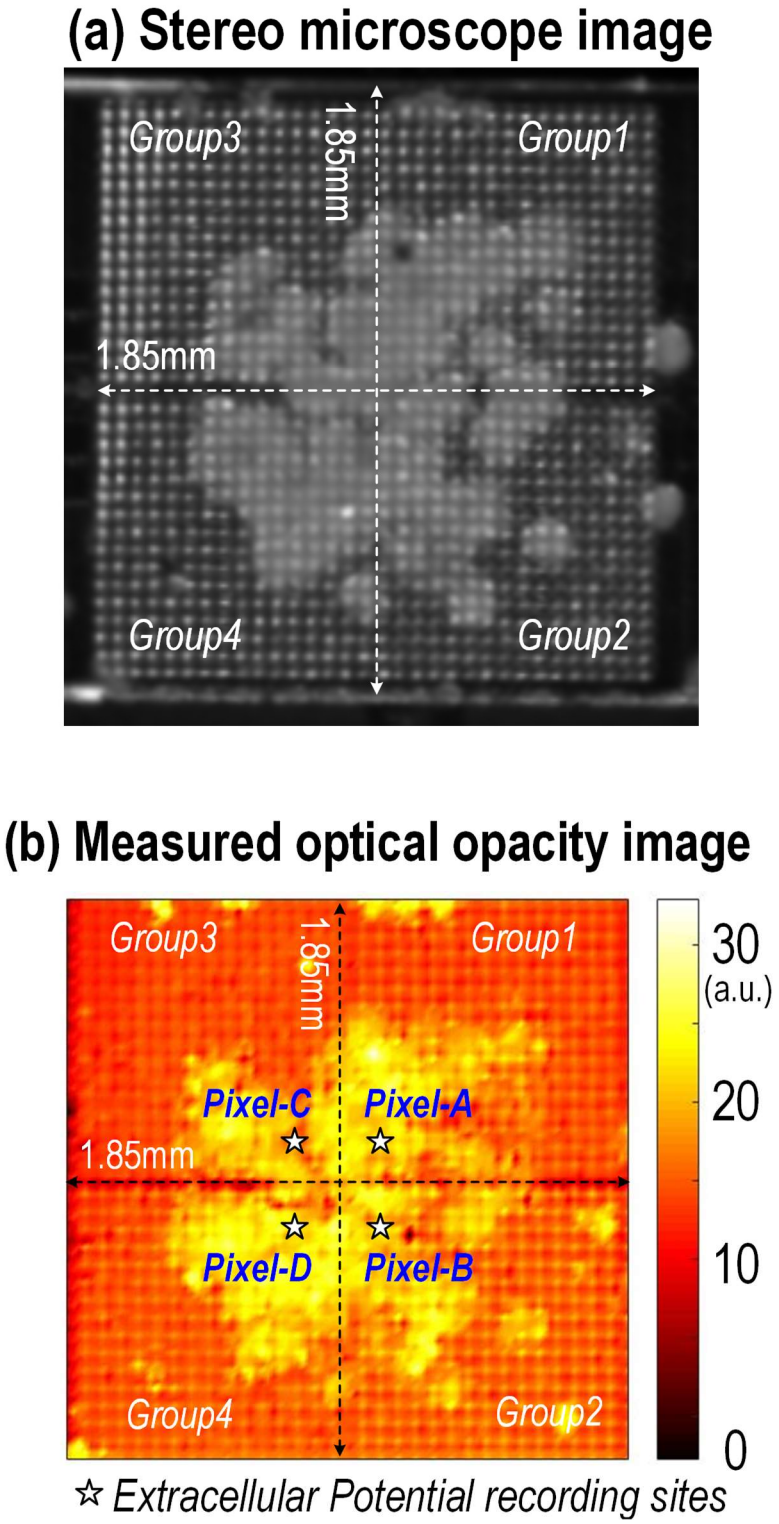

Fig. 3.18. (a) Stereo microscope image and (b) measured optical opacity image of the on-chip cultured synchronous cardiomyocyte cluster.

The CMOS chip surface was washed with DPBS (Gibco) and coated with human fibronectin (Corning, Corning NY) at a concentration of 5 µg/mL for 1 hour at 37°C. Spheroids were added to the CMOS chip surface and allow to adhere overnight. After 24 hours, fresh medium with 10% serum was added. Media is replaced every 2 days (Figure 3.19) [92].

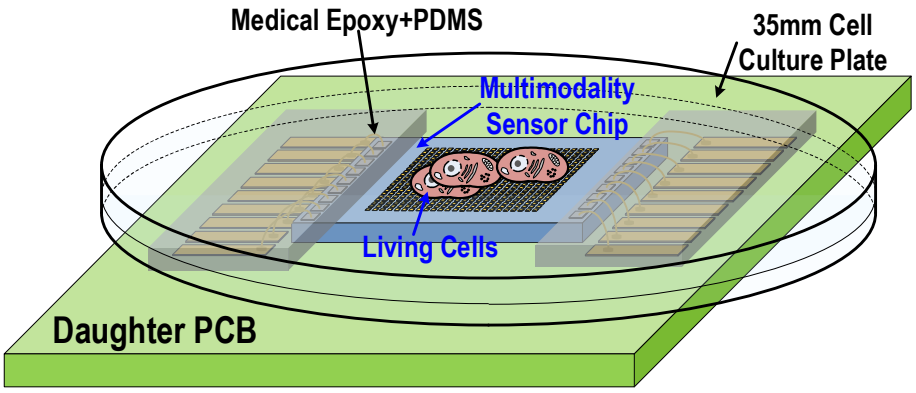

Fig. 3.19. Illustration of in-vitro measurement setup with a fully packaged multimodality cellular interfacing array module.

3.5.2. High Resolution Optical/Impedance Imaging

Figure 3.17 (a) shows the stereo microscope image of the on-chip cultured rat cardiomyocytes. The rat cardiomyocytes are well attached to the CMOS chip surface with successful growth. First of all, the light intensities at 4096 optical detection sites are measured and the measured optical opacity image is shown in Figure 3.17 (b). The measured optical opacity image closely matches the reference stereo microscope image and clearly shows the 2D distribution of the cultured rat cardiomyocytes on the CMOS chip surface. Furthermore, with the high spatial resolution, Figure 3.17 (b) also clearly shows the opacity gradient within the rat cardiomyocytes cluster that can be a useful

indicator for cell viability tests. For example, in Figure 3.17 (b), the measured opacity gradient of the rat cardiomyocyte cluster inside the dotted circle using our CMOS chip closely matches that of the reference stereo microscope image. Therefore, the proposed CMOS chip demonstrates in-situ low cost optical detection, particularly useful for massively paralleled fully automated drug screening applications.

Next, impedance sensing is performed on the right lower corner of the chip at 100kHz in Figure 3.17 (b). With the spatial resolution of 58μm, the proposed sensor can measure the impedance of rat cardiomyocyte spheroid/cluster. The measured rat cardiomyocyte spheroid/cluster impedance image is shown in Figure 3.17 (c) and closely matches the measured optical opacity image in Figure 3.17 (b) and the reference stereo microscope image in Figure 3.17 (a). The impedance image shows not only the 2D distribution of the cultured cell clusters on the chip surface but also the cell cluster-to-sensor surface attachment, which is a critical indicator for successful *in vitro* mammalian cell growth [31]. The cell adhesion is essential to the etiology and pathogenesis of diseases such as inflammatory diseases and oncology [57]. In addition, the cellular impedance is an important cell property parameter that can monitor physiological events such as myocardial ischemia [64] and cardiac muscle contraction [12].

The asynchronous cardiomyocyte spheroids in high concentration are often combined to form a large cardiomyocyte cluster with synchronized beating. Figure 3.18 (a) and (b) show the reference stereo microscope image and the measured optical opacity image of the on-chip cultured synchronous cardiomyocyte cluster. The measured optical opacity image closely matches the reference stereo microscope image, and the synchronized and autonomous beating is observed under stereo microscope.

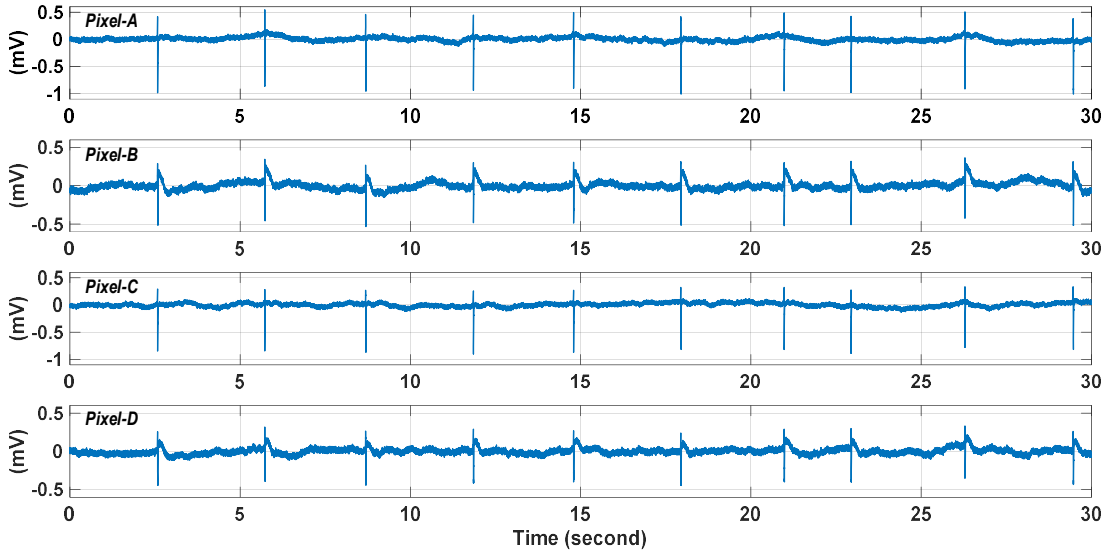

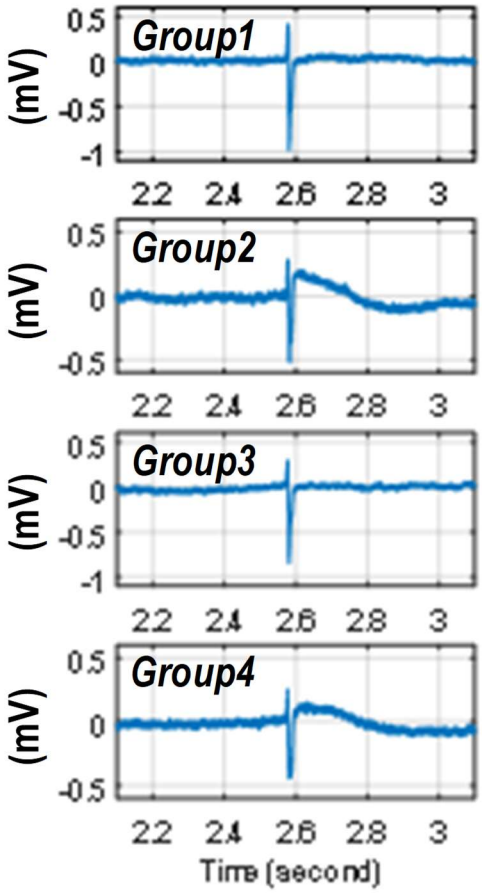

Fig. 3.20. Measured extracellular potentials with on-chip cultured rat cardiomyocytes at 4 different recording sites in Figure 3.18.

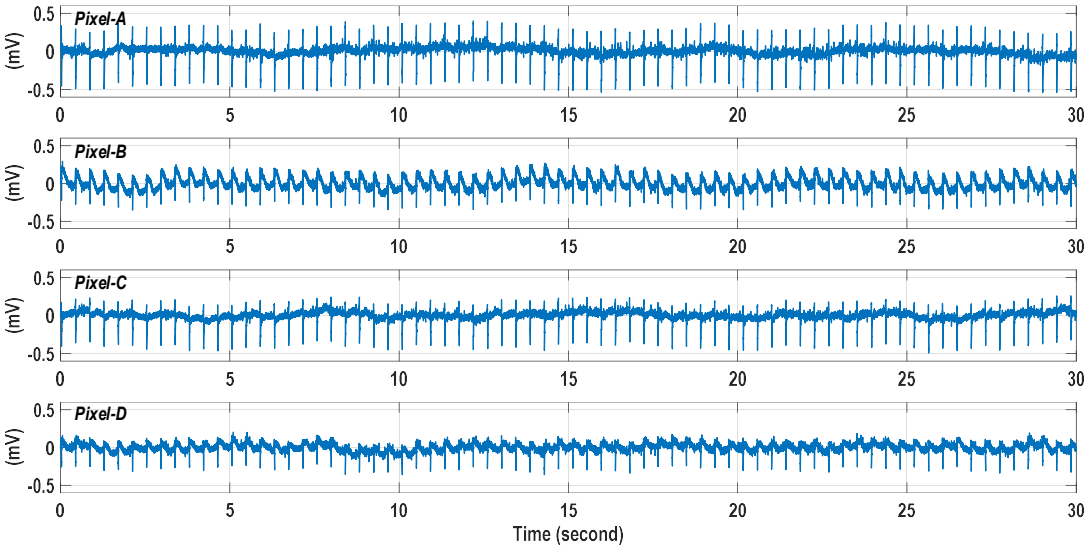

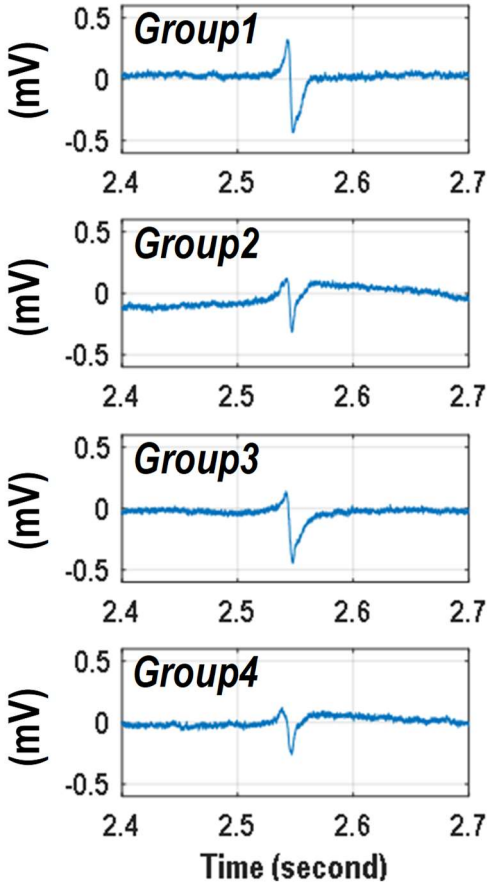

Fig. 3.21. Measured extracellular potential with on-chip cultured rat cardiomyocytes after isoproterenol administration at 4 parallel recording sites in Figure 3.18.

3.5.3. Extracellular Potential Recording

We also performed extracellular potential recordings for the on-chip cultured rat cardiomyocyte cluster shown in Figure 3.18. Figure 3.20 shows the measured input-referred extracellular potentials at 4 independent recording sites labeled in Figure 3.18 (b). The measured extracellular potential recordings achieve high signal-to-noise ratio (SNR) and faithfully capture the fast action potential spikes and slow local field potentials shown in Figure 3.20. The measured extracellular potentials at Pixel-A and Pixel-C mostly show fast action potential spikes. On the other hand, the measured extracellular potentials at Pixel-B and Pixel-D clearly show fast action potential spikes together with slow local field potentials. No external filter or signal post-processing is used. The measured action potential spikes at 4 parallel sites are well synchronized, indicating that cardiomyocytes are electrochemically connected. The measured beating rate is 0.34Hz with a standard deviation of 0.063Hz.

In addition, we directly add 10μL isoproterenol to the culture medium to test the cell-based drug detection capability of the CMOS multimodality chip. The isoproterenol is a medication used for the treatment of bradycardia, heart block, and asthma [49]. The measured parallel extracellular potentials are shown in Figure 3.21 after the isoproterenol administration. After isoproterenol administration, the cardiomyocytes beating rate increases to 2.38Hz from 0.34Hz, and the cardiomyocytes beat more uniformly with a measured standard deviation of 0.007Hz. Also, the measured action potential spikes at 4 parallel recording sites are well synchronized. Furthermore, the measured input-referred action potential spike amplitude decreases with isoproterenol. The observed cardiomyocytes responses well match the isoproterenol drug effects.

3.5.4. Optical Measurements of Cardiac Muscle Contraction and Relaxation

The light transmittance of cardiomyocytes varies with the mechanical movements due to cardiac muscle contraction and relaxation [27]. We measure the real-time light transmittance changes of on-chip cultured rat cardiomyocytes using our CMOS multi-modality chip, which can optically extract the cardiac beating information. For the measurement, we put the CMOS chip module with on-chip cultured rat cardiomyocytes (Figure 3.18) in the dark room and illuminate off-the-shelf LED light from the top. Since the incident light intensity is constant, the measured transient light intensity at the optical sensing sites on the CMOS chip shows the transient light transmittance of cardiomyocytes. Note that we perform the measurement using the same cellular sample in Figure 3.18, and therefore the optically measured cardiomyocytes beating rate can be directly compared with the measured cardiomyocytes beating rate by extracellular potential recordings (Figure 3.21).

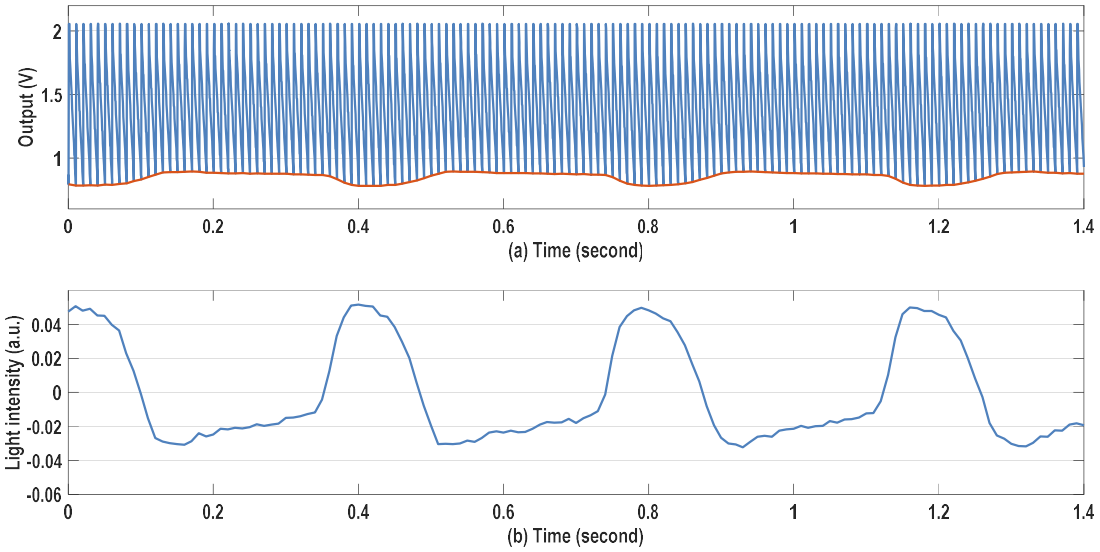

Fig. 3.22. Measured transient (a) chip output voltage slope for optical detection and transient (b) light intensity.

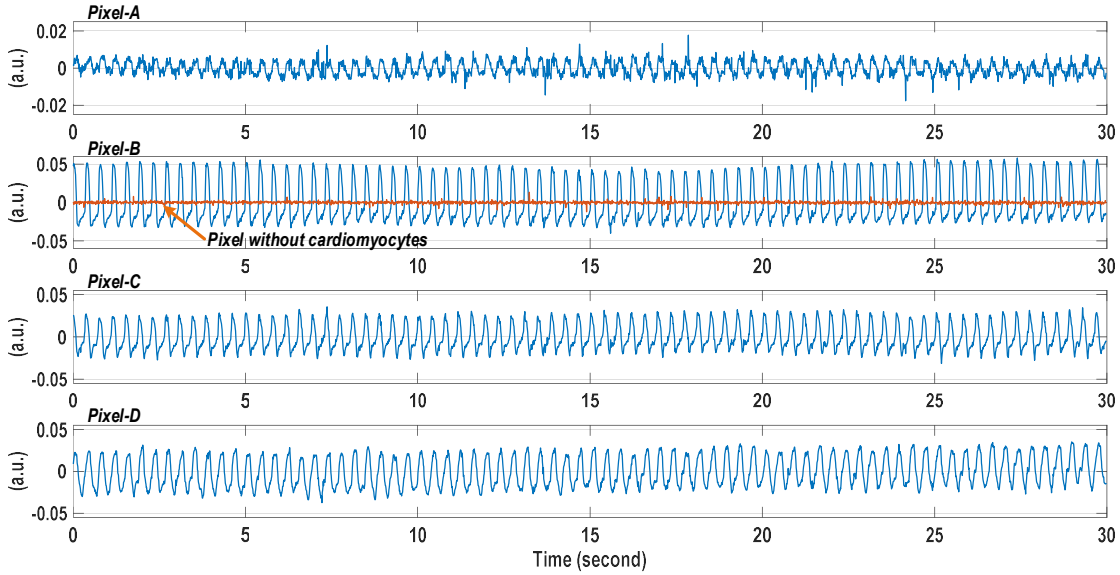

Fig. 3.23. Measured transient light intensities at 4 parallel recording sites in Figure 3.18. A pixel without cardiomyocytes is also recorded as the control experiment.

Figure 3.22 (a) shows the real-time CMOS chip output voltage for the optical detection with the photodiode reset frequency of 100Hz, and Figure 3.22 (b) shows the measured transient light intensity extracted using correlated double sampling of the output voltage slope. To faithfully capture the cardiac muscle mechanical movements, we use the optical sampling frequency (photodiode reset frequency) of 100Hz for a temporal resolution of 10ms [27]. The measured transient light intensity in Figure 3.22 (b) clearly shows the cyclic patterns of systolic and diastolic rhythms for on-chip cultured rat cardiomyocytes. Figure 3.23 shows the measured real-time light intensities at 4 parallel recording sites labeled in Figure 3.18, recorded concurrently. The larger light intensity changes are observed at Pixel-B indicating stronger cardiac muscle contraction around that pixel compared to the other pixels. The real-time light intensities also show that the cardiac muscle contractions are well synchronized, which is consistent with the measured

extracellular potential recording (Figure 3.21). The optically measured cardiomyocytes beating rate is 2.59Hz with the standard deviation of 0.08Hz, closely aligned with the extracellular potential recording results. The real-time light intensity at a pixel without cardiomyocytes is also measured as a control experiment and plotted together with the real-time light intensity at Pixel-B in Figure 3.23, showing high SNR and confidence level of the cardiomyocytes light intensity measurements. Although we do not enable two sensing modalities simultaneously for each pixel, with fully integrated on-chip high-speed electronics, the multiple sensing modalities are multiplexed with sufficiently small time interval to achieve multi-modal sensing on the same on-chip cellular samples with biological relevance.

3.5.5. Biphasic Current Stimulation for Cardiomyocyte Pacing

The cell pacing experiments with the on-chip cultured rat cardiomyocytes are also performed. The fluorescent-microscope image, measured optical opacity image, and measured impedance image of the on-chip cultured rat cardiomyocytes are shown in Figure 3.24 (a), Figure 3.24 (b), and Figure 3.24 (c), respectively. The rat cardiomyocyte spheroids achieve full confluency and very slow synchronized autonomous beating is observed (1 beat/min). For cell pacing experiments, the rat cardiomyocyte spheroids are first stimulated at 4 independent sites (Figure 3.24) with the pulse frequency of 1Hz, the pulse width of 200μs, and the current amplitude of 33μA. Then, we gradually increase the pulse width from 200μs to 4ms to measure the pacing threshold while keeping the pulse frequency and the current amplitude same. At the same time, the extracellular potential recordings are enabled at 4 independent sites (Figure 3.24) to monitor the stimulation response of the on-chip cultured rat cardiomyocytes. Note that since the stimulation artifact could saturate the

potential recording amplifier, simultaneous stimulation and potential recording on the same location are challenging [93] [94]. Therefore, the extracellular potential recordings are enabled on the recording sites which are 656μm apart from the biphasic current stimulation sites (Figure 3.24) to allow response time delay.

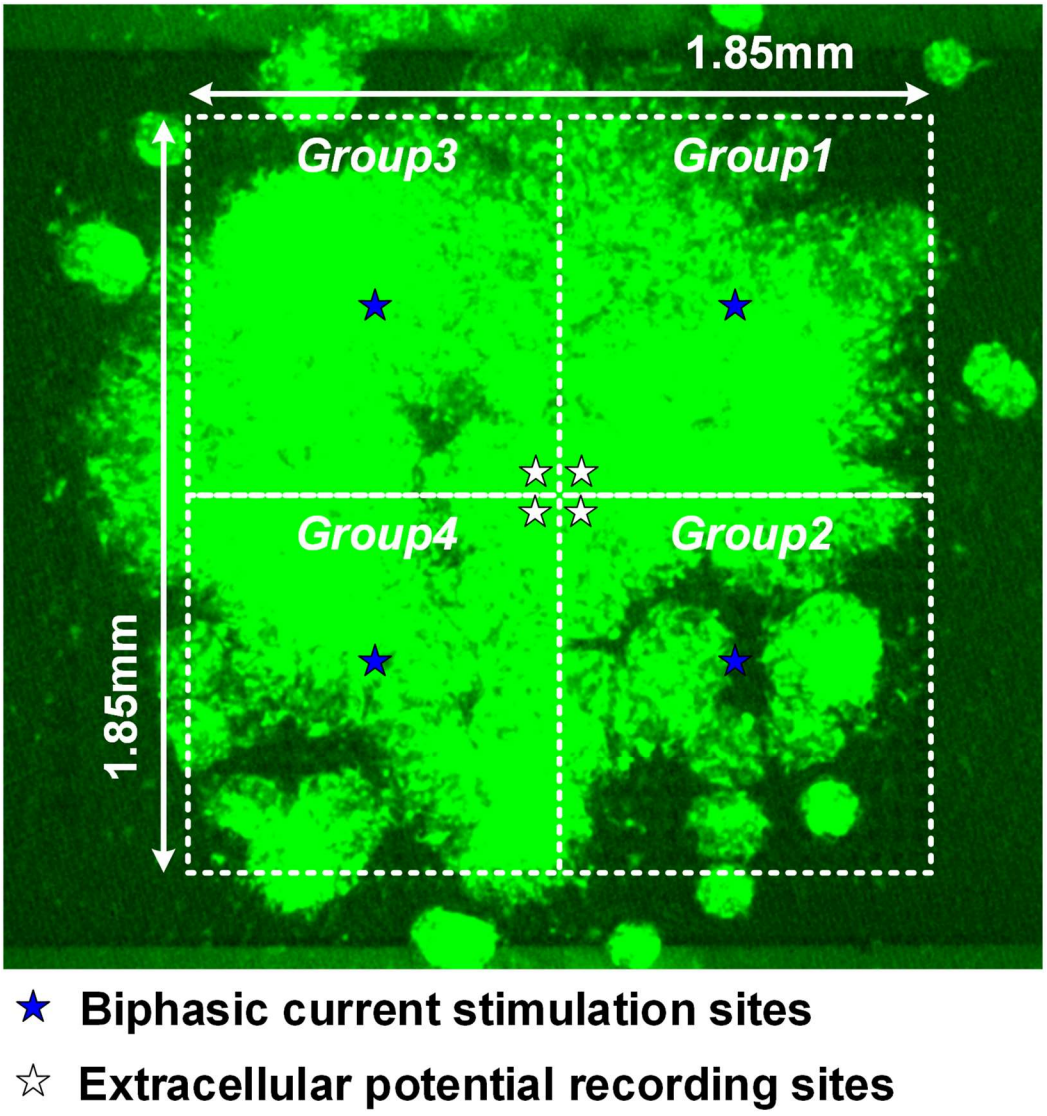

Fig. 3.24. (a) The fluorescent-microscope image of the on-chip cultured rat cardiomyocytes.

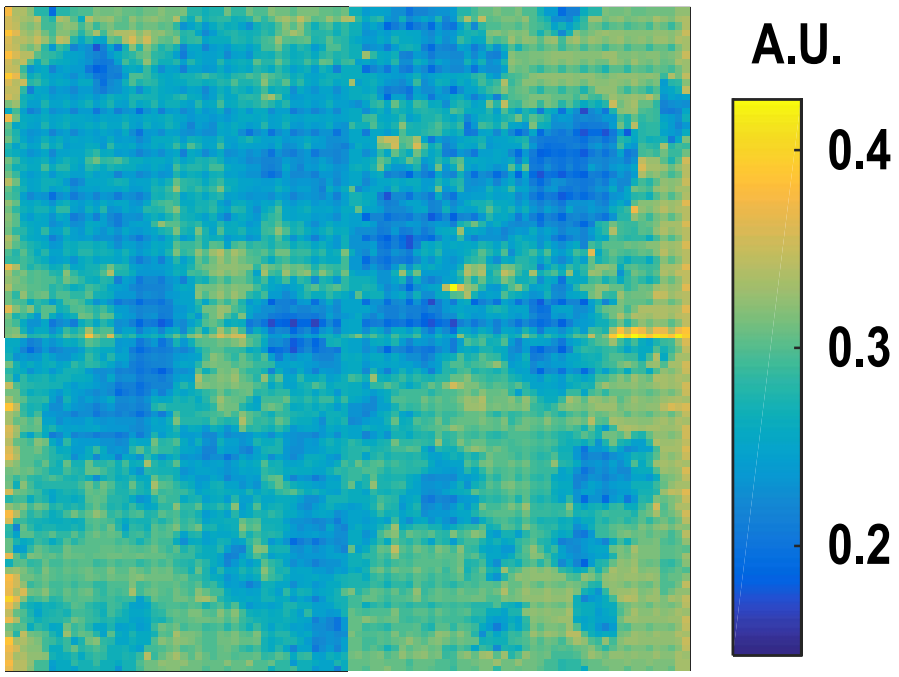

Fig. 3.24. (b) The measured optical opacity image of the on-chip cultured rat cardiomyocytes shown in Fig. 3.24. (a).

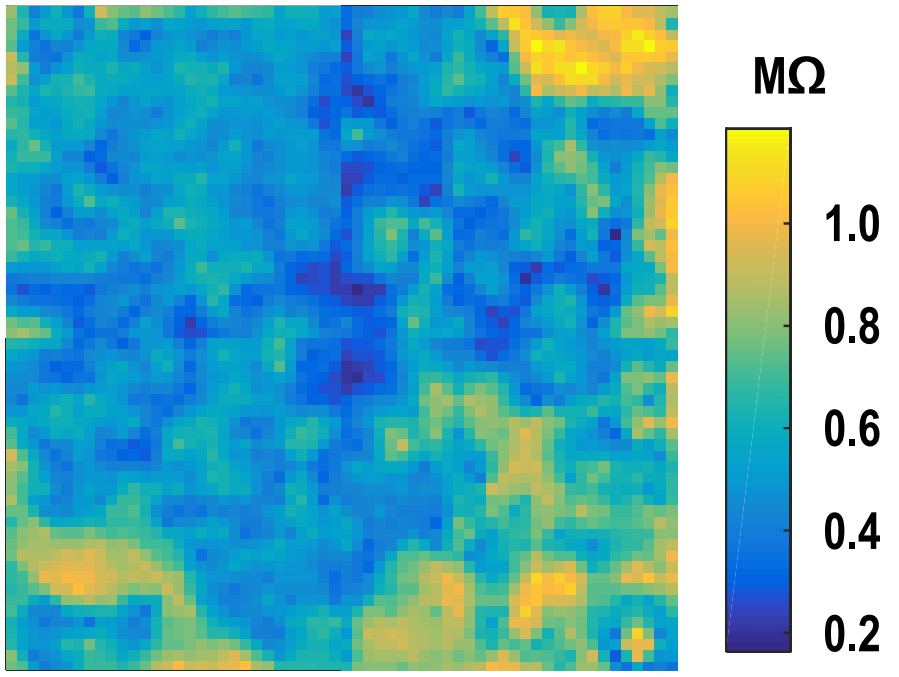

Fig. 3.24. (c) The measured impedance image of the on-chip cultured rat cardiomyocytes shown in Fig. 3.24. (a).

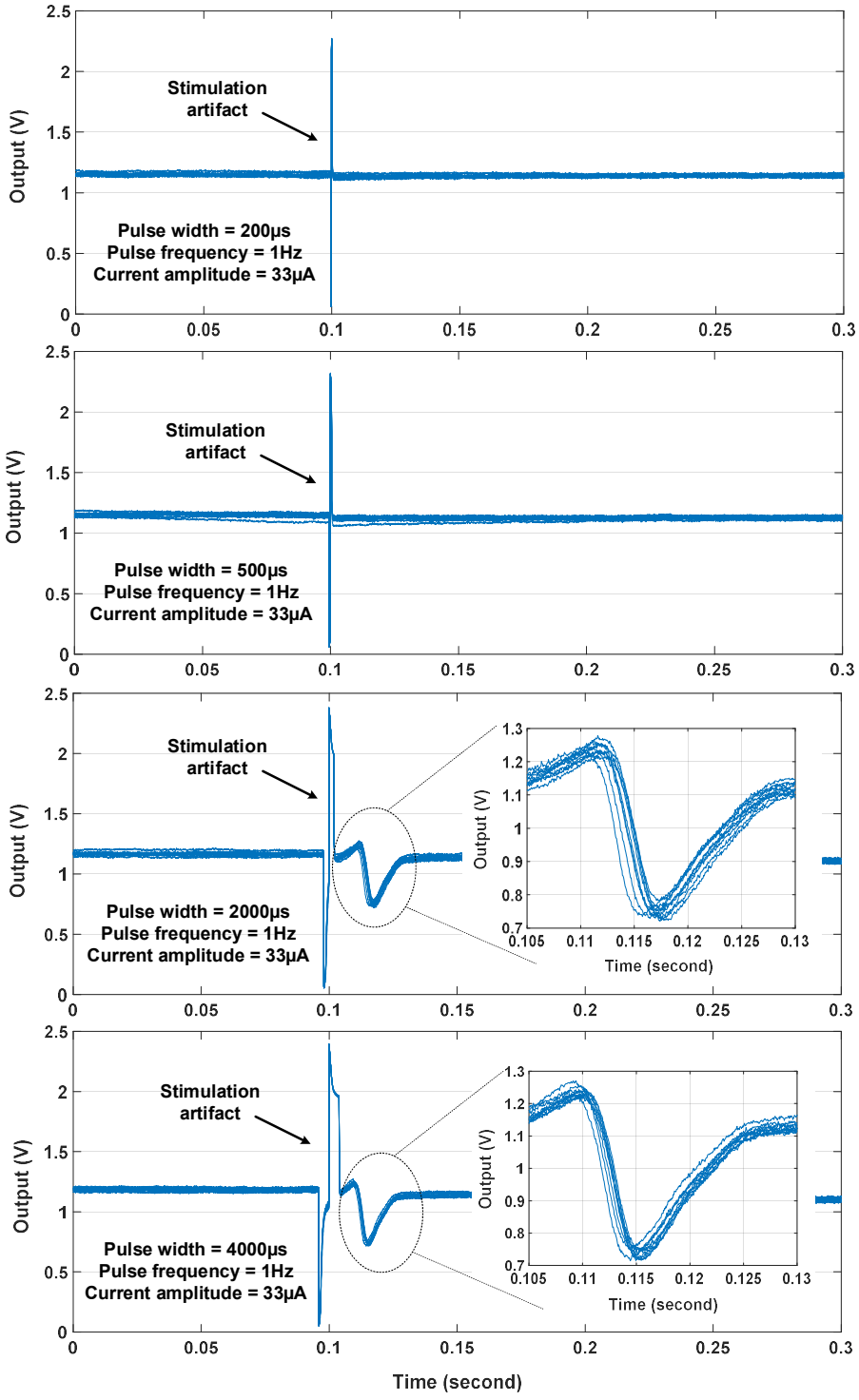

Fig. 3.25. The overlay plot of the measured extracellular potential recordings at the pixel group1 with the on-chip biphasic current stimulation versus different biphasic current stimulation pulse width.

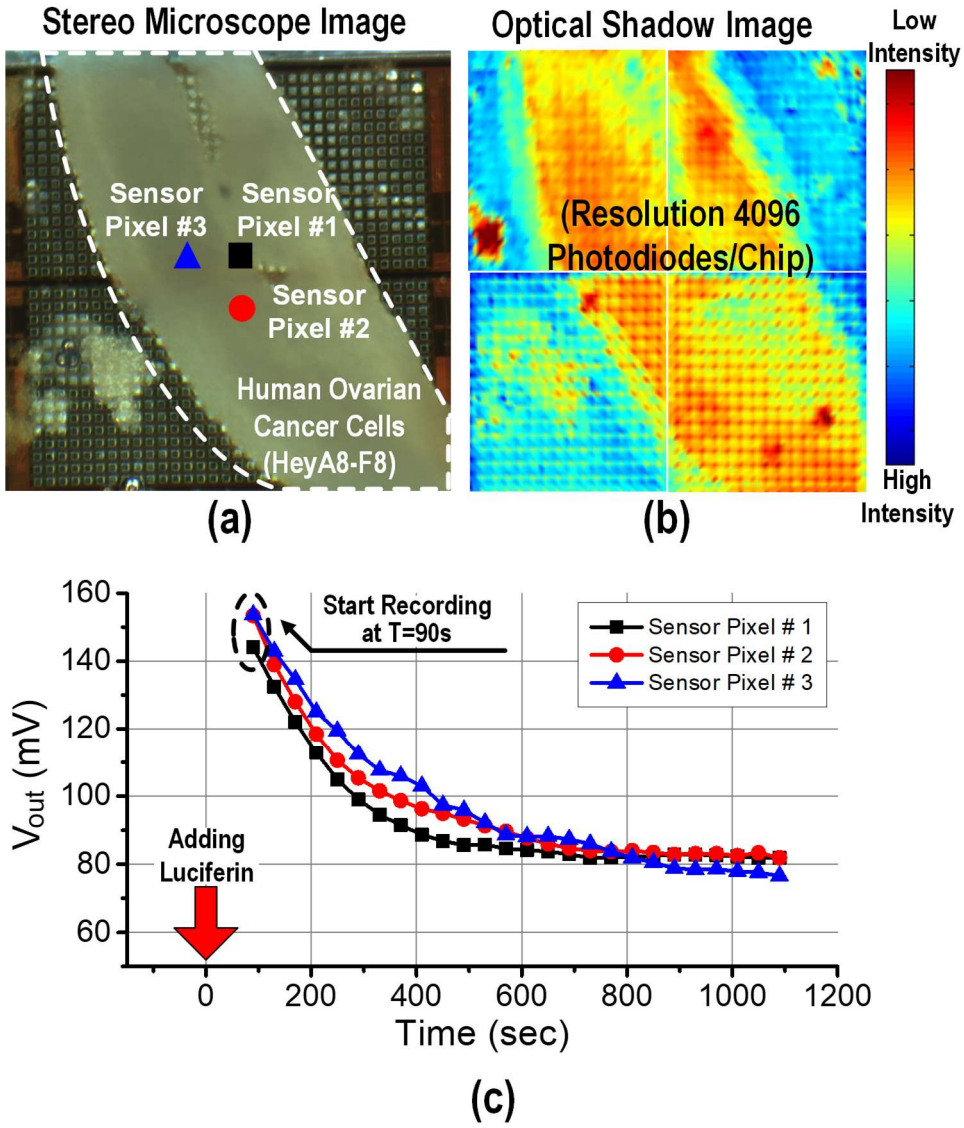

Fig. 3.26. (a) The reference image of the on-chip cultured HeyA8-F8 cells. (b) Measured optical shadow image by the CMOS chip. (c) The real-time bioluminescence measurement results for 3 pixels.

The overlay plot of the measured extracellular potentials at the pixel group1 (Figure 3.24) with the biphasic current stimulations is shown in Figure 3.25. The measurement results show that the on-chip cultured rat cardiomyocyte spheroids are successfully paced with the pulse width greater than 2ms and the measured capture rate is 100% with the pulse

width greater than 2ms. The output referred evoked action potential spike amplitude is 538mV, which is corresponding to the input referred voltage amplitude of 1.34mV. It also shows that the time delay between the current stimulations and evoked action potential spikes, the amplitude of the spikes, and the shape of the spikes are consistent for 10 continuous biphasic current stimulations.

The human ovarian cancer cells (HeyA8-F8) are also cultured on the chip shown in Figure 3.26. First of all, the 4096 optical sensing sites are scanned and the measured optical opacity image is shown in Figure 3.26. (b). The measured optical opacity image closely matches the reference stereo microscope image (Figure 3.26. (a)), showing location, 2D distribution, and opacity information of the on-chip cultured human ovarian cancer cells. Then, we add luciferin to trigger cellular bioluminescence responses. Real-time recordings at 3 pixels show desired bioluminescence decaying response (Figure 3.26. (c)).

	Modality	Pixel Size (μm^2)	Number of Pixels	Field of View (mm^2)	On-Chip Cell Assay	Measured Cellular Phenotype	Tech (nm)
This work	**Potential Recording, Impedance Sensing, Optical Detection, Current Stimulation**	**58 × 58**	**1024**	**1.85×1.85**	**Rat CMs**	**Extracellular Potential, Impedance/Optical Imaging, Cardiac Muscle Contraction/Relaxation, Stimulation**	**CMOS 130**
[34]	Magnetic Movement Tracking	180 × 180	64	1.2×1.2	Cardiac Progenitors	Cardiac Muscle Contraction/Relaxation	CMOS 65
[8]	Potential Recording	7.5 × 7.5	16k	1×1	Snail Neurons	Extracellular Potential	CMOS 500
[9]	Potential Recording, Current Stimulation	17.5 × 17.5	26k	3.85×2.1	Rat Cortical Neurons	Extracellular Potential	CMOS 350
[10]	Impedance Sensing	90 × 90	100	1×1	DNA, Protein	DNA Hybridization, Protein Detection	CMOS 350
[65]	PH Sensing	10.2 × 10.2	65k	2.87×2.87	Hexokinase, Glucose	Glucose Concentration	CMOS 350
[66]	Optical Detection, PH Sensing	10 × 10	4096	0.64×0.64	45μm Microbeads	N.A	CMOS 180
[13]	Fluorescence	250 × 250	56	3×3	DNA Molecule	DNA Hybridization	CMOS 350
[16]	Potential Recording, Impedance Sensing, Optical Detection	80 × 100	144	1.5×1.68	CMs, Neurons, Cancer	Extracellular Potential, Impedance/Optical Imaging, Bioluminescent	CMOS 130
[95]	Potential Recording, Impedance Sensing, Stimulation, Neurotransmitter Detection	13.5 × 13.5	59,760	4.48×2.43	Rat Cortical Neurons	Extracellular Potential, Stimulation	CMOS 180

Table 3.1. Comparison table of state-of-the art silicon-based biosensors

3.6. Conclusion

In this chapter, we present a 1024-pixel CMOS multimodality cellular interfacing array chip for holistic cell characterization and cell-based drug screening applications. Each pixel can be independently configured to perform extracellular potential recording, cellular impedance sensing, optical detection, and biphasic current stimulation. Each pixel size is 58μm×58μm including a 28μm×28μm gold-plated electrode and four 12μm×12μm photodiodes. We also present our in-house biocompatible packaging with robust solution resistance and demonstrate successful culturing of rat cardiomyocytes on the CMOS chip. The measured optical opacity image of on-chip cultured rat cardiomyocytes achieves high spatial resolution and closely matches the reference stereo microscope image. The measured extracellular potentials achieve high SNR and accurately capture the isoproterenol drug effects. Furthermore, real-time optical measurement of cardiomyocyte beating is demonstrated to record the transient cardiac muscle contraction and relaxation events and measure the cardiac beating rate, which aligns well with extracellular potential recording. The on-chip cultured rat cardiomyocytes are successfully paced with the on-chip biphasic current stimulator, and the pacing threshold and capture rate are also measured. The cell-based measurement results demonstrate the utility and benefit of the proposed CMOS multimodality cellular interfacing array system for fully automated and massively paralleled drug screening and new drug development in the pharmaceutical industry (Table 3.1).

CHAPTER 4

A CMOS 22K-PIXEL SINGLE-CELL RESOLUTION MULTI-MODALITY REAL-TIME CELLULAR SENSING ARRAY

This chapter presents a single-cell-resolution multimodality cellular interfacing array for holistic cell characterization and high-throughput drug screening. It contains 22,528 multimodality sensing pixels with a pixel size of 17μm×17μm. Each pixel contains a 4μm×4μm gold-plated electrode for extracellular potential recording and a 3μm×6μm photodiode for optical detection. To maintain high signal to noise ratio (SNR) despite the large electrode-electrolyte impedance due to small electrodes, we employ a DC-coupled chopper amplifier for extracellular potential recording that substantially minimizes front-end electronic noise. A proof-of-concept design is implemented in a standard 130nm CMOS process. It achieves a measured input-referred noise of 2.46μV_{rms} integrated from 1Hz to 4kHz at a chopping frequency of 20kHz, and cell-based measurements demonstrate real-time recorded action potentials with high SNR. Measured high-resolution optical shadow images provide the detailed cell and tissue morphology as well as the 2D distribution of on-chip cultured cells. Furthermore, this chapter presents the first CMOS sensing array that can successfully capture on-chip rat cardiomyocyte contraction using optical detection with action potential recordings for holistic cardiac cell characterizations.

4.1. Introduction

The built-in machineries in cells can be utilized in conjunction with electronic platforms to achieve unprecedented sensing and actuation capabilities far beyond conventional electronics-only devices. Cell-based assays are an excellent example of such "cell-electronics" hybrid systems that present unique advantages for chemical sensing and drug screening. First of all, cell-based assays directly use the physiological responses of living cells to examine new drugs, and therefore they provide physiologically relevant information that more accurately represents real-life biological behavior when compared to traditional biochemical assays. Moreover, cell-based assays can potentially achieve a high sensitivity/specificity as well as sample-in-answer-out fast response. Cell-based assays have been widely used in numerous high-impact applications such as drug discovery, epidemic disease detection, and environmental monitoring. In addition, cell-based assays also support personalized medicine, as patient derived cells can be directly used to test the potency, efficacy, and toxicity of patient-specific medicine.

Existing integrated cellular sensors are mostly of single-modality that only captures one type of cellular physiological change, e.g., extracellular potential [9], impedance [10], and optical absorption [13]. However, cells are highly complex systems with multi-physics and multi-parametric activities. For example, cells exhibit chemical activities such as anabolism and catabolism as well as mechanical activities including contraction, chemotaxis, and phototaxis. As a result, single-modality sensors cannot fully capture these multi-faceted responses; sensor platforms with multiple sensing modalities are necessary to simultaneously monitor multi-parametric cellular activities for holistic cell characterizations [16]-[19].

However, the reported multi-modality cellular sensors suffer from poor spatial resolution, since each sensing pixel needs to integrate multiple sensing functionalities. Therefore, in this chapter, we propose and demonstrate a CMOS multimodality sensor array with 22,528 pixels with a pixel size of 17μm×17μm (edge-to-edge), gold-plated electrode size of 4μm×4μm, and photodiode size of 3μm×6μm, achieving single-cell resolution for typical mammalian cells (10-20μm). Each sensor pixel supports extracellular potential recording, and optical detection for holistic cellular characterization. Note that the aggressive in-pixel electrode miniaturization increases the electrode-electrolyte impedance [21], making low-noise extracellular potential recording challenging. We employ a DC-coupled chopper amplifier to substantially reduce the front-end circuit noise and ensure overall high SNR in extracellular potential recording. The design details, biocompatible packaging, electrical measurements, and cell-based measurements are presented in the following sections.

4.2. A Single-Cell Resolution Multimodality CMOS Sensor Array Design

Figure 4.1 shows the system schematic of a 22k-pixel multimodality CMOS sensor array. It consists of 22 pixel groups each of which includes 16×64 pixels, switch matrices, a DC-coupled chopper amplifier, a photodiode readout circuit, a non-overlapping clock generation block, and a signal conditioning block. Each pixel contains one 4μm×4μm gold-plated electrode, one 3μm×6μm photodiode, transmission gate switches, and a buffer for the photodiode. Each 2×2 square of pixels can be accessed together as a sub-pixel group for extracellular potential recording and optical detection. For extracellular potential recording, two sub-pixel groups are selected, one as a sensing sub-pixel group and the other as a reference sub-pixel group. The signal conditioning block is composed of a high-pass

filter (HPF), a programmable low-pass filter (LPF), and a programmable gain amplifier (PGA) to process the output signals.

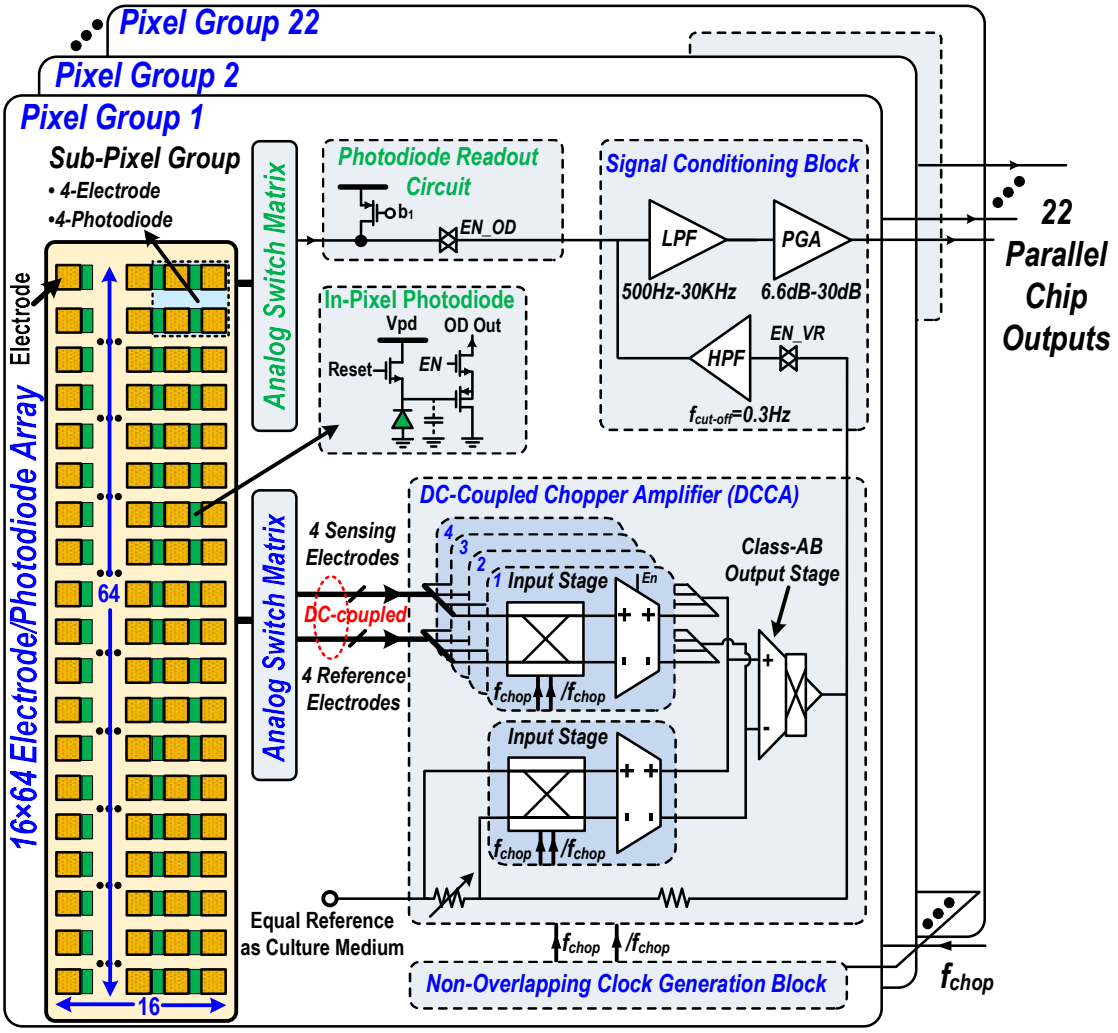

Fig. 4.1. Schematic of a 22k-pixel multimodality CMOS sensor array.

Figure 4.2 shows the detailed circuit schematic of the DC-coupled chopper amplifier (DCCA) for extracellular potential recording. It consists of five front-end input stages, four for sensing and one for feedback, and one Class-AB output stage. Each front-end input

stage contains a chopper circuit and gm cell. Note that two sub-pixel groups are selected and four input stages are either simultaneously enabled or sequentially enabled. For example, in many cases, cells are sparsely distributed and there could be only one cell or cell cluster within one selected sensing sub-pixel group (2×2 pixels) as shown in Fig. 4.3(a). In this case, we can simultaneously enable the four input stages to receive correlated signals from one cell and combine them at the Class-AB output stage, thereby maximizing the SNR. Note that the non-correlated noise such as circuit noise and DC-drift/offset at the electrode-electrolyte interface can be averaged out while the correlated signals are combined in the current domain. On the other hand, when multiple cells or cell clusters are located within one selected sensing sub-pixel group in Fig. 4.3(b), we use a time-multiplexing scheme among the four input stages to measure cell responses from each electrode individually to maximize the spatial resolution. Note that this arrangement can be readily extended to have more input stages with one Class-AB stage to construct a high-density array.

The dominant noise source for the bio-potential amplifier is the low-frequency flicker noise of CMOS devices [28]. Although chopping suppresses this flicker noise, it results in reduced amplifier input impedance ($1/2f_{chop}C_{DC}$) due to the chopping operation at the frequency f_{chop} with a large input DC blocking capacitor (C_{DC}) [96]. Note that high input impedance is critical for electrode safety (small DC current), low cut-off frequency, and high SNR (minimized signal attenuation at the electrode-electrolyte interface), especially for high density arrays with small electrodes. Therefore, we employ DC coupling at the front-end input stages, obviating the large DC blocking capacitor and achieving minimized input capacitance, which consists of the PMOS gate capacitance

shown in Fig. 4.2. Furthermore, since the chopping circuit can also largely suppress the V_{th} mismatches between PMOS differential pairs, the size of the PMOS differential pair can be very small. Considering the trade-off between the input capacitance and device V_{th} mismatches, we choose an input PMOS devices size of 9.8μm/240nm. The extracted input parasitic capacitance C_{in} is 2.5fF, resulting in an input impedance of $1/2f_{chop}C_{in}\approx 1G\Omega$ at the chopping frequency f_{chop} of 20kHz. In summary, DC-coupled chopping operations simultaneously achieve flicker noise suppression, high input impedance, and compact design, all of which are necessary for high-density design.

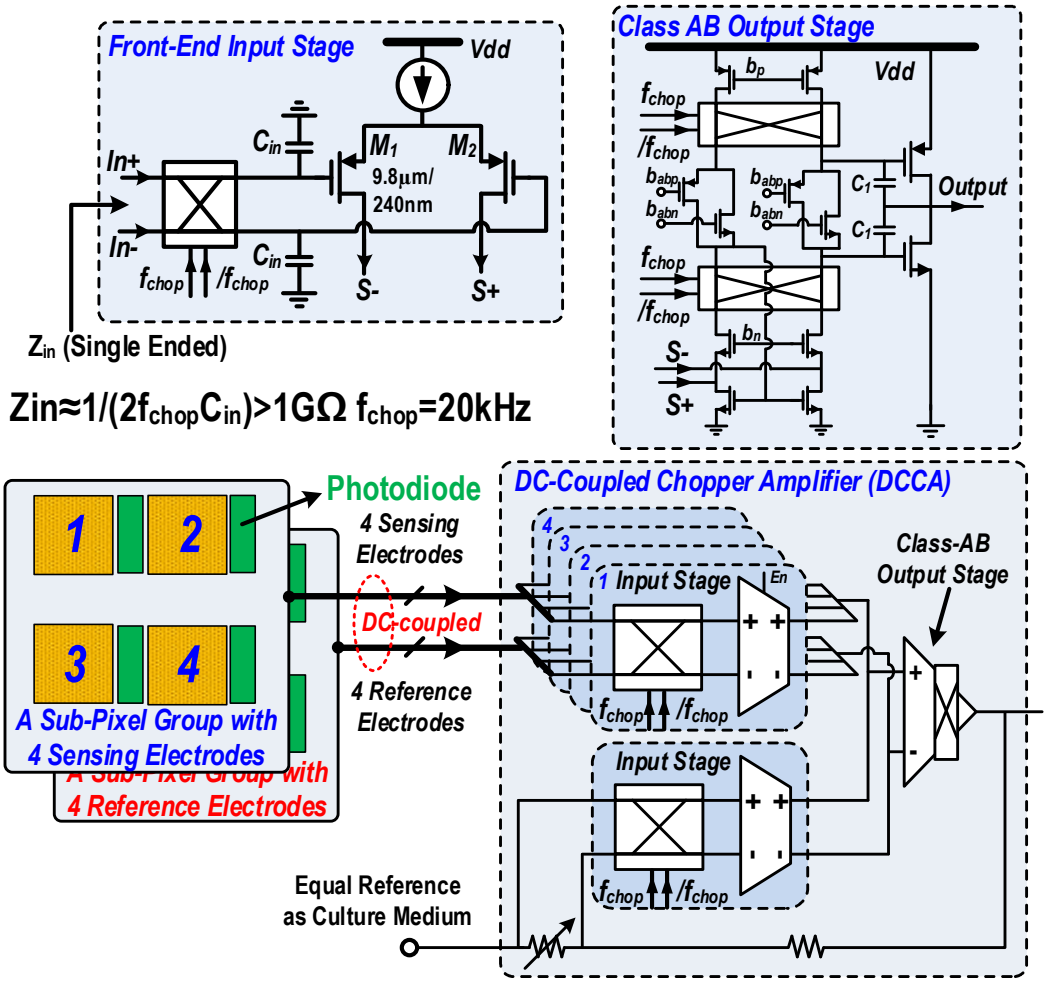

Fig. 4.2. Schematic of the DC-coupled chopper amplifier.

Since we employ DC coupling at the front-end input stages, special care must be taken for undesired DC-drifts/offsets at the electrode-electrolyte interface. The voltage gain of the DCCA can be programmed from 5.8dB to 33dB and the amplified DC-drift/offset is largely removed by the following HPF implemented in the signal conditioning block. Note that if we enable the four input stages simultaneously, the non-correlated DC-drift/offset can be averaged out, allowing us to have higher voltage gain in the DCCA.

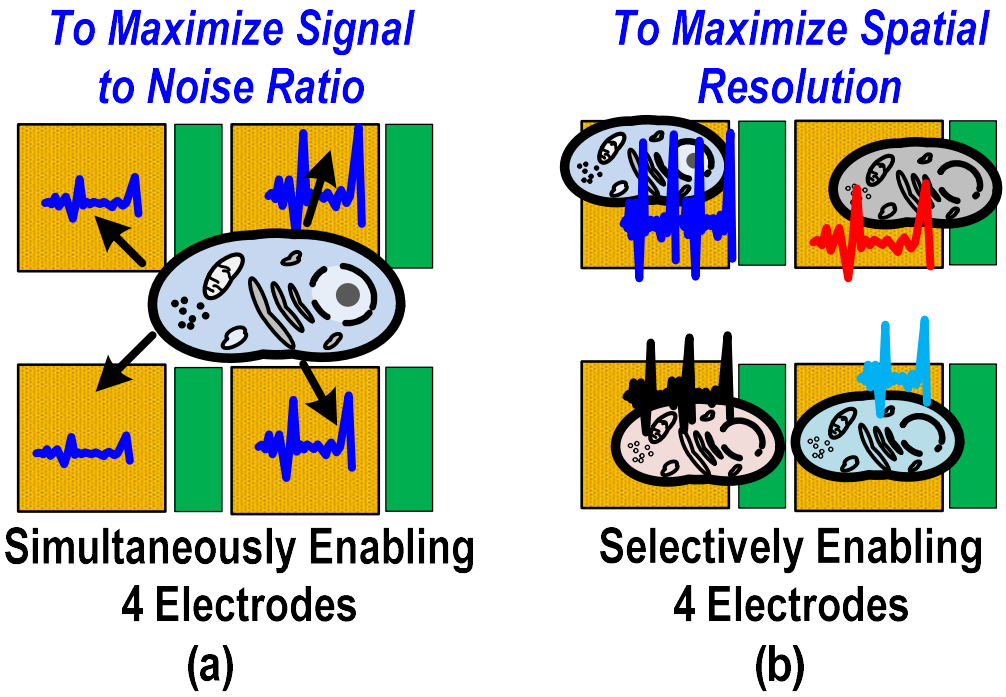

Fig. 4.3. (a) Single cell/cell cluster and (b) multiple cells/cell clusters located in the selected sensing pixel group.

For optical detection, one reverse-biased p+/nwell/psub 3μm×6μm photodiode, NMOS for reset, and buffer are implemented within each pixel as shown in Fig. 4.1. The

generated photon current at the photodiode, which is proportional to light intensity, is integrated in its parasitic capacitance and buffered out by a PMOS source follower.

4.3. Experimental Results

The proposed 22k-pixel multimodality sensor array is implemented in a standard 130nm CMOS process shown in Fig. 4.4. The entire chip occupies 4mm×4mm with a sensing area of 2.2mm×3.4mm, electrode size of 4µm×4µm, and photodiode size of 3µm×6µm. We perform standard electro-less gold plating for electrode safety and for creating a bio-compatible interface. To facilitate testing, we package the chip on a daughter board connected to a mother board (Fig. 4.5).

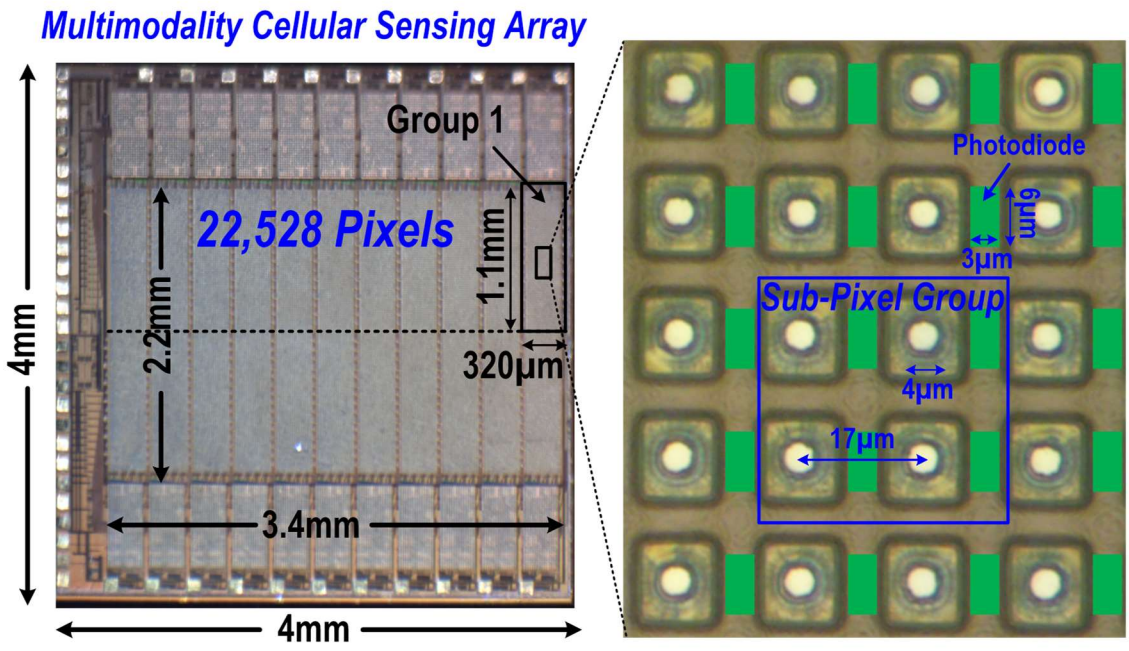

Fig. 4.4. Chip microphotograph.

After electro-less gold plating, we wash the chip surface using acetone, methanol, and isopropyl alcohol to remove organic residue in the sensing area. The chip is bonded to the daughter board, and the I/O pads are wire-bonded. We then apply medical epoxy to completely seal the bonding wires for high water resistance. Subsequently, we apply polydimethylsiloxane on top of the medical epoxy for biocompatibility. A standard 35mm cell culture plate with a laser-cut bottom is mounted onto the daughter board to contain the culture medium and cell samples while still housing the sensing array (Fig. 4.5).

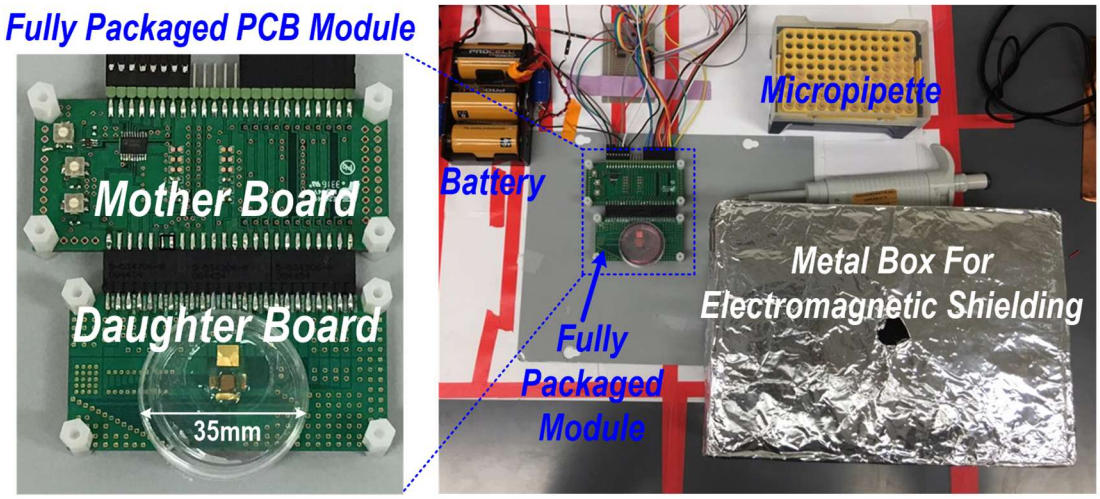

Fig. 4.5. Fully packaged module and cell-based measurement setup.

After packaging, the chip is electrically characterized. Figure 4.6(a) shows the measured voltage gain with a 20-kHz chopping frequency. The voltage gain and high cut-off frequency are fully programmable. Note that with a 6^{th}-order low-pass filter implemented in the signal conditioning block, the chopping noise can be largely eliminated (-60dB/dec). Figure 4.6(b) shows the measured input-referred noise with and without chopping operation. The measured input referred noise integrated from 1Hz to 4kHz is

2.46μV_{rms} with a chopping frequency at 20kHz. Compared to the measured integrated input referred noise of 17.08μV_{rms} without chopping operation, it achieves maximum 30-dB noise floor reduction as shown in Fig. 4.6(b). The rat cardiomyocyte action potential measurement results will further confirm low-noise performance.

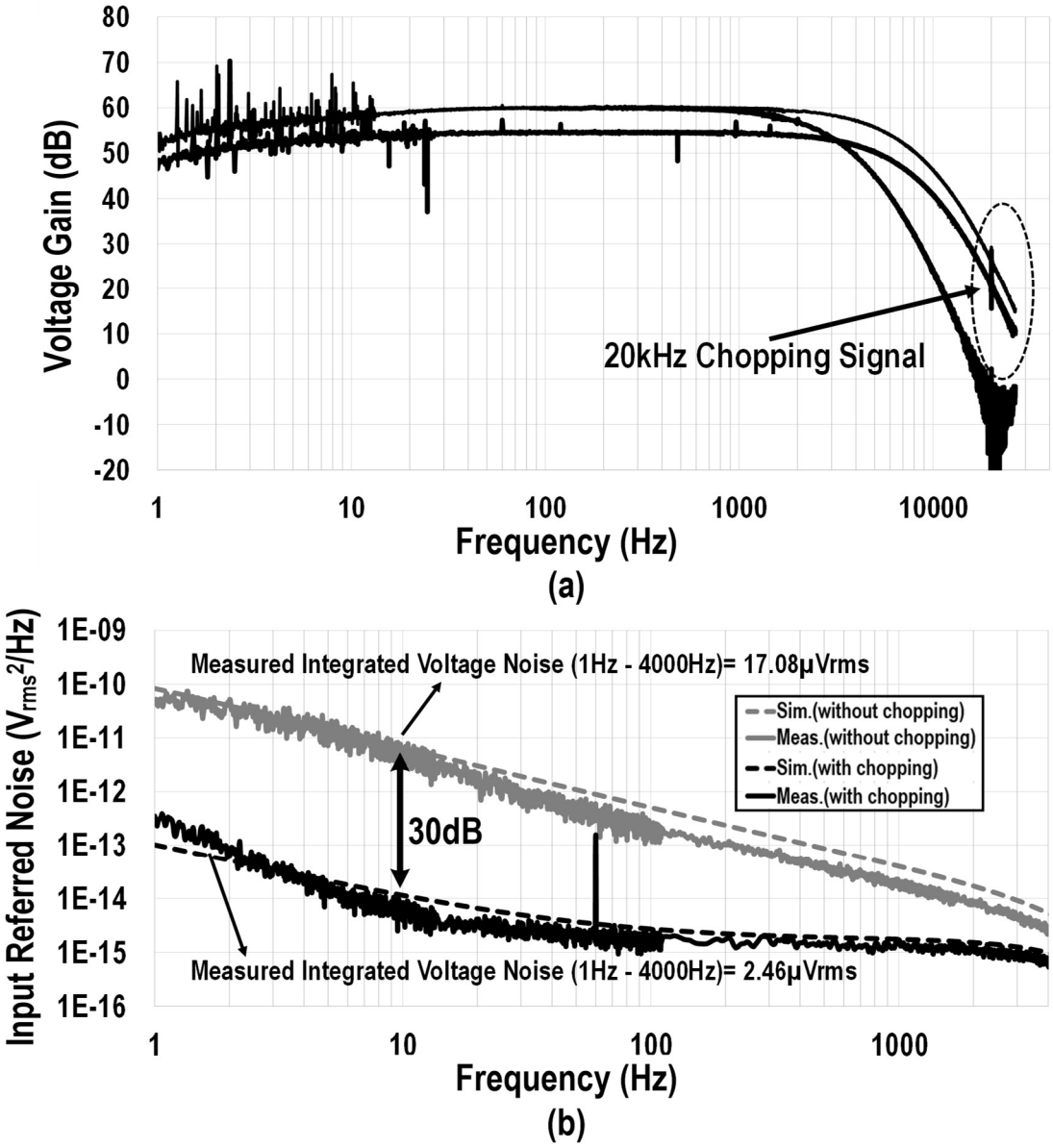

Fig. 4.6. (a) Measured voltage gain with chopping frequency of 20kHz and (b) input-referred noise with and without chopping operation.

Next, we perform cell-based measurements of on-chip cultured rat cardiomyocytes. First of all, 11,264 photodiodes (upper half chip) are scanned. The measured optical shadow image is shown in Fig. 4.7 and matches with the reference stereo microscope image. The measured optical shadow image depicts cell opacity, 2D cell distribution, and cell morphology.

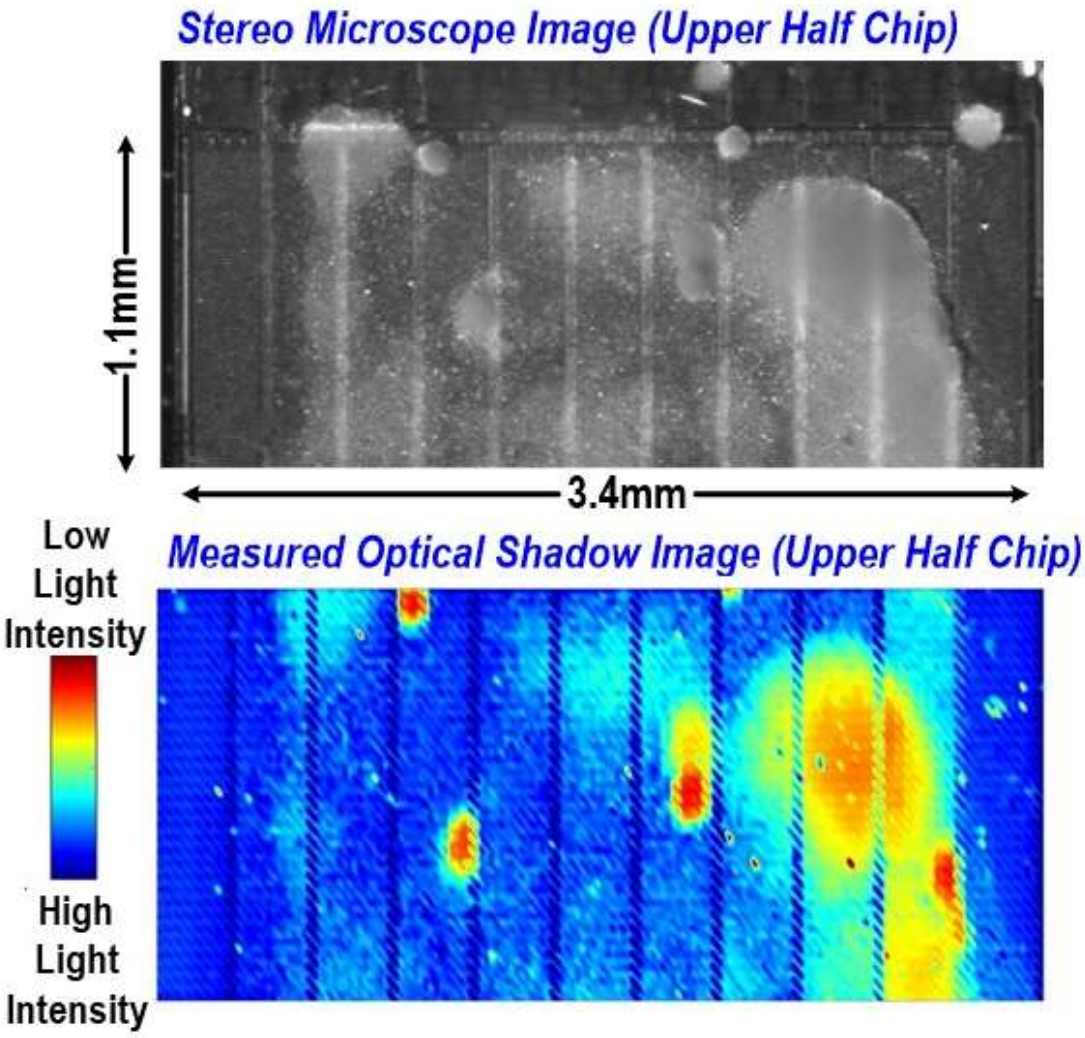

Fig. 4.7. Stereo microscope image and measured optical shadow image of on-chip cultured rat cardiomyocytes.

The extracellular potential recording with on-chip cultured rat-cardiomyocytes are performed with a 20-kHz chopping frequency, and the measured real-time action potentials shown in Fig. 4.8 demonstrate high SNR. The zoomed-in view of simultaneous action potential recording from multiple pixel groups shows that it preserves the same pattern over time with the action potential spike recorded at pixel group 4 always leading, showing action potential propagation and synchronized cardiac cell beating.

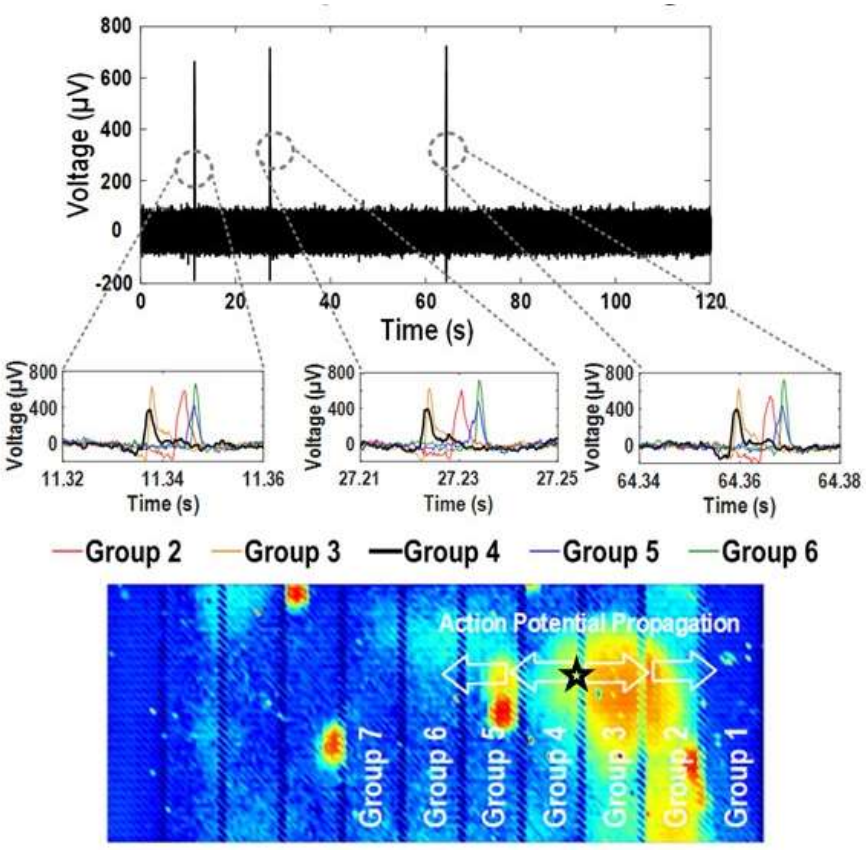

Fig. 4.8. Measured action potential spike of on-chip cultured cardiomyocytes.

The real-time measured action potentials of cardiomyocytes before and after isoproterenol administration are also shown in Fig. 4.9. After isoproterenol administration,

action potentials occur with faster and more uniform frequency but with decreased amplitude from 605.6μV to 384.3 μV, which is consistent with the expected effects of the isoproterenol.

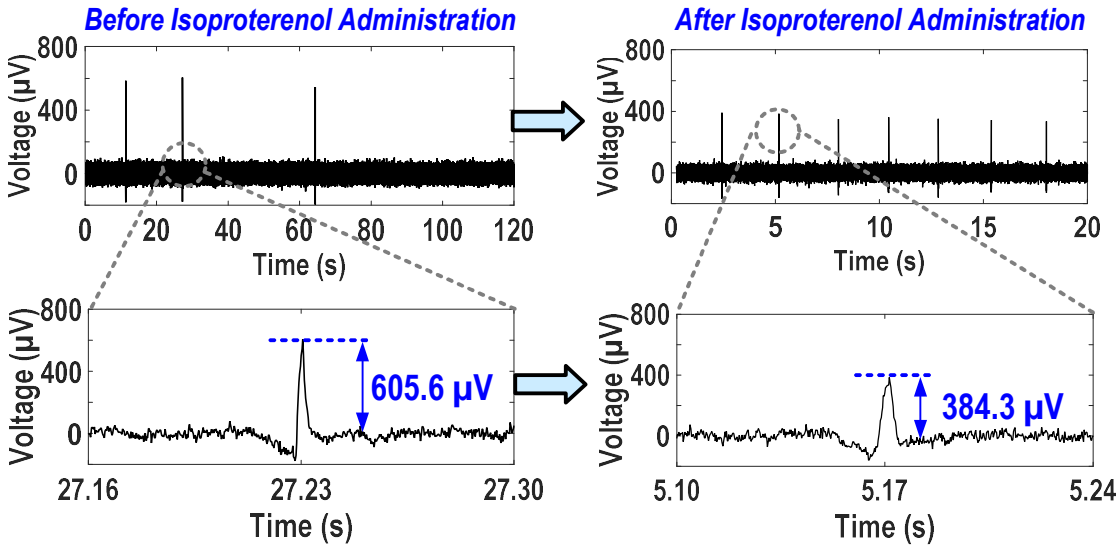

Fig. 4.9. Measured action potential of on-chip cultured cardiomyocytes before and after isoproterenol administration.

Optical detection can also be used to detect when cardiomyocytes contract [27]. Figure 4.10 illustrates how measuring the light intensity at a single pixel can capture cardiomyocyte contraction, thereby detecting cell contractility. The cardiac muscle fibers' contraction and relaxation can modulate the light transmittance of cardiomyocytes, and this modulation can be measured by the photodiode within each pixel. Figure 4.11 shows the measured real-time action potential and light intensity measurements. The frequency of the measured transient light intensity spikes aligns well with the measured action potential frequency, verifying that optical detection can successfully capture cardiomyocyte contraction. Note that action potentials occur due to the firing of ions, while the light

intensity spikes come from cardiac muscle fiber contraction and relaxation. Therefore, the measurement results shown in Fig. 4.11 demonstrate that our proposed multimodality sensor can capture multi-physical cellular physiological changes on the same cellular sample, showing the utility and unique benefit of the proposed multimodality sensing array.

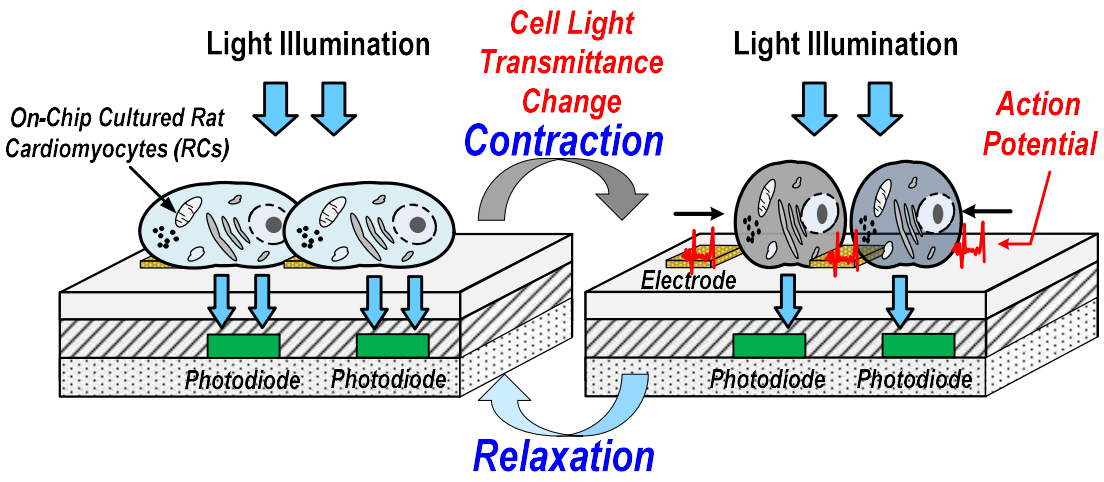

Fig. 4.10. Optical measurement methods to capture cardiac muscle fiber contraction/relaxation events.

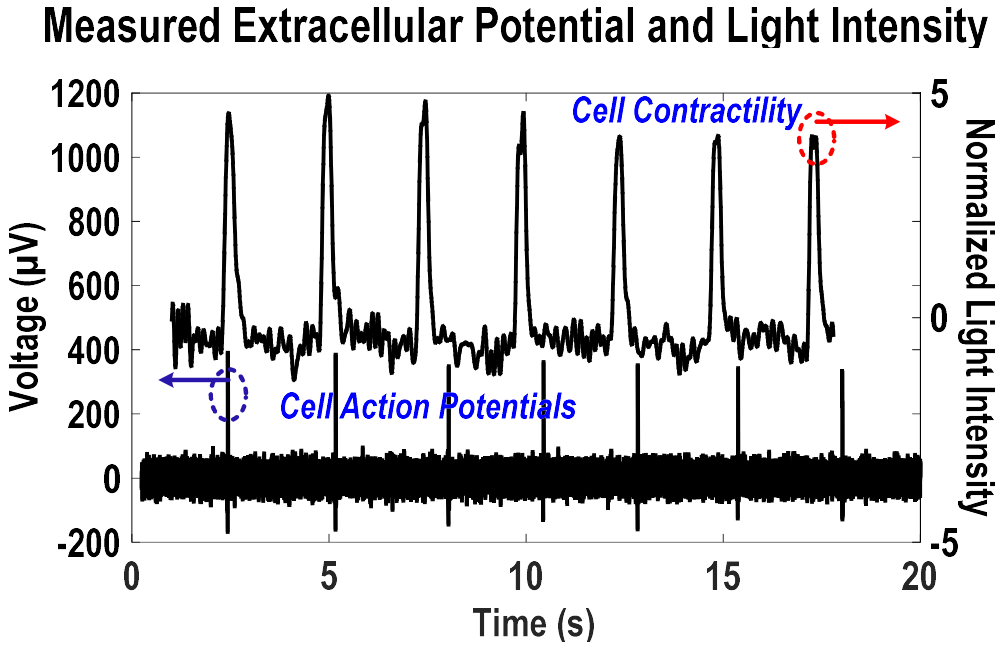

Fig. 4.11. Measured real-time action potentials and contractility.

4.4. Successive Approximation ADC Measurement Results

In this section, we will present the 10-bit successive approximation (SAR) ADC design and measurement results for the future work on multimodality joint sensor and stimulator cellular interfacing array with massively parallel recordings in chapter 5. The topology of the SAR ADC is presented in paper [97]. It uses a monotonic capacitor switching procedure to reduce average switching energy and total capacitance. Moreover, this topology can significantly simplify the digital circuits for successive approximation. The SAR ADC consists of bootstrapped switches, capacitor DACs, comparator, and SAR digital logic circuit. The required effective number of bits (ENOB) and sampling speed are 9-bit and 1Msample/s. With the typical extracellular recording sampling rate of 10KHz, single ADC can be time-multiplexed by 100 potential recording amplifiers. In order to improve the linearity performance, we choose the unit capacitance value of 49fF.

Figure 4.12 shows the measured FFT spectrum with the target sampling rate of 1MS/s and input sinusoidal signal frequency of 200KHz. The measured signal-to-noise and distortion ratio (SINAD), signal-to-noise ratio (SNR), and effective number of bits (ENOB) are 52.4dB, 62.03 dB, and 8.4 bits, respectively. The excessive ADC output harmonic distortion is mainly due to the harmonic distortion of the input signal generator (Keysight 81160A), which exhibits the harmonic distortion of -63dBc. Figure 4.13 shows the measured differential nonlinearity (DNL) and integral nonlinearity (INL). The measured DNL and INL are within 0.61LSB and 0.74LSB, respectively.

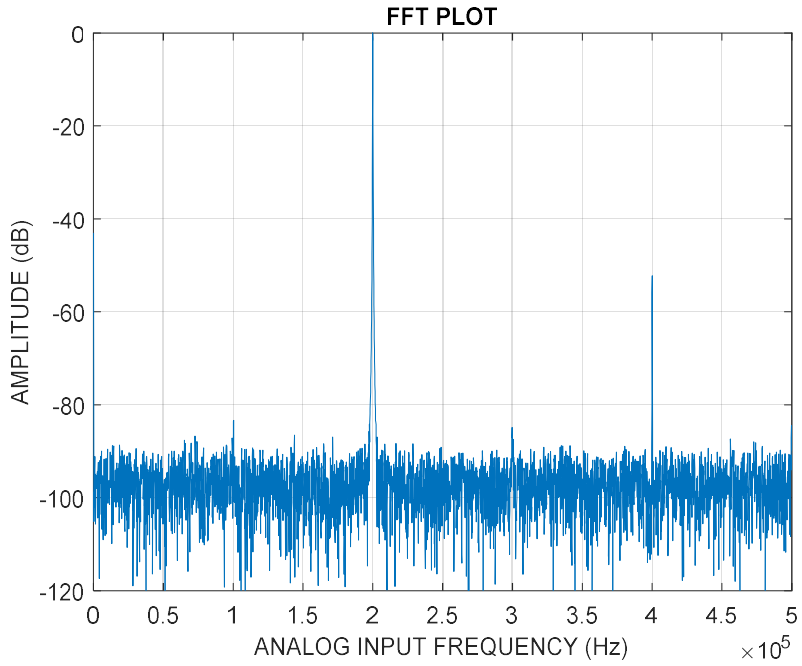

Fig. 4.12. Measured FFT spectrum at 1MSample/s with the input sine wave at 200KHz.

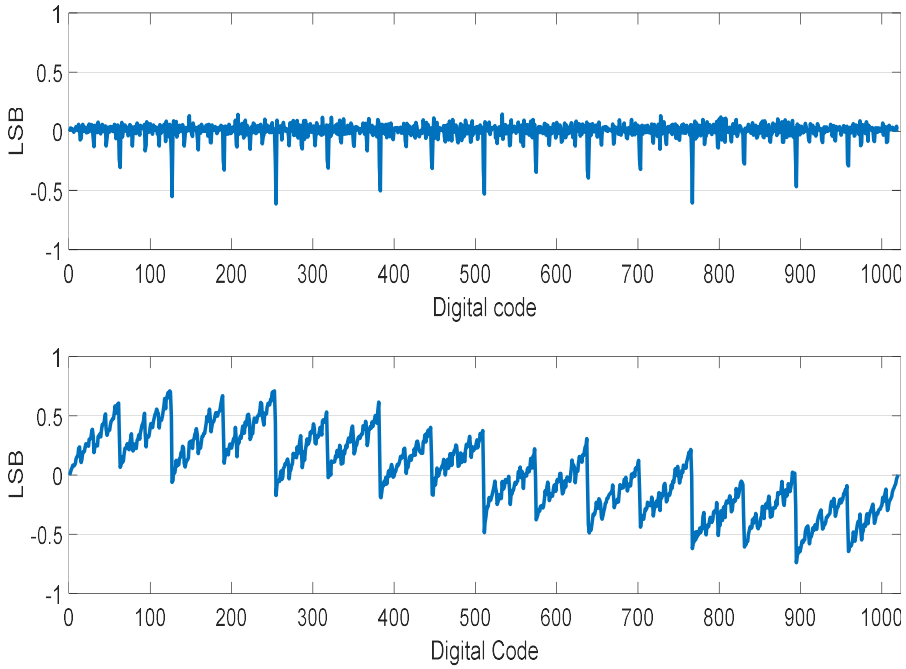

Fig. 4.13. Measured differential nonlinearity (DNL) and integral nonlinearity (INL).

4.5. Conclusion

This chapter presents a 22k-pixel multimodality sensing array with a DCCA for cell characterization and drug screening. DCCA achieves the measured input-referred noise of 2.46μV_{rms} and cell-based measurements successfully capture the beating rate of cardiomyocytes using both optical detection and potential recording (Table 4.1.). Additionally, drug effects of isoproterenol are successfully characterized, and the cardiomyocyte culture is successfully imaged.

	Sensing Modality	# of Sensor	Noise (Bandwidth)	Pixel Size μm^2	Cell-Based Assay	Tech
This Work	**VR+OD**	**22k**	**2.45μV_{Rms} (1Hz-4KHz)**	**17×17**	**Cardiomyocyte**	**130nm CMOS**
[9]	VR	26k	5.9μV_{Rms} (1Hz-10KHz)	17.5×17.5	Neuron	350nm CMOS
[10]	IS	100	577pA_{rms} (1Hz-1KHz)	100×100	DNA+Protein	350nm CMOS
[19]	VR+OD+IS	1024	16μV_{rms} (0.3Hz-400KHz)	58×58	Human Ovarian Cancer Cell	130nm CMOS
[99]	VR	8	9μV_{rms} (1Hz-5KHz)	N.A	N.A	40nm CMOS

VR: Voltage Recording, IS: Impedance Sensing, and OD: Optical Detection

Table 4.1. Performance comparison.

CHAPTER 5

FUTURE WORK

5.1. Introduction

Since the cell signals are encoded by temporal dynamics and spatial gradients, massive parallel recording channels are very important to decode the temporally coupled cellular signals and high spatial resolution is also critical to analyze the spatially coupled cellular signals. Due to the large number of combinations between diseases relevant cell lines and compound libraries, drug screening could be very time consuming and labor intensive. Therefore, high throughput is very critical for fully automated drug screening applications. However, with the increased spatial resolution or decreased pixel size, the electrode-electrolyte impedance increases substantially. The large electrode-electrolyte impedance results in additional noise for extracellular potential recordings and measurement artifacts due to the electrode-electrolyte impedance degrade the accuracy of the cellular impedance.

As a future work, I will investigate in increasing the number of parallel channels for each modality by utilizing the time-multiplexing operation of the on-chip analog-to-digital converter (ADC). Also, I will further reduce the pixel size without compromising the number of modalities. In addition, I will investigate on the electrode materials such as titanium nitride and iridium oxide to minimize the electrode-electrolyte impedance and the electrode-electrolyte impedance artifacts. The 4-point impedance measurements will be

employed in the future design to precisely de-embed the electrode-electrolyte impedance for cellular impedance measurements. In this chapter, we will present the multimodality joint sensor and stimulator design architecture and potential electrode materials for low noise and reliable stimulations.

5.2. Multimodality Joint Sensor and Stimulator Cellular Interfacing Array with Massively Parallel Recording Channels

Figure 5.1 shows the schematic of the multimodality joint sensor and stimulator cellular interfacing array with massively parallel recording channels of N_C. It consists of electrode and photodiode arrays, pixel multiplexers, potential recording amplifiers ($\times N_C$), optical sensing read-out buffers ($\times N_C$), one 4-point impedance measurement block, two successive approximation ADCs, two time multiplexers, and a digital control unit. In order to achieve massively parallel extracellular potential recordings with the channel number of N_C, each channel should have individual potential recording amplifier due to the following reasons. Since each pixel electrode exhibits its own DC offset and/or DC drift, if the pixels are time-multiplexed with one shared potential recording amplifier at very fast scan rate, the DC offset and/or DC drift from pixels are modulated and fall into in-band frequency of potential recording amplifier and could saturate the following potential recording amplifier. Furthermore, for simultaneous recordings between extracellular potential and optical detection, we employ two separate successive approximation ADCs.

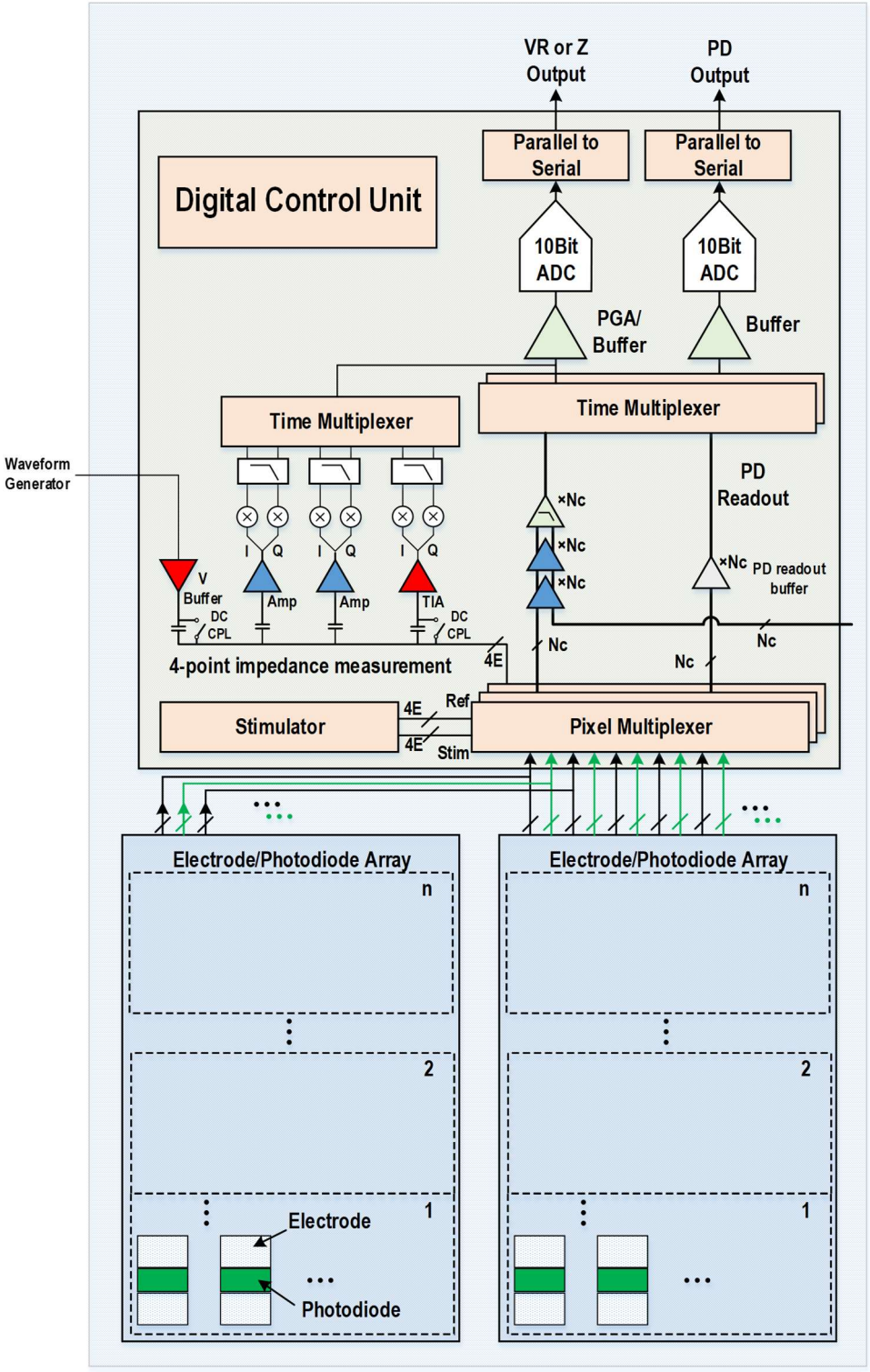

Fig. 5.1. Schematic of a multimodality joint sensor and stimulator array unit with massively parallel recording channels.

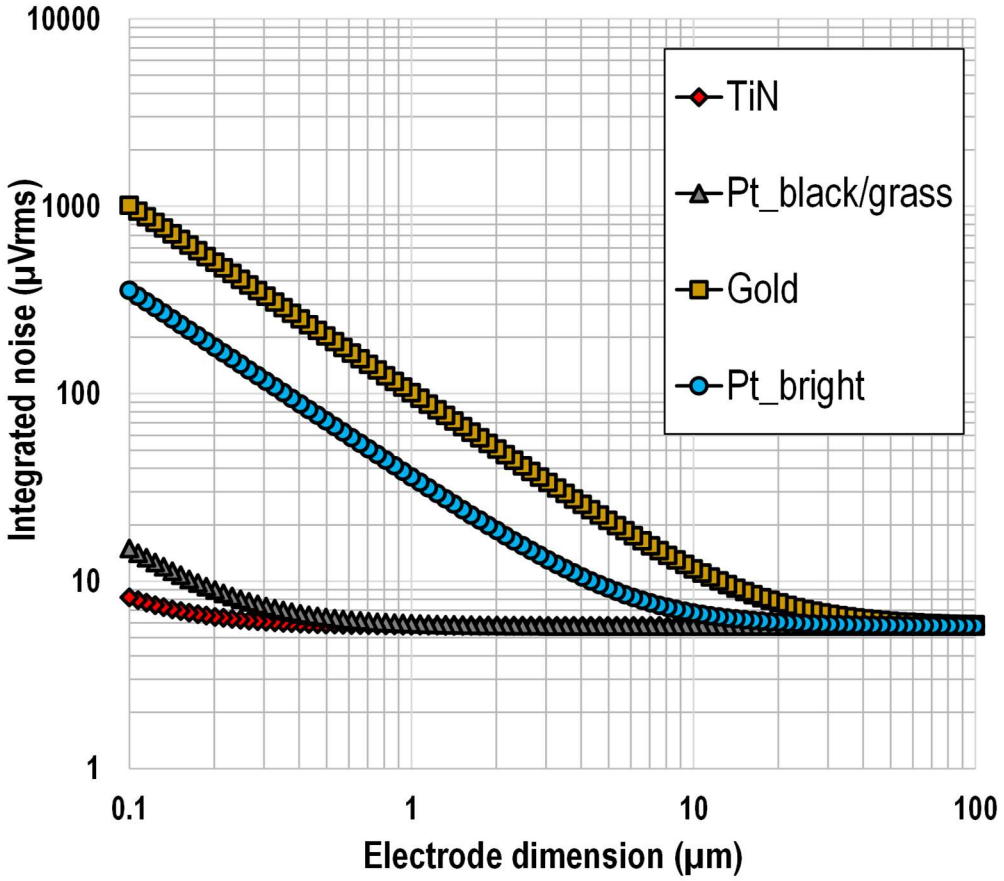

Fig. 5.2. Simulated integrated noise versus electrode dimension with different electrode materials.

5.3. Electrode Modifications

Figure 5.2. shows the simulated noise integrated from 0.3Hz to 20KHz versus electrode dimension with different electrode materials. It shows that the simulated integrated noises for gold, platinum bright, platinum black/glass, and titanium nitride with the electrode diameter of 1μm are 101μV_{rms}, 36μV_{rms}, 5.92μV_{rms}, and 5.79μV_{rms}, respectively. The electrode noise with gold electrode is 17.4 times larger than the electrode noise with titanium nitride electrode. Furthermore, the recent studies [98] show that the

titanium nitride and iridium oxide electrodes can reliably be used for long-term current/voltage stimulation with high stimulation efficacy and efficiency. Therefore, I will investigate on modifying the current gold electrodes to titanium nitride electrodes.

CHAPTER 6

CONCLUSION

6.1. Research Summary

The proposed research is to develop multimodality CMOS sensor array for holistic cellular characterization and cell-based drug screening. Cells are the basic structural, functional, and biological units of all known living organisms. Understanding the physiological behaviors of living cells and tissues is a prerequisite to further advance bioscience and biotechnologies, such as synthetic biology, stem cell manufacturing, and regenerative medicine. Moreover, both wide-type and genetically modified cells have been widely used as powerful sensing and diagnostic tools in cell-based assays; these assays are the key enablers in numerous high-impact applications, including characterizing the potency, efficacy, and toxicity of new drugs in pre-clinical pharmaceutical development, determining the patient-specific treatments in personalized medicine, fast pathogen screening for epidemic disease detections, and detecting biohazards and pollutants in environmental monitoring. However, cells are highly complex systems often with concurrent multi-physics responses when subjected to external stimuli, which cannot be captured by conventional single-modality sensors, e.g., with electrical or optical only detections. Furthermore, cell signals could be encoded by spatiotemporal dynamics. Thus, there is an unmet need for new multi-modality sensor arrays comprised of pixels each capable of detecting multi-physics cellular responses together with actuations.

In this thesis, we demonstrate a fully integrated 144-pixel multimodality sensor array in a standard CMOS process. The sensor array characterizes four different cell physiological parameters, i.e., extracellular voltage recording, cellular impedance

mapping, optical shadow imaging/bioluminescence imaging, and temperature monitoring in a real-time joint-modality fashion with the pixel size of 80μm×100μm. Electrical measurements and extensive biological experiments with different types of living cells are performed to demonstrate the functionalities of the proposed multi-modality sensing in holistic cell characterization, cell-based assay and drug screening. Next, this design is extended to a 1024-pixel multimodality joint sensor and stimulator cellular interfacing array. The biphasic current stimulator is added to pace the cardiomyocytes and to precisely capture the drug effects under the uniform pacing condition. In addition, the pixel size is significantly reduced to 58μm×58μm for high spatial resolution. The measured optical opacity image of on-chip cultured rat cardiomyocytes achieves high spatial resolution and closely matches the reference stereo microscope image. The measured extracellular potentials achieve high SNR and accurately capture the isoproterenol drug effects. Furthermore, real-time optical measurement of cardiomyocyte beating is demonstrated to record the transient cardiac muscle contraction and relaxation events and measure the cardiac beating rate, which aligns well with extracellular potential recording. The on-chip cultured rat cardiomyocytes are successfully paced with the on-chip biphasic current stimulator, and the pacing threshold and capture rate are also measured. The cell-based measurement results demonstrate the utility and benefit of the proposed CMOS multimodality cellular interfacing array system for fully automated and massively paralleled drug screening and new drug development in the pharmaceutical industry. The multimodality pixel resolution is further reduced to a single-cell resolution with the pixel size of 17μm×17μm.

6.2. List of Publications

[C1] **J. Park**, M. K. Aziz, S. Gonzalez, D. Jung, T. Chi, S. Li, H. C. Cho, H. Wang, "A CMOS 22k-Pixel Single-Cell Resolution Multi-Modality Real-Time Cellular Sensing Array," *IEEE Custom Integrated Circuits Conference* (***CICC***), May 2017.

[C2] **J. Park**, Y. Wang, S. Pellerano, C. Hull, H. Wang, "A 24dBm 2-to-4.3GHz Wideband Digital Power Amplifier with Built-In AM-PM Distortion Self-Compensation," *IEEE International Solid-State Circuits Conference (**ISSCC**) Dig. Tech. Papers*, Feb. 2017.

[C3] T. Chi, F. Wang, S. Li, M. Huang, **J. Park**, and H. Wang, "A 60GHz On-Chip Linear Radiator with Single-Element 27.9dBm Psat and 33.1dBm Peak EIRP Using Multi-Feed Antenna for Direct On-Antenna Power Combining," *IEEE International Solid-State Circuits Conference (**ISSCC**) Dig. Tech. Papers*, Feb. 2017.

[C4] **J. Park**, M. K. Aziz, T. Chi, A. Su, A. Zhao, H. C. Cho, M. Styczynski, and H. Wang, "Live Demonstration: CMOS Multi-Modality Sensing Array for Drug Screening and Cell-Based Assays", *Proc. IEEE **SENSORS***, Oct. 2016.

[C5] S. Li, T. Chi, **J. Park**, and H. Wang, "A Multi-Feed Antenna for Antenna-Level Power Combining", *in Proc. IEEE AP-S/URSI*, June 2016.

[C6] **J. Park**, T. Chi, A. Su, C. Zhu, J. H. Sung, H. C. Cho, M. Styczynski, and H. Wang, "A High-Density CMOS Multi-Modality Joint Sensor/Stimulator Array with 1024 Pixels for Holistic Real-Time Cellular Characterization", *in Proc. IEEE VLSI Tech. Cir. Symp. (**VLSI**),* June 2016.

[C7] **J. S. Park**, T. Chi, A. Su, C. Zhu, J. Butts, T. Hookway, T. McDevitt, M. Styczynski, and H. Wang, "Live Demonstration: A Multi-Modality CMOS Sensor Array

for Cell-Based Assay and Drug Screening," *IEEE Biomedical Circuits and Systems Conference* (***BioCAS***), Oct. 2015.

[C8] **J. Park**, S. Hu, Y. Wang, and H. Wang, "A Highly Linear Dual-Band Mixed-Mode Polar Power Amplifier in CMOS with An Ultra-Compact Output Network," *IEEE Custom Integrated Circuits Conference (**CICC**) Dig. Tech. Papers*, Sep. 2015. **2015 CICC Best Student Paper Award.**

[C9] T. Li., **J. Park**, and H. Wang, "A 2-24GHz 360-Degree Full-Span Differential Vector Modulator Phase Rotator with Transformer-Based Poly-Phase Quadrature Network," *IEEE Custom Integrated Circuits Conference (**CICC**) Dig. Tech. Papers*, Sep. 2015. **2015 CICC Best Student Paper Award Finalist.**

[C10] **J. Park** and H. Wang, "A Transformer-Based Poly-Phase Network for Ultra-Broadband Quadrature Signal Generation," *IEEE MTT-S Int. Microwave Symp. (**IMS**),* May 2015.

[C11] **J. Park**, T. Chi, J. Butts, T. Hookway, T. C. McDevitt, and H. Wang, "A Multi-Modality CMOS Sensor Array for Cell-Based Assay and Drug Screening," *IEEE International Solid-State Circuits Conference (**ISSCC**) Dig. Tech. Papers*, Feb. 2015.

[C12] S. Lepkowski, **J. Park**, T. Chi, and H. Wang, "A Transformer Based Ultra-Compact 8×8 Mm-Wave Butler Matrix Fully Integrated in 65nm Bulk CMOS," *Government Microcircuit Applications and Critical Technology Conference (**GOMACTech**)*, Mar. 2015.

[C13] T-W Li, **J. Park**, and H. Wang, "An Ultra-broadband 360° Full-Span Transformer-Based Differential Vector Modulator Phase Rotator In CMOS,"

*Government Microcircuit Applications and Critical Technology Conference (**GOMACTech**)*, Mar. 2015.

[C14] H. Wang, A. Mohadavi, **J. Park**, T. Chi, J. Butts, T. A. Hookway, T. McDevitt, D. A. Tirrell, A. Hajimiri, "Cell Culture and Cell Based Sensors on CMOS," (Invited) *IEEE Biomedical Circuits and Systems Conference (**BioCAS**) Dig. Tech. Papers*, Oct. 2014.

[C15] **J. Park**, T. Chi, S. Hu, M. Styczynski, H. Wang, "A Scalable CMOS Cell Sensor Array," *Semiconductor Research Corporation **SRC TECHCON** Dig. Tech. Papers*, Sept. 2014.

[C16] T. Chi, **J. Park**, R. L. Schmid, A. C. Ulusoy, J. D. Cressler, and H. Wang, "A Low-Power and Ultra-Compact W-band Transmitter Front-End in 90nm SiGe BiCMOS Technology," *IEEE Bipolar/BiCMOS Circuits and Technology Meeting (**BCTM**) Dig. Tech. Papers*, Sep. 2014.

[C17] **J. Park** and H. Wang, "A K-Band 5-Bit Digital Linear Phase Rotator with Folded Transformer Based Ultra-Compact Quadrature Generation," *IEEE Radio Frequency Integrated Circuits Symposium*, (***RFIC***) 2014.

[C18] S. Hu, S. Kousai, **J. Park**, O. Chlieh, and H. Wang, "A +27.3dBm Transformer-Based Digital Doherty Polar Power Amplifier Fully Integrated in Bulk CMOS," *IEEE Radio Frequency Integrated Circuits Symposium*, (***RFIC***) 2014. **2014 RFIC Best Student Paper Award (1st Place).**

[C19] **J. Park**, T. Chi, and H. Wang, "An Ultra-Broadband Compact Mm-Wave Butler Matrix in CMOS for Array-Based MIMO Systems," *IEEE Custom Integrated Circuits Conference* (***CICC***), Sep. 2013.

[C20] **J. Park**, S. Kousai, and H. Wang, "A Fully Differential Ultra-Compact Broadband Transformer Based Quadrature Generation Scheme," *IEEE Custom Integrated Circuits Conference* (***CICC***), Sep. 2013.

[C21] **J. Park** and H. Wang, "A Passive Quadrature Generation Scheme for Integrated RF Systems," *IEEE MTT-S International Wireless Symposium* (***IWS***), Apr. 2013.

[J1] S. Hu, S. Kousai, **J. Park**, O. Chlieh, and H. Wang, "Design of A Transformer-Based Reconfigurable Digital Polar Doherty Power Amplifier Fully Integrated in Bulk CMOS," *IEEE J. of Solid-State Circuits* (***JSSC***), vol. 50, no. 5, pp. 1094-1106, May 2015.

[J2] **J. Park** and H. Wang, "A Transformer-Based Poly-Phase Network for Ultra-Broadband Quadrature Signal Generation," *IEEE Trans. Microw. Theory. Tech (**T-MTT**)*, vol. 63, no. 12, pp. 4444-4457, Dec 2015.

[J3] **J. Park** and H. Wang, "A Fully Differential Ultra-Compact Broadband Transformer-Based Wilkinson Power Divider," *IEEE Microwave and Wireless Component Letters (**MWCL**),* vol. 26, no. 4, pp.255-257, April 2016.

[J4] T. Chi, **J. Park**, J. C. Butts, T. A. Hookway, A. Su, C. Zhu, M. P. Styczynski, T. C. McDevitt, and H. Wang, "A Multi-Modality CMOS Sensor Array for Cell-Based Assay and Drug Screening," *IEEE Trans. Biomed. Circuits Syst. (**T-BCAS**),* vol. 9, no. 6, pp. 801-814, Dec. 2015.

[J5] **J. Park**, S. Hu, Y. Wang, and H. Wang, "A Highly Linear Dual-Band Mixed-Mode Polar Power Amplifier in CMOS with An Ultra-Compact Output Network," *IEEE J. of Solid-State Circuits (**JSSC**),* vol. 51, no. 8, pp. 1756 - 1770, Aug. 2016.

[J6] M. Zia, T. Chi, **J. Park**, A. Su, J. L. Gonzalez, P. K. Jo, M. P. Styczynski, H. Wang, and M. S. Bakir, "A 3D Integrated Electronic Microplate Platform for Lowcost Repeatable Biosensing Applications," *IEEE Trans. Compon., Packag., Manuf. Technol.* (***T-CPMT***), vol. 6, no. 12, pp. 1827 - 1833, Dec. 2016.

[J7] T. Chi, S. Li, **J. Park**, and H. Wang, "A Multi-Feed Antenna for High-Efficiency On-Antenna Power Combining," *accepted and to appear in IEEE Trans. Antennas Propag.(**T-AP**)*, 2017.

[J8] **J. Park**, M. K. Aziz, S. Li, T. Chi, S. I. Grijalva, J. Sung, H. Cho, and H. Wang, "1024-Pixel CMOS Multi-Modality Joint Cellular Sensor/Stimulator Array for Real-Time Holistic Cellular Characterization and Cell-Based Drug Screening" *accepted and to appear in IEEE Trans. Biomed. Circuits Syst.(**T-BCAS**),* 2017.

[J9] **J. Park**, Y. Wang, S. Pellerano, C. Hull, H. Wang, "A CMOS Wideband Current-Mode Digital Polar Power Amplifier with Built-In AM-PM Distortion Self-Compensation," *accepted and to appear in IEEE J. of Solid-State Circuits (**JSSC**),* 2017.

REFERENCES

[1] B. Alberts, D. Bray, K. Hopkin, A. D. Johnson, A. Johnson, J. Lewis, M. Raff, K. Roberts, and P. Walter, Essential Cell Biology, 4th ed. New York, NY, USA: Garland Science, 2013.

[2] D. Randall, W. Burggren, and K. French, Eckert Animal Physiology: Mechanisms and Adaptations, 5th ed. San Francisco, CA, USA: Freeman, 2001.

[3] B. Alberts, A. Johnson, J. Lewis, D. Morgan, M. Raff, K. Roberts, and P. Walter, Molecular Biology of the Cell, 4th ed. New York, NY, USA: Garland Science, 2002.

[4] R. A. Meyers, Synthetic Biology (Current Topics From the Encyclopedia of Molecular Cell Biology and Molecular Medicine), 1st ed. Hoboken, NJ, USA: Wiley, 2015.

[5] C.-F. Mandenius and M. Björkman, Biomechatronic Design in Biotechnology: A Methodology for Development of Biotechnological Products. Hoboken, NJ, USA: Wiley, 2011.

[6] C. M. Metallo, S. M. Azarin, L. Ji, J. J. De Pablo, and S. P. Palecek, "Engineering tissue from human embryonic stem cells," J. Cell. Molecular Med., vol. 12, no. 3, pp. 709–729, 2008.

[7] R. R. Harrison and C. Charles, "A low-power low-noise CMOS amplifier for neural recording applications," IEEE J. Solid-State Circuits, vol. 38, no. 6, pp. 958–965, Jun. 2003.

[8] B. Eversmann, M. Jenkner et al., "A 128×128 CMOS biosensor array for extracellular recording of neural activity," IEEE J. Solid-State Circuits, vol. 38, no. 12, pp. 2306–2317, Dec. 2003.

[9] M. Ballini, J. Muller, P. Livi, Y. Chen et al., "A 1024-channel CMOS microelectrode array with 26,400 electrodes for recording and stimulation of electrogenic cells in vitro," IEEE J. Solid-State Circuits, vol. 49, no. 11, pp. 2705–2719, Nov. 2014.

[10] A. Manickam, A. Chevalier, M. McDermont, A. Ellington, and A. Hassibi, "A CMOS electrochemical impedance spectroscopy (EIS) biosensor array," IEEE Trans. Biomed. Circuits Syst., vol. 4, no. 6, pp. 379–390, Dec. 2010.

[11] M. Schienle, C. Paulus, A. Frey, F. Hofmann, B. Holzapfl, P. Schindler-Bauer, and R. Thewes, "A fully electronic DNA sensor with 128 positions and in-pixel A/D conversion," IEEE J. Solid-State Circuits, vol. 39, no. 12, pp. 2438–2455, Dec. 2004.

[12] Y. Schmid, S. Burgel, P. Misun, A. Hierlemann, and O. Frey, "Electrical impedance spectroscopy for microtissue spheroid analysis in hanging-drop networks," ACS Sens., 1 (8), pp 1028–1035, July. 2016.

[13] B. Jang, P. Cao, A. Chevalier, A. Ellington, and A. Hassibi, "A CMOS fluorescent-based biosensor microarray," in Proc. IEEE ISSCC, Dig. Tech. Papers, 2009, pp. 436–437.

[14] G. Patounakis, K. L. Shepard, and R. Levicky, "Active CMOS array sensor for time-resolved fluorescence detection," IEEE J. Solid-State Circuits, vol. 41, no. 11, pp. 2521–2530, Nov. 2006.

[15] H. Eltoukhy, K. Salama, and A. Gamal, “A 0.18-µm CMOS bioluminescence detection lab-on-chip,” IEEE J. Solid-State Circuits, vol. 41, no. 3, pp. 651–662, Mar. 2006.
[16] J. Park et al., “A multimodality CMOS sensor array for cell-based assay and drug screening,” IEEE ISSCC, pp. 208-209, Feb. 2015.
[17] T. Chi, J. S. Park, J. C. Butts, T. A. Hookway, A. Su, C. Zhu, M. P. Styczynski, T. C. McDevitt, and H. Wang, “A Multi-Modality CMOS Sensor Array for Cell-Based Assay and Drug Screening,” IEEE Trans. Biomed. Circuits Syst., vol. 9, no. 6, pp. 801-814, Dec. 2015.
[18] J. S. Park, T. Chi, A. Su, C. Zhu, J. Butts, T. Hookway, T. McDevitt, M. Styczynski, and H. Wang, “Live Demonstration: A Multi-Modality CMOS Sensor Array for Cell-Based Assay and Drug Screening,” Proc. IEEE Biomedical Circuits and Systems Conference, Oct. 2015.
[19] J. Park, T. Chi, A. Su, C. Zhu, J. H. Sung, H. C. Cho, M. Styczynski, and H. Wang, "A High-Density CMOS Multi-Modality Joint Sensor/Stimulator Array with 1024 Pixels for Holistic Real-Time Cellular Characterization", Proc. IEEE VLSI Tech. Cir. Symp., June 2016.
[20] J. Park, M. K. Aziz, S. Li, T. Chi, S. I. Grijalva, J. Sung, H. Cho, and H. Wang, “1024-Pixel CMOS Multi-Modality Joint Cellular Sensor/Stimulator Array for Real-Time Holistic Cellular Characterization and Cell-Based Drug Screening” *accepted and to appear in IEEE Trans. Biomed. Circuits Syst.(**T-BCAS**),* 2017.
[21] W. Franks, I. Schenker, P. Schmutz, and A. Hierlemann, “Impedance characterization and modeling of electrodes for biomedical applications,” IEEE Trans. Biomed. Eng., vol. 52, no. 7, pp. 1295–1302, July. 2005.
[22] D. Jaron, H. Schwan, and D. Geselowitz, “A mathematical model for the polarization impedance of cardiac pacemaker electrodes,” Med. & Biol. Engng., vol. 6, no. 6, pp. 579-594, Nov. 1968.
[23] S.E. Moulton, J.N. Barisci, A. Bath, R. Stella, and G.G. Wallace, “Studies of double layer capacitance and electron transfer at a gold electrode exposed to protein solutions,” Electrochimica Acta, vol. 49, no. 24, pp. 4223-4230, Sept. 2004.
[24] M. A. P. Pertijs, A. Niederkorn, X. Ma, B. McKillop, A. Bakker, and J. H. Huijsing, “A CMOS smart temperature sensor with a 3σ inaccuracy of ±0.5 ºC from -50 ºC to 120 ºC,” IEEE J. Solid-State Circuits, vol. 40, no. 2, pp. 454–461, Feb. 2005.
[25] H. Wichterle et al., “Directed differentiation of embryonic stem cells into motor neurons,” Cell, vol. 110, no. 3, pp. 385–397, Aug. 2002.
[26] X. Lian et al., “Directed cardiomyocyte differentiation from human pluripotent stem cells by modulating Wnt/ -catenin signaling under fully defined conditions,” Nature Protoc., vol. 8, no. 1, pp. 162–175, Jan. 2013.
[27] M. M. Hossain et al., “Non-invasive characterization of mouse embryonic stem cell derived cardiomyocytes based on the intensity variation in digital beating video,” Analyst, 135, pp. 1624-1630, Jun. 2010.
[28] B. Razavi, RF Microelectronics, 2012, Prentice-Hall.
[29] R. Muller, S. Gambini, and J. Rabaey, “A 0.013 mm2, 5µW, DC-coupled neural signal acquisition IC with 0.5V supply,” IEEE J. Solid-State Circuits, vol. 47, no. 1, pp. 232–243, Jan. 2012.

[30] C. Huang, Y. Huang et al., "A fully integrated hepatitis B virus DNA detection SoC based on monolithic polysilicon nanowire CMOS process," Proc. IEEE VLSI Tech. Cir. Symp., June 2012.
[31] Y. Feng, T. Mitchison, A. Bender, D. Young, and J. Tallarico, "Multi-parameter phenotypic profiling: using cellular effects to characterize small-molecule compounds," Nat. Rev. Drug Discov., vol. 8, pp. 567-578, July 2009.
[32] J. E. Ali, P. K. Sorger, and K. F. Jensen, "Cells on chips," Nature, 442, 27, pp. 403-411, Jul. 2006.
[33] T. Riss, "Selecting cell-based assays for drug discovery screening," Cell Notes, 13, 2005.
[34] H. Wang, A. Mohdavi, D. Tirrell, and A. Hajimiri, "A magnetic cell-based sensor," Lab Chip, vol. 12, pp. 4465-4471, 2012.
[35] J. Woodcock, "The prospects for 'personalized medicine' in drug development and drug therapy," Clinical Pharmacology & Therapeutics, vol. 81, no. 2, pp. 164-169, Feb. 2007.
[36] S. Liebeschuetz, S. Bamber, K. Ewer, J. Deeks, A. A. Pathan, and A. Lalvani, "Diagnosis of tuberculosis in South African children with a T cell-based assay: a prospective cohort study," The Lancet, vol. 364, no. 9452, pp. 2196-2203, Dec. 2004.
[37] P. Banerjee and A. K. Bhunia, "Mammalian cell-based biosensors for pathogens and toxins," Trends in Biotechnology, vol. 27, no. 3, pp. 179-188, Mar. 2009.
[38] D. A. Borkholder, B. D. DeBusschere, and G. T. A. Kovacs, "An approach to the classification of unknown biological agents with cell based sensors," Solid-State Sensor and Actuator Workshop, pp. 178-182, Jun. 1998.
[39] S. Girotti, E. N. Ferri, M. G. Fumo, and E. Maiolini, "Monitoring of environmental pollutants by bioluminescent bacteria," Analytica Chimica Acta, vol. 608, no. 1, pp. 2-29, Feb. 2008.
[40] M. Jenkner, M. Tartagni, A. Hierlemann, and R. Thewes, "Cell-based CMOS sensor and actuator arrays," IEEE J. Solid-State Circuits, vol. 39, no. 12, pp. 2431–2437, Dec. 2004.
[41] G. Medoro, N. Manaresi, A. Leonardi, L. Altomare, M. Tartagni, and R. Guerrieri, "A lab-on-a-chip for cell detection and manipulation," IEEE Sens. J., vol. 3, no. 3, pp. 317–325, 2003.
[42] E. Noorsal, et al., "A neural stimulator frontend with high-voltage compliance and programmable pulse shape for epiretinal implants," IEEE J. Solid-State Circuits, vol. 47, no. 1, pp. 244–256, Jan. 2012.
[43] C. Lopez, A. Andrei, S. Mitra, M. Welkenhuysen, W. Eberle, C. Bartic, R. Puers, R. Yazicioglu, and G. Gielen, "An implantable 455-activeelectrode 52-channel CMOS neural probe," IEEE J. Solid-State Circuits, vol. 49, no. 1, pp. 248–261, Jan 2014.
[44] E. R. Fossum, "CMOS image sensors: electronic camera-on-a-chip," lEEE Trans. Electron Devices, vol. 44, no. 10, pp. 1689-1698, Oct. 1997.
[45] T. Sun and H. Morgan, "Single-cell microfluidic impedance cytometry: a review", Microfluid. Nanofluid., vol. 8, no.4, pp. 423–443, Apr. 2010.
[46] R. Schaumann and M. V. Valkenburg, Design of Analog Filters, 2nd edition, Oxford University Press, 2009.
[47] [Online] Available: http://www.accutase.com/accutase.html

[48] U. Cavallaro and G. Christofori, "Cell adhesion and signalling by cadherins and Ig-CAMs in cancer", Nat. Rev. Cancer, vol. 4, pp. 118–132, Feb. 2004.
[49] H. Shen, Illustrated Pharmacology Memory Cards: PharMnemonics, 1st edition, Minireview, 2007.
[50] H. Nakazawaa, et al., "Multimodal bio-image sensor for real-time proton and fluorescence imaging," Sens. Actuators B: Chem., vol. 180, pp. 14–20, Nov. 2011.
[51] Y.-J. Huang, T.-H. Tzeng, T.-W. Lin, C.-W. Huang, P.-W. Yen, P.-H. Kuo, C.-T. Lin, and S.-S. Lu, "A self-powered CMOS reconfigurable multi-sensor SoC for biomedical applications," IEEE J. Solid-State Circuits, vol. 49, no. 4, pp. 851–866, Apr. 2014.
[52] W. P. Chan, et al., "A monolithically integrated pressure/oxygen/temperature sensing SoC for multimodality intracranial neuromonitoring," IEEE J. Solid-State Circuits, vol. 49, no. 11, pp. 2449–2461, Nov. 2014.
[53] H. Lee, Y. Liu, R. Westervelt, and D. Ham, "IC/Microfluidic hybrid system for magnetic manipulation of biological cells," IEEE J. Solid-State Circuits, vol. 41, no. 6, pp. 1471–1480, Jun. 2006.
[54] R. Tunuguntla, M. Bangar, K. Kim, P. Stroeve, C. Grigoropoulos, C. Ajo-Franklin, and A. Noy, "Bioelectronic light-gated transistors with biologically tunable performance," Advanced Materials, vol. 27, pp. 831-836, Nov. 2014.
[55] K. Iniewski, Integrated microsystems: electronics, photonics, and biotechnology, Boca Raton, FL, US: CRC Press, 2012.
[56] H. Wang, "Integrated biosensors in CMOS," IEEE International Midwest Symposium on Circuits and Systems (MWSCAS), Aug. 2011.
[57] S. Shamah, and B. Cunningham, "Label-free cell-based assays using photonic crystal optical biosensors," Analyst, vol. 136, pp. 1090-1102, Jan. 2011.
[58] H. Wang, "Magnetic Sensors for Diagnostic Medicine: CMOS-Based Magnetic Particle Detectors for Medical Diagnosis Applications," IEEE Microwave Magazine, vol. 14, no. 5, pp. 110-130, July-Aug. 2013.
[59] R. Wilke, D. Lin, D. Roden, P. Watkins, D. Flockhart, I. Zineh, K. Giacomini, and R. Krauss, "Identifying generic risk factors for serious adverse drug reactions: current progress and challenges," Nat. Rev. Drug Discov., vol. 6, no. 11, pp. 904-916, Nov. 2007.
[60] R. Shah, "Cardiac repolarization and drug regulation," Drug Safety, vol. 30, no. 12, pp. 1093-1110, Dec. 2007.
[61] E. Esch, A. Bahinski, and D. Huh, "Organs-on-chips at the frontiers of drug discovery," Nat. Rev. Drug Discov. 2015 April; 14(4): 248–260.
[62] G. Gil, R. Mitchell, S. Chang, and M. Gu, "A biosensor for the detection of gas toxicity using a recombinant bioluminescent bacterium," Biosensors and Bioelectronics, vol. 15, no. 1-2, pp.23-30, Mar. 2000.
[63] R. Kubisch, U. Bohrn, M. Fleischer, and E. Stutz, "Cell-based sensor system using L6 cells for broad band continuous pollutant monitoring in aquatic environments," Sensors, vol. 12, pp. 3370–3393, Mar. 2012.
[64] A. Yufera, A. Rueda, J. Munoz, R. Doldan, G. Leger, and E. Rodriguez-Villegas, "A tissue impedance measurement chip for myocardial ischemia detection", IEEE Trans. Circuits Syst. I, Reg. Papers, vol. 52, no. 12, pp. 2620–2628, Dec. 2005.

[65] B. Cheah, A. Macdonald, C. Martin, A. Streklas, G. Campbell, M. Al-Rawhani, B. Nemeth, J. Grant, M. Barrett, and D. Cumming, "An integrated circuit for chip-based analysis of enzyme kinetics and metabolite quantification", IEEE Trans. Biomed. Circuits Syst., vol. 10, no. 3, pp. 721–730, June 2016.
[66] X. Huang, H. Yu, X. Liu, Y. Jiang, M. Yan, and D. Wu, "A dual-mode large-array CMOS ISFET sensor for accurate and high-throughput pH sensing in biomedical diagnosis", IEEE Trans. Biomed. Eng., vol. 62, no. 9, pp. 2224–2233, Sept. 2015.
[67] I. Lee, S. Lee, K. Lee, C. Park, D. Kim, J. Lee, H. Yi, and B. Kim, "A reconfigurable and portable highly sensitive biosensor platform for ISFET and enzyme-based sensors," IEEE Sensors Journal, vol. 16, no. 11, June 2016.
[68] H. Wang, Y. Chen, A. Hassibi, A. Scherer, and A. Hajimiri, "A frequency-shift CMOS magnetic biosensor array with single-bead sensitivity and no external magnet," IEEE International Solid-State Circuits Conference (ISSCC), pp. 438-439, Feb. 2009.
[69] H. Wang, C. Sideris, and A. Hajimiri, "A Frequency-Shift based CMOS Magnetic Biosensor with Spatially Uniform Sensor Transducer Gain," IEEE Custom Integrated Circuits Conference (CICC) Dig. Tech. Papers, Sep. 2010.
[70] P. P. Liu, K. Skucha, Y. Duan, M. Megens, K. Jungkyu, I. I. Izyumin, S. Gambini, and B. Boser, "Magnetic relaxation detector for microbead labels," IEEE J. Solid-State Circuits, vol. 47, no. 4, pp. 1056–1064, Apr. 2012.
[71] H. Wang, C. Weng, and A. Hajimiri, "Phase noise and fundamental sensitivity of oscillator-based reactance sensors," IEEE Transaction on Microwave Theory and Techniques (T-MTT), vol. 61, no. 5, pp. 2215-2229, May 2013.
[72] A. Pai, A. Khachaturian, S. Chapman, A. Hu, H. Wang, and A. Hajimiri, "A handheld magnetic sensing platform for antigen and nucleic acid detection," Analyst 139 (6), pp. 1403-1411, Dec. 2013.
[73] N. Manaresi, A. Romani, G. Medoro, L. Altomare, A. Leonardi, M. Tartagni, and R. Guerrieri, "A CMOS chip for individual cell manipulation and detection," IEEE J. Solid-State Circuits, vol. 38, no. 12, pp. 2297–2305, Dec. 2003.
[74] H. Lee, K. Kwon, W. Li, and M. Ghovanloo, "A power-efficient switched-capacitor stimulating system for electrical/optical deep brain stimulation," IEEE J. Solid-State Circuits, vol. 50, no. 1, pp. 360–374, Jan. 2015.
[75] J. Christen, and A. Andreou, "Design, fabrication, and testing of a hybrid CMOS/PDMS microsystem for cell culture and incubation," IEEE Trans. Biomed. Circuits Syst., vol. 1, no. 1, pp. 3–18, Mar. 2007.
[76] P. Stefano et al., "Monophasic and Biphasic Electrical Stimulation Induces a Precardiac Differentiation in Progenitor Cells Isolated from Human Heart", Stem Cells and Development, vol. 23, no. 8, pp. 888-898, Dec. 2013.
[77] Y. Chan, S. Ting, Y. Lee, K. Ng, J. Zhang, Z. Chen, C. Siu, S. Oh, and H. Tse, "Electrical stimulation promotes maturation of cardiomyocytes derived from human embryonic stem cells", J. of Cardiovasc. Trans. Res., vol. 6, no. 6, pp. 989-999, Dec. 2013.
[78] N. Davidovics, G. Fridman, B. Chiang, and C. Santina, "Effects of biphasic current pulse frequency, amplitude, duration, and interphase gap on eye movement responses to prosthetic electrical stimulation of the vestibular nerve," IEEE Transaction on Neural Systems and Rehabilitation Engineering, vol. 19, no. 1, Feb. 2011.

[79] J. Wong, J. Olson, M. Morhart, and K. Chan, “Electrical stimulation enhances sensory recovery; a randomized controlled trial,” Annals of Neurology, vol. 77, no. 6, May 2015.
[80] C. N. Heck et al., “Two-year seizure reduction in adults with medically intractable partial onset epilepsy treated with responsive neurostimulation: Final results of the RNS system pivotal trial,” Epilepsia, vol. 55, no. 3, pp. 432–441, 2014.
[81] M. L. Kringelbach, N. Jenkinson, S. L. F. Owen, and T. Z. Aziz, “Translational principles of deep brain stimulation,” Nat. Rev. Neurosci., vol. 8, no. 8, pp. 623–635, 2007.
[82] A. Berényi, M. Belluscio, D. Mao, and G. Buzsáki, “Closed-loop control of epilepsy by transcranial electrical stimulation,” Science, vol. 337, no. 6095, pp. 735–737, Aug. 2012.
[83] J. Weiland, D. Anderson, and M. Humayun, “In vitro electrical properties for iridium oxide versus titanium nitride stimulating electrodes,” IEEE Transaction on Biomedical Engineering, vol. 49, no. 12, pp. 1574-1579, Dec. 2002.
[84] N. Aryan, H. Kaim, A. Rothermel, Stimulation and recording electrodes for neural prostheses, Springer, 2015.
[85] D. Merrill, M. Bikson, and J. Jefferys, “Electrical stimulation of excitable tissue: design of efficacious and safe protocols”, Journal of Neuroscience Methods, vol. 141, no. 2, pp. 171-198, Feb. 2005.
[86] M. Zia, T. Chi, C. Zhang, P. Thadesar, T. Hookway, J. Gonzalez, T. McDevitt, H. Wang, and M. Bakir, “A microfabricated electronic microplate platform for low-cost repeatable biosensing applications,” IEEE International Electron Devices Meeting (IEDM), Dec. 2015.
[87] M. Zia, T. Chi, J. Park, A. Su, J. Gonzalez, P. Jo, M. Styczynski, H. Wang, and M. Bakir, “3-D integrated electronic microplate platform for low-cost repeatable biosensing applications,” IEEE Transaction on Components, Packaging and Manufacturing Technology, vol. 6, no. 12, pp. 1827-1833, Dec. 2016.
[88] H. Wang, S. Kosai, C. Sideris, and A. Hajimiri, “An ultrasensitive CMOS magnetic biosensor array with correlated double counting noise suppression,” IEEE International Microwave Symposium (IMS), pp. 616-619, May 2010.
[89] B. Thurgood, D. Warren, N. Ledbetter, G. Clark, and R. Harrison, “A wireless integrated circuit for 100-channel charge-balanced neural stimulation,” IEEE Trans. Biomed. Circuits Syst., vol. 3, no. 6, pp. 405-414, Dec. 2009.
[90] N. Kapoor, W. Liang, E. Marbán, and H. Cho, “Direct conversion of quiescent cardiomyocytes to pacemaker cells by expression of Tbx18”, Nat. Biotechnol. vol. 31, pp. 54–62, Jan. 2013.
[91] N. Kapoor, G. Galang, E. Marbin, and H. Cho, “Transcriptional suppression of connexin43 by TBX18 undermines cell-cell electrical coupling in postnatal cardiomyocytes”, Journal of Biological Chemistry, vol. 286, no. 16, pp. 14073-14079, April 2011.
[92] H. Wang, A. Mahdavi, J. Park, T. Chi, J. Butts, T. Hookway, T. McDevitt, D. Tirrell, and A. Hajimiri, “Cell culture and cell based sensor on CMOS,” IEEE Biomedical Circuits and Systems Conference (BioCAS), pp. 1-4, Oct. 2014.

[93] B. Dura, M. Chen, O. Inan, G. Kovacs, and L. Giovangrandi, "High-frequency electrical stimulation of cardiac cells and application to artifact reduction," IEEE Trans. Biomed. Circuits Syst., vol. 59, no. 5, pp. 1381-1390, May 2012.
[94] A. Mendrela, J. Cho, J. Fredenburg, V. Nagaraj, T. Netoff, M. Flynn, and E. Yoon, "A bidirectional neural interface circuit with active stimulation artifact cancellation and cross-channel common-mode noise suppression," IEEE J. Solid-State Circuits, vol. 51, no. 4, pp. 955–965, April 2016.
[95] J. Dragas, V. Viswam, A. Shadmani, Y. Chen, R. Bounik, A. Stettler, M. Radivojevic, S. Geissler, M. Obien, J. Muller, and A. Hierlemann, "In vitro multi-functional microelectrode array featuring 59 760 electrodes, 2048 electrophysiology channels, stimulation, impedance measurement, and neurotransmitter detection channels," IEEE J. Solid-State Circuits, vol. 52, no. 6, pp. 1576–1590, June 2017.
[96] Q. Fan, et al., "A 1.8 μW 60 nV/√Hz Capacitively-Coupled Chopper Instrumentation Amplifier in 65 nm CMOS for Wireless Sensor Nodes," IEEE J. Solid-State Circuits, vol. 46, no. 7, pp. 1534−1543, Jul. 2011.
[97] C. Liu, S. Chang, G. Huang, and Y. Lin, "A 10-bit 50-MS/s SAR ADC with monolithic capacitor switching procedure," IEEE J. Solid-State Circuits, vol. 45, no. 4, pp. 731–740, Apr. 2010.
[98] J. Weiland, and D. Anderson, "In Vitro electrical properties for iridium oxide versus titanium nitride stimulating electrodes," IEEE Transaction on Biomedical Engineering, vol. 49, no. 12, Dec. 2002.
[99] H. Chandrakumar, and D. Markovic, "A 2μW 40mVpp linear-input-range chopper stabilized bio-signal amplifier with boosted input impedance of 300MΩ and electrode-offset filtering," IEEE International Solid-State Circuits Conference (ISSCC), pp. 96-97, Feb. 2016.